

**NASA TECHNICAL  
REPORT**

NASA TR R-429



NASA TR R-429

**CASE FILE  
COPY**

**DRAG AND STABILITY CHARACTERISTICS  
OF A VARIETY OF REEFED AND UNREEFED  
PARACHUTE CONFIGURATIONS AT MACH 1.80  
WITH AN EMPIRICAL CORRELATION  
FOR SUPERSONIC MACH NUMBERS**

*Lana M. Couch*

*Langley Research Center  
Hampton, Va. 23665*



NATIONAL AERONAUTICS AND SPACE ADMINISTRATION • WASHINGTON, D. C. • FEBRUARY 1975

1. Report No. NASA TR R-429	2. Government Accession No.	3. Recipient's Catalog No.	
4. Title and Subtitle DRAG AND STABILITY CHARACTERISTICS OF A VARIETY OF REEFED AND UNREEFED PARACHUTE CONFIGURATIONS AT MACH 1.80 WITH AN EMPIRICAL CORRELATION FOR SUPER-SONIC MACH NUMBERS		5. Report Date February 1975	
		6. Performing Organization Code	
7. Author(s) Lana M. Couch		8. Performing Organization Report No. L-9265	
9. Performing Organization Name and Address  NASA Langley Research Center Hampton, Va. 23665		10. Work Unit No. 760-17-01-11	
		11. Contract or Grant No.	
12. Sponsoring Agency Name and Address National Aeronautics and Space Administration Washington, D.C. 20546		13. Type of Report and Period Covered Technical Report	
		14. Sponsoring Agency Code	
15. Supplementary Notes			
16. Abstract  <p>An investigation was conducted at Mach 1.80 in the Langley 4-foot supersonic pressure tunnel to determine the effects of variation in reefing ratio and geometric porosity on the drag and stability characteristics of four basic canopy types deployed in the wake of a cone-cylinder forebody. The basic designs included cross, hemisflo, disk-gap-band, and extended-skirt canopies; however, modular cross and standard flat canopies and a ballute were also investigated. An empirical correlation was determined which provides a fair estimation of the drag coefficients in transonic and supersonic flow for parachutes of specified geometric porosity and reefing ratio.</p>			
17. Key Words (Suggested by Author(s))  Parachutes Drag Stability		18. Distribution Statement  Unclassified - Unlimited   STAR Category 01	
19. Security Classif. (of this report) Unclassified	20. Security Classif. (of this page) Unclassified	21. No. of Pages 109	22. Price* \$ 5.25



DRAG AND STABILITY CHARACTERISTICS OF A VARIETY OF REEFED AND  
UNREEFED PARACHUTE CONFIGURATIONS AT MACH 1.80 WITH AN  
EMPIRICAL CORRELATION FOR SUPERSONIC MACH NUMBERS

By Lana M. Couch  
Langley Research Center

SUMMARY

An investigation was conducted at Mach 1.80 in the Langley 4-foot supersonic pressure tunnel to determine the effects of variation in reefing ratio and geometric porosity on the drag and stability characteristics of four basic canopy types deployed in the wake of a cone-cylinder forebody. The canopy designs included cross, hemisflo, disk-gap-band, and extended-skirt canopies; in addition, modular cross and standard flat canopies and a ballute were investigated.

In general, the drag coefficients increased with increasing constructed reefing ratio and with increasing geometric porosity for the test range of porosities regardless of canopy design. Photographic data showed that, for all the canopies, the inflated reefing ratio attained during the test increased with increasing constructed reefing ratio. However, for the cross and hemisflo canopies, plateaus were reached such that further increases in constructed reefing ratio resulted in no substantial increases in inflated reefing ratio or drag coefficient.

In general, the canopies were fairly stable, with the exception of the cross canopies which experienced large drag variations due to both breathing and squidding of the canopy and coning motions of the parachute. Almost all the canopies exhibited some breathing and coning motions, but their amplitudes were less than those of the cross canopies.

An empirical correlation which provides a fair estimation of the drag coefficients in transonic and supersonic flow for parachutes of specified geometric porosity and reefing ratio was determined from the wind-tunnel data. Examination of the experimental measurements indicated that the parameters having the dominant effects on drag coefficient are reefing ratio, geometric porosity, and Mach number. Other variables, such as canopy type, dynamic pressure, and stiffness, apparently had only a minor influence on the drag coefficient.

## INTRODUCTION

The supersonic aerodynamic characteristics of flat plates normal to the flow, convex and concave hemispherical models, and blunt-nose rigid models have been documented from wind-tunnel data (refs. 1 to 4) and can, in many cases, be theoretically predicted. Decelerators often have configurations which are similar in shape to the models previously mentioned, but are flexible and rarely have a steady-state or fixed geometry. Consequently, investigations of decelerators are generally conducted on flexible models in wind tunnels or free flight to determine their aerodynamic characteristics. Unfortunately, these investigations are usually limited to a small number of configurations and, therefore, do not provide sufficient data for a parametric analysis.

The present investigation was conducted to provide systematic parachute design information on the effects of variation of reefing ratio and geometric porosity on the drag and stability characteristics of four basic canopy designs deployed from a cone-cylinder forebody into supersonic flow. The four types of canopies were cross, hemisflo, disk-gap-band, and extended skirt. In addition, a larger diameter hemisflo, modular cross and standard flat parachutes and a ballute were investigated. The experimental data, obtained at a Mach number of 1.80, were empirically correlated and a Mach-number variation was superimposed which resulted in an equation for predicting drag coefficient based on reefing ratio, geometric porosity, and Mach number.

The configurations were tested in the Langley 4-foot supersonic pressure tunnel at a free-stream Mach number of 1.80 and a dynamic pressure of 12.1 kN/m<sup>2</sup>. The performance characteristics obtained included quantitative drag and stability data and qualitative flow field and stability characteristics.

## SYMBOLS

$A_e$	exit area of canopy, $\eta \frac{\pi D_o^2}{4}$
$A_i$	inflated minimum-inlet area of canopy, $\frac{\pi D_i^2}{4}$
$A_o$	nominal area of canopy
$C_{D_i}$	drag coefficient based on inflated minimum-inlet area of canopy, $\frac{\text{Time-averaged drag force}}{qA_i}$

$C_{D_0}$	drag coefficient based on nominal area of canopy, $\frac{\text{Time-averaged drag force}}{qA_0}$
$d$	maximum forebody diameter
$D_i$	time-averaged, inflated, minimum-inlet diameter, measured from lateral view of canopy
$D_{\max}$	time-averaged, inflated, maximum canopy diameter, measured from lateral view of canopy
$D_0$	nominal constructed diameter of canopy, $\sqrt{\frac{4A_0}{\pi}}$
$F_D$	drag force
$M$	free-stream Mach number
$p_t$	free-stream stagnation pressure
$q$	free-stream dynamic pressure
$R$	Reynolds number
$t$	time
$x$	longitudinal distance from forebody base to plane of canopy inlet
$\eta$	geometric porosity of canopy
$\xi$	reefing ratio, $\frac{D_i}{D_0}$
$\xi_{\text{const}}$	constructed reefing ratio, $\frac{\text{Constructed inlet diameter}}{D_0}$
$\xi_{\text{inf}}$	inflated reefing ratio, $\frac{D_i}{D_{\max}}$

## WIND TUNNEL AND INSTRUMENTATION

The investigation was conducted in the Langley 4-foot supersonic pressure tunnel at a free-stream Mach number of 1.80 and a stagnation pressure of  $31.0 \text{ kN/m}^2$ . This continuous flow wind tunnel has a stagnation pressure range from approximately 21 to  $207 \text{ kN/m}^2$  at a stagnation temperature of 316.7 K. Discrete Mach numbers can be obtained from 1.41 to 2.20 by using interchangeable nozzle templates.

The data acquisition system consisted of a six-component strain-gage balance and transducers which transmitted electrical outputs to self-balancing potentiometers. The outputs were then digitized and punched into cards. Reference pressures were measured on precision mercury manometers. Output from all six components of the balance was recorded; however, only the axial-force data are presented. The maximum rated loading capacity of the axial beam of the balance was 889.6 N. This maximum capacity was considerably higher than the average load obtained, but was needed to accommodate the excursions which resulted from parachute dynamics.

An oscillograph, which recorded the time history of the dynamic response of the balance axial beam, was started immediately before deployment and recorded for about 60 sec. High-speed, black and white schlieren movies, which recorded for 16 sec at 1000 frames per second, and 16 mm color movies, which recorded for 40 sec at 400 frames per second, were obtained simultaneously with the force data.

## APPARATUS

The parachutes and ballute were tested downstream of a cone-cylinder forebody, which was supported in the center of the test section by two tapered struts. The struts were mounted to the tunnel sidewalls in the upstream region of the test section. Photographs of the installation and sketches of the forebody and strut geometry are presented in figures 1 and 2, respectively. The stainless steel forebody had a fineness ratio of 9.6: a maximum diameter of 6.1 cm and 57.8 cm in length. A band of 0.03-cm-particle-size grit was placed 2.54 cm downstream of the forebody conical apex in order to insure early boundary-layer transition to turbulent flow. The boundary-layer transition and the grit size were determined according to the criteria of references 5 and 6, respectively.

Each steel supporting strut was welded to a plate which was bolted to the tunnel sidewall. The plate was 56.4 cm in length and had a maximum width of 15.2 cm. The apex angle of the conical-wedge section of the plate ( $2.4^\circ$ ) and the thickness of the plate (1.3 cm) were held as small as possible to minimize the effect of supporting structure on the flow field of the decelerators. The boundary-layer thickness on the test-section wall in the region of the supporting structure was approximately 7.62 cm; therefore, the plate

thickness was approximately 17 percent of the total boundary-layer thickness. Each tapered strut, a wedge—flat-plate—wedge cross-sectional design, had 64.5 cm semispan, 20.3 cm chord at the test-section wall, and 10.2 cm chord at the intersection with the forebody. The struts varied in thickness from 1.3 cm at the test-section wall to 0.6 cm at the forebody. The total wedge angle at the leading and trailing edges was approximately  $14.3^\circ$ . A groove in the strut surface was provided for pressure tubes and electrical leads to be brought to an external access point in the test-section sidewall.

The decelerators were attached to a balance adapter (fig. 1) with a swivel between the adapter attachment point and the confluence point of the suspension lines to prevent wrapping of the lines due to canopy spinning. Swivel failure did occur and the suspension lines wrapped as shown in figure 3, but those data were not used. Each canopy and its suspension lines were packed in a cylindrical cloth bag and the opening of the bag was drawn closed with a 16.0-N line. A 2.5-kN deployment line was attached to the rear of the bag and routed through the permanent strut assembly and the tunnel wall to the outside. Therefore, when the desired test conditions were established and all recording instrumentation had been prepared, the decelerator was deployed manually by steadily pulling the deployment line. Photographs of the deployment sequence of a 0.33-m-diameter hemisflo parachute are presented in figure 4. The sequence of photographs shows the bag deployment at  $t = 0$  sec, line snatch or full extension of the suspension lines at  $t = 0.023$  sec, and the period of canopy inflation between  $t = 0.028$  and  $0.043$  sec. In the lower right photograph, the canopy is at a steady condition.

## TEST MODELS

The seven decelerator configurations investigated included parachutes with cross, hemisflo, disk-gap-band, extended-skirt, modular cross, and standard flat canopies and a ballute. The modular cross parachute was a direct combination of two cross parachutes, and the standard flat parachute was a disk-gap-band parachute with the band removed. The dimensions and design specifications for each type of decelerator are presented in figure 5 and tables I and II, respectively.

## TEST CONDITIONS AND TEST VARIABLES

The configurations were tested at a selected free-stream Mach number of 1.80 and a free-stream dynamic pressure of  $12.1 \text{ kN/m}^2$ . The extended-skirt canopies were tested at a reduced dynamic pressure of approximately  $6.8 \text{ kN/m}^2$  to prevent damage to the force-balance axial beam due to overloading. The parachutes tested had geometric porosities which ranged from 0.06 to 0.413 and constructed reefing ratios which ranged

from 0.16 to 0.57. A tabulation of the configurations and parametric variables is presented in table II.

## ACCURACY AND CORRECTIONS

Data obtained with the force balance and recording system used in this investigation are normally determined to be accurate to 0.5 percent of the maximum capacity of the beam. Therefore, since the maximum loading capacity of the axial beam was 889.6 N, the accuracy of the drag measurements in this investigation would be 4.45 N. It should be noted that this accuracy specification is intended for a steadily applied load – not for the extensive dynamic loading applied to the beam by a parachute. However, it is the opinion of the instrumentation specialists that the lag time is negligible for the frequencies experienced. The uncorrected measurements were recorded at intervals of approximately 10 sec over a period of approximately 1 min. These measurements were then averaged and compared with the average uncorrected drag value determined from the continuous oscillograph trace, which provided an immediate check on the method of random acquisition of the uncorrected drag data. The values of drag coefficient were corrected for the drag force acting over the balance base area. Measurements taken from the film are accurate to 0.03 cm. The accuracies of other parameters are:

M . . . . .  $\pm 0.005$

$p_t$ , kN/m<sup>2</sup> . . . . .  $\pm 0.14$

$q$ , kN/m<sup>2</sup> . . . . .  $\pm 0.14$

## RESULTS AND DISCUSSION

### Force-Balance Drag Data of the Various Parachutes

The variation of drag coefficient with constructed reefing ratio is presented in figures 6(a) to 6(d) for each of the various canopy types with a summary plot of all configurations in figure 6(e). The drag coefficients for the cross and modular cross canopies were computed using the fabric surface area; whereas, for all other canopies the nominal area was used. The unreefed configurations are plotted at  $\xi_{const} = 1.0$ . In general, the drag coefficient increases with both increasing constructed reefing ratio and geometric porosity for the test range of parameters, but at different rates of increase for the various canopy types, as indicated by the faired data. It should be noted in figure 6(d) for the disk-gap-band canopies that the drag coefficient obtained for the unreefed 0.125-geometric-porosity parachute is substantially lower than the drag coefficients obtained for the 0.06- and 0.20-geometric-porosity parachutes.

Several parachutes were modified during the investigation to determine the effects of the various structural alterations. Decreasing the suspension line length from  $1.4D_0$  to  $1.0D_0$  ( $x/d$  from 8.40 to 6.38) for the cross parachute (configuration 23) resulted in a slight increase in the drag coefficient. However, a modular cross parachute constructed from two cross parachutes and having twice as many suspension lines as a cross parachute produced a drag coefficient that was approximately 50 percent lower than the value obtained for the cross parachute of the same reefing ratio.

The 0.33-m-diameter hemisflo parachute (configuration 42 in fig. 6(b)) was unreefed and trailed the forebody at a value of  $x/d$  of 10.42 in contrast to 7.65 for the other hemisflo canopies. The drag coefficient was about 30 percent higher for the large unreefed hemisflo parachute than for the smaller parachutes. Removing the meridional tapes from the vent of configuration 29 resulted only in a very slight increase in drag coefficient.

In figure 6(d), configurations 32 and 34, which were reefed on the leading edge of the disk, showed only very slight increases in drag coefficient over the comparable configurations which were reefed on the leading edge of the band.

Variations of the parachute steady-state drag coefficients with Mach number, obtained both from the present investigation and from other sources, including unpublished data obtained in 1969 at the Arnold Engineering Development Center (AEDC) for the U.S. Air Force, are presented in figure 7. Cross parachute configurations (fig. 7(a)) having reefing ratios greater than 0.40 were compared with unreefed configurations of other investigations, since no unreefed cross parachutes were tested in this investigation. This comparison was reasonable since photographic data showed that these configurations had reefing line lengths that would allow an inlet diameter greater than the maximum inlet diameter assumed by the canopy in the wind tunnel. All the reefed configurations presented had constructed reefing ratios of 0.273, and the parachutes ranged in constructed diameter from 0.305 to 3.05 m. All the cross parachute data are in good agreement with the data of reference 7 and from AEDC, with the exception of configuration 2 which had a drag coefficient about 20 percent higher than the unreefed parachute data.

The drag coefficients obtained for the unreefed hemisflo parachutes (fig. 7(b)) also are in agreement with the trend established by the data of references 8 to 10. The geometric porosities of the parachutes represented in this figure range from 0.085 to 0.197 with variations in canopy diameter from 0.305 to 1.83 m.

The variation of drag coefficient with Mach number for the unreefed disk-gap-band parachutes is presented in figure 7(c). The data obtained for the 0.125-geometric-porosity parachute of the present investigation are in agreement with the trend established by the data of references 11 and 12. However, the data of reference 13, which were obtained for a 0.125-geometric-porosity parachute, and the 0.06- and 0.20-geometric

porosity data of the present investigation have a somewhat higher level. The basic problem in the comparison of drag coefficients obtained for different size models of a given type of parachute is the difficulty in thorough geometric scaling of the models. This problem may account for the difference in levels of drag coefficients obtained for the 0.125-geometric-porosity, unreefed disk-gap-band parachutes in figure 7(c).

#### Dynamic Behavior of Parachutes Determined From Photographic Data

General comments on the dynamic behavior of the different types of parachutes are presented in this section; detailed descriptions of the dynamic behavior of the various configurations are included in appendix A. All comments made about the dynamic behavior of the various types of parachutes are based mainly on the photographic data; however, visual observations made during the investigation are also included (tables III, IV, and V). Effects included in the discussion of the dynamic behavior are breathing, coning, spinning motions, and the overall stability of the parachute. As was discussed in reference 13, the frequencies of the angular motions of parachutes incurred in the wind tunnel are generally much higher than those incurred in free-flight testing and may be inversely proportional to the canopy diameter. However, the amplitudes of the angular motions of the model parachutes (table IV) are similar in magnitude to the free-flight results on the large parachutes.

Continuous oscillograph traces of the direct output from the force-balance axial beam are presented for each configuration in figure 8. In general, these traces include the deployment sequence – consisting of bag deployment, line snatch, inflation period, and "steady-state," uncorrected drag data. A typical annotation of one trace (configuration 8) is shown in figure 8(a). This output obtained at  $q = 12.1 \text{ kN/m}^2$  indicated that, dynamically, the maximum loading capacity of the axial beam had been exceeded for this parachute which had the lowest reefing ratio of all the extended-skirt canopies. Therefore, in order to reduce the balance loading, all the extended-skirt canopies, including configuration 8, were tested at  $q = 6.8 \text{ kN/m}^2$  (fig. 6(e)). The spurious markings on these oscillograph traces result from the light sensitivity of the recording paper on which any wrinkle or fold in the paper results in a mark.

The oscillograph traces are included for the purpose of comparison of the dynamic behavior during steady-state testing of the various configurations. Although the results of the deployment method used in the wind tunnel are shown in these traces, no attempt to analyze deployment loads or times is included, since parachute deployment of a small model in a wind tunnel is not comparable with the deployment of large parachutes in free flight.

Cross canopies. - All the cross canopies were reefed even though the reefing line was sometimes too long and, therefore, ineffective. The cross canopies were consistent



in their behavior in that all but one configuration tended to be somewhat unstable due to breathing, coning, and spinning motions. The breathing frequency was sporadic, varying from approximately 70 to 125 Hz; the coning frequency was fairly constant at approximately 20 Hz; and the spinning frequency was approximately 20 Hz.

Modular cross canopy.- There was very little coning and no apparent breathing for the modular cross canopy. The canopy and suspension lines were stable and there was no determinable variation in the canopy diameter.

Hemisflo canopies.- The hemisflo canopies, which had geometric porosities of 0.085 and 0.147, were stable with little or no coning or spinning. Although the breathing frequencies of the hemisflo canopies were large (varying from approximately 100 to 200 Hz), the amplitude of the motion was quite small.

Extended-skirt canopies.- The extended-skirt canopies were fairly stable, had only small amplitudes due to the motions of breathing and coning, and did not spin. The breathing frequency varied from approximately 125 to 200 Hz, and the coning frequency varied from approximately 56 to 83 Hz.

Disk-gap-band canopies.- The disk-gap-band canopies, which had geometric porosities of 0.06, 0.125, and 0.20, were generally quite stable, had only small amplitudes due to breathing and coning motions, and did not spin. The breathing frequencies varied from approximately 100 to 200 Hz, and the coning frequency was approximately 56 Hz. Several canopies did oscillate slightly about the spin axis.

Standard flat canopy.- The standard flat canopy, consisting only of the disk from a disk-gap-band canopy, was investigated to determine the effect of the band on stability. The parachute was extremely unstable, and the erratic behavior precluded the determination of specific frequencies.

Ballute.- The ballute (configuration 35) was quite stable with no spinning or oscillation about the spin axis and very little breathing or coning. The breathing and coning frequencies were approximately 20 and 45 Hz, respectively. Unlike the majority of the parachutes, the ballute and meridional tape extensions generally remained aligned with the direction of the free-stream flow when coning and the coning angle was formed only by the riser line. Shortly after deployment of the ballute, the structure around the apex fatigued somewhat and the 90°-design apex angle changed to approximately 80°, but there was no apparent effect on the stability. Before and after the change in the apex angle, the ballute was quite well inflated both ahead of and behind the inlet band. The retention cord which secured the leading edge of the inlet band was either defective or of insufficient strength, since it failed a few seconds after deployment. The vent holes, which had been under the inlet band and subjected to stagnation pressure, were then subjected to a much lower pressure. Nevertheless, the ballute remained well inflated and was still quite stable.

## Description of Shock-Wave Patterns of Parachutes

General comments on the shock-wave patterns, which were observed in the high-speed schlieren movies of the different types of parachutes, are included in this section. The detailed descriptions of the shock-wave patterns of the various configurations are included in appendix B. Schlieren photographs which show the typical shock-wave pattern of each parachute are presented in figure 9.

Although the shock-wave patterns were dominated by changes both in canopy diameter due to breathing and in canopy asymmetry due to coning, the shock-wave pattern for most of the parachutes generally consisted of two main shock waves, as shown in figure 9(a) at four different times during the test of configuration 3. The upstream shock wave had a conical shape with changing virtual apex angle that increased with increasing suspension-line included angle (i.e., increasing canopy diameter) and decreased with decreasing suspension-line included angle (i.e., decreasing canopy diameter). The downstream shock wave consisted of either a conical shock wave attached to the canopy inlet lip or a bow shock wave standing at the canopy inlet curving to a conical shock wave downstream of the canopy.

Cross canopies.- The general instability of the cross canopies resulted in considerable asymmetry in the shock-wave patterns. However, during their short periods of stability, the cross canopies had the double shock-wave pattern described above. In addition, during canopy breathing, for canopies with reefing ratios greater than about 0.40, the downstream shock wave sometimes moved inside the canopy (i.e., was swallowed) when the inlet approached its maximum opening and then popped out as the inlet opening decreased in size, as shown for configuration 3 in figure 9(a).

Modular cross canopy.- The modular cross canopy had the same double shock-wave pattern described previously. The downstream shock wave was a bow shock just ahead of the canopy inlet.

Hemisflo canopies.- The hemisflo canopies had the same double shock-wave pattern which has been described previously and is shown in figure 9(b) at four different times during the testing of configuration 18. For canopies reefed at the lower reefing ratios (e.g., below about 0.30) the downstream shock wave generally had been swallowed by the canopy.

Extended-skirt canopies.- The extended-skirt canopies (fig. 9(d)) had the double shock-wave pattern with an additional shock wave which occasionally appeared on the canopy due to some asymmetry in the canopy contour. Also, the longitudinal movement of the upstream shock wave was more extensive for the extended-skirt canopies than for the cross or hemisflo canopies.

Disk-gap-band canopies. - The shock-wave pattern for the disk-gap-band canopies (fig. 9(c)) generally consisted of three shock waves: a conical shock wave from the suspension lines, a conical or bow-conical shock-wave combination from the band inlet, and a conical or bow-conical shock-wave combination from the disk inlet. Occasionally, a fourth shock wave formed due to canopy asymmetry or band-disk misalignment.

Standard flat canopy. - The standard flat canopy shown in figure 9(c) at four different times during the test, had the basic double shock-wave pattern. However, because of the instability of this parachute, many variations occurred in the shock-wave pattern.

Ballute. - Configuration 35, shown in figure 9(e) at four different times during the test, had a triple shock-wave pattern: a conical shock wave from the riser line between the swivel and confluence point, a bow-conical combination shock wave from near the inlet, and a bow-conical shock wave from the band region. Shortly after deployment, the angle of the shock wave from the inlet decreased slightly due to the change in the ballute apex angle, which was discussed previously.

The retention cord failure, also discussed previously, which forced the inlet band back against the surface of the ballute exposing the inlet holes, resulted only in a weakening of the shock wave emanating from the band. There was no significant change in the degree of inflation or shape of the ballute due to the decreased pressure at the inlet holes and, therefore, very little change in the shock-wave pattern.

#### Discussion of Empirical Correlation of Measured Force Data

The drag-coefficient data obtained in this investigation were examined for relationships with constructed canopy parameters. Although systematic variations of the experimental data with construction changes were observed in the data, these variations could not be directly defined by use of constructed canopy parameters. Therefore, the approach to analyzing the data was to determine empirically at  $M = 1.80$  the relationships between inflated and constructed canopy parameters, the relationship of the drag-coefficient data to the inflated canopy parameters, and consequently the relationship between the drag-coefficient data and the constructed canopy parameters. Finally, the empirical prediction was extended to include Mach number effects. This approach to the data analysis was possible since an extensive photographic record - including both high-speed color and schlieren movies - had been obtained throughout the investigation. Tabulations of parachute geometric characteristics and all quantities which were measured from the film are presented in tables II to V.

The standard flat canopy (configuration 40) is not included in the quantitative discussion because the dynamic motion of the canopy was so violent that a representative set of measurements could not be obtained from the film. The extended-skirt canopies

are included when the appropriate parameters are determinable. The data obtained for the standard flat and extended-skirt canopies are included in the tables.

All the decelerators tested in this investigation had geometrically porous canopies with the exceptions of the extended-skirt canopies, the standard flat canopy, and the ballute. A porous canopy is merely a flow-through model made of flexible material and, as such, in supersonic flow would be expected to exhibit consistent variations between certain aerodynamic characteristics and its inlet-to-exit area ratio. Since the mass flow through the canopy is related to the area ratio and would be expected to affect the canopy shape, the area ratio should therefore be related to canopy shape. Since the actual exit area of the canopy under flow conditions could not be determined, the parameter  $A_e$  was used which is defined as the product of the geometric porosity and the canopy nominal area for the hemispherical and disk-gap-band canopies. For the cross and modular cross canopies,  $A_e$  is the product of the geometric porosity and the area of the circle having a diameter equal to the panel length. It should be noted that the geometric porosity does not account for any contribution to mass flow due to flow through the fabric.

The variation of  $A_i/A_e$  with  $\xi_{inf}$  is presented in figure 10. The inlet area  $A_i$  is the inflated minimum-inlet area of the canopy. A parametric variation of  $A_i/A_e$  with  $\xi_{inf}$  is apparent with geometric porosity as the ordering parameter regardless of canopy design. It can be seen in figure 10 that at a constant  $\xi_{inf}$ , an increase in porosity results in a decrease in this area ratio, as would be expected.

Since in figure 10 the data were parametrically ordered by porosity, they can be correlated by appropriately including the effect of porosity as shown in figure 11. The equation

$$\frac{A_i}{A_e} = \frac{0.324}{\eta} (\xi_{inf})^{3.424} \quad (1)$$

describes the line which was faired through the correlated data. This equation is, in its simplest terms, a correlation between the canopy surface area and the maximum inflated diameter of the canopy. Therefore, the dependence of  $D_i/D_o$  (the ratio of inflated minimum-inlet diameter to constructed canopy diameter) on  $\xi_{inf}$  can be determined by substituting the definitions of  $A_i$  and  $A_e$  into equation (1) and solving for  $D_i/D_o$ . The equation then is

$$\frac{D_i}{D_o} = 0.569 (\xi_{inf})^{1.712} \quad (2)$$

which represents the bulk of the data quite well as can be seen in figure 12. Since the relationship between these two diameter ratios ( $D_i/D_o$  and  $\xi_{inf}$ ) is not affected by porosity, the data for the extended-skirt canopies are included in this figure.

In order to proceed toward determining the relationship between the constructed canopy parameters and the drag coefficients, a direct correspondence between measured and constructed quantities must be determined. The relationship between  $\xi_{\text{inf}}$  and  $\xi_{\text{const}}$  is presented in figure 13. An approximate relationship was derived by providing the best straight-line fit to the data of figure 13. The relationship between the two reefing ratios is then defined as the logarithmic expression described by the equation

$$\xi_{\text{inf}} = 0.305 \ln \xi_{\text{const}} + 1.106 \quad (3)$$

The effectiveness of increasing the constructed reefing ratio (i.e., constructed inlet diameter divided by  $D_0$ ) can be assessed directly by comparing it with the ratio  $D_i/D_0$ , as shown in figure 14 for the cross, hemisflo, disk-gap-band, and extended-skirt canopies. By substituting equation (3) for  $\xi_{\text{inf}}$  into equation (2), the empirically determined relation between  $D_i/D_0$  and  $\xi_{\text{const}}$  is found to be

$$\frac{D_i}{D_0} = 0.569(0.305 \ln \xi_{\text{const}} + 1.106)^{1.712} \quad (4)$$

With the exception of the two sets of hemisflo canopies and the cross canopies for values of  $\xi_{\text{const}}$  greater than approximately 0.45 and 0.33, respectively, the experimental data are well represented by the empirical curve of equation (4). For values of  $\xi_{\text{const}}$  greater than those indicated for the cross and hemisflo canopies,  $D_i/D_0$  reaches a plateau above which increasing the constructed inlet diameter becomes ineffective – producing no increase in the inflated minimum-inlet diameter. No plateaus were evident in the data obtained for either the disk-gap-band or the extended-skirt canopies.

Two of the disk-gap-band configurations (32 and 34) have not been included in these figures; since they were reefed on the disk rather than on the band, the inlet diameter measurements would not be comparable. The data for these two configurations are included in the tables.

The variation of the ratio of inflated maximum canopy depth to inflated maximum canopy diameter with the constructed reefing ratio is presented in figure 15. All the canopy types show a power-law variation between the two parameters, with the ratio of inflated maximum canopy depth to inflated maximum canopy diameter decreasing with increasing  $\xi_{\text{const}}$ , as would be expected. However, the magnitude of the ratio of the inflated parameters is slightly lower for the disk-gap-band canopies than for cross and hemisflo canopies at the same reefing ratios.

In an attempt to determine the relationship of the drag coefficient to inflated canopy parameters, the variation of  $C_{D_i}$  (the drag coefficient based on inflated minimum-inlet area) with the inlet-to-exit area ratio is presented in figure 16. Although the magnitudes are poorly represented, the general trend of the data are represented by the equation

$$C_{D_i} = 1.69 \left( \frac{A_i}{A_e} \right)^{-0.3} \quad (5)$$

By examining the definitions of the drag coefficients, the drag coefficient based on constructed canopy area can be written

$$C_{D_o} = C_{D_i} \left( \frac{D_i}{D_o} \right)^2$$

and since

$$\left( \frac{D_i}{D_o} \right)^2 = \eta \left( \frac{A_i}{A_e} \right)$$

then

$$C_{D_o} = C_{D_i} \left[ \eta \left( \frac{A_i}{A_e} \right) \right] \quad (6)$$

By substituting the empirically derived value for  $C_{D_i}$  from equation (5) into equation (6), the drag coefficient can be written

$$C_{D_o} = 1.69 \eta \left( \frac{A_i}{A_e} \right)^{0.7} \quad (7)$$

This equation is represented by the family of curves which are ordered by porosity and are in general agreement with the experimental data of figure 17. This figure shows that the drag coefficient increases both with increasing area ratio at constant porosity and with increasing porosity for constant area ratio. In figure 18, the constructed exit area is plotted against the measured minimum-inflated inlet area and the fairings are lines of constant values of drag coefficient. The radial fairings are lines of constant area ratio. These curves were generated from the empirical curves of figure 17 by reading the predicted area ratios for varying porosity at constant values of drag coefficient and computing the inlet area. Two effects can be observed from figure 18: (1) For a constant constructed exit area, the drag coefficient increases with increasing inlet area and (2) for a constant inflated minimum-inlet area, the drag coefficient increases with increasing exit area. In addition, the lines of constant area ratio in figure 18 show that at large values of  $A_i/A_e$  (i.e., values greater than 2.33) the drag coefficient is more sensitive to changes in constructed exit area; whereas at values of  $A_i/A_e$  less than 2.33 the drag coefficient is more sensitive to changes in inflated inlet area.

Since both the drag coefficient-area ratio relationship and the area ratio-measured reefing ratio relationship have been determined in equations (7) and (1), respectively, the dependence of drag coefficient on measured, inflated reefing ratio is found to be

$$C_{D_o} = 0.768 \eta^{0.3} (\xi_{inf})^{2.4} \quad (8)$$

and is represented by the faired curves which are ordered by geometric porosity in figure 19. These data show that the drag coefficient increases both with increasing  $\xi_{\text{inf}}$  at constant values of geometric porosity and with increasing geometric porosity at constant values of  $\xi_{\text{inf}}$ .

By substituting the relationship for  $\xi_{\text{inf}}$  in terms of  $\xi_{\text{const}}$  in equation (3) into equation (8), the drag coefficient can be defined completely in terms of constructed parameters and is

$$C_{D_0} = 0.768\eta^{0.3}(0.305 \ln \xi_{\text{const}} + 1.106)^{2.4} \quad (9)$$

The equation is valid only for porous canopies at  $M = 1.8$ . In figure 20 the faired curves which represent equation (9) are again ordered by porosity and are in fair agreement with the experimental data. The drag coefficient increases both with increasing constructed reefing ratio at constant values of porosity and with increasing porosity at constant values of constructed reefing ratio.

In order to extend the empirical prediction to include Mach number effects, data from the present investigation and from references 7, 9, 10, and 13 and from AEDC were used to establish the trend of the variation of drag coefficient with Mach number. Having determined the trend mainly from the data of unreefed parachutes, the level of the prediction was then normalized to the levels of the experimental data of the reefed parachutes and the following equation resulted:

$$C_{D_0} = \left( \frac{\eta}{M^2 - 1} \right)^{0.3} (0.305 \ln \xi_{\text{const}} + 1.106)^{2.4} \quad (10)$$

Although the variation of the aerodynamics of porous bodies with Mach number involves more complicated flow phenomena than are accounted for with this expression, this simple form seems to fit the trend of the data and is, therefore, thought to be appropriate. Comparisons of experimental data with the predicted drag coefficients from equation (10) are presented in figure 21. In general, the predicted drag coefficients at constant geometric porosity and reefing ratio are in good agreement with the trend and in fair agreement with the magnitudes of the experimental data.

In order to extend the empirical prediction to the transonic range, the singularity at  $M = 1.0$  was eliminated by modifying the Mach number expression in equation (10), so that

$$C_{D_0} = \left[ \frac{\eta}{(M^2 - 1) + 0.7} \right]^{0.3} (0.305 \ln \xi_{\text{const}} + 1.106)^{2.4} \quad (11)$$

Equation (11) provides a fair prediction of the drag coefficients in both the transonic and supersonic ranges, as can be seen in figure 22. This figure includes the data of the pres-

ent investigation and data from other investigations of comparable porosity parachutes. For further comparison of the empirical prediction of equation (11) with experimental data, figure 23 includes both the reference data from the previous figure and additional wind-tunnel and flight data for many varied canopy types. The diameters of the canopies ranged from 0.22 to 12.19 m and the geometric porosities ranged from 0.046 to 0.443; the effect of geometric porosity has been included in the ordinate parameter. Since there is insufficient information in the references to determine the inflated reefing ratio of the unreefed parachutes, the level of the empirical prediction cannot be evaluated in figure 23(a). However, the trend predicted by equation (11) is in good agreement with the variation of drag coefficient with Mach number for the reference data from the flight and wind-tunnel investigations. In addition, the drag coefficients for the majority of the unreefed parachutes fall within a band of reefing ratios (about 0.6 to 0.8) throughout the Mach number range, as would be expected.

In figure 23(b) (reefed parachutes), the drag coefficients for the hemisflo parachute with a 0.289 reefing ratio are overpredicted by equation (11). However, the majority of the data (the cross parachutes from ref. 7 and from AEDC and the hemisflo parachutes with the two largest reefing ratios from ref. 14) agree fairly well with the drag coefficients predicted by equation (11). Therefore, the predicted variation of drag coefficient with Mach number for various reefing ratios and geometric porosities, calculated by using equation (11), is corroborated in figure 23 both in trend by the reference data for unreefed parachutes and in magnitude by the reference data for reefed parachutes.

It should be noted at this point that as a result of the agreement between the empirical prediction of equation (11) and the experimental data, as shown in figures 22 and 23, the parameters having the dominant effects on drag coefficient are reefing ratio, geometric porosity, and Mach number. Suspension line length is recognized as an important parameter in parachute design, but it was not a variable in the present investigation. Other variables, such as canopy type, dynamic pressure, and stiffness (which generally varies with nominal diameter for a given canopy type), apparently have only a minor influence on the drag coefficients. Therefore, equation (11) could be used to provide a fair estimation of the drag coefficients at transonic and supersonic speeds for parachutes of specified porosity and reefing ratio. The drag coefficients of unreefed parachutes could also be predicted, by using equation (8), if the inflated reefing ratios ( $D_i/D_{max}$ ) were known from photographic data.

## CONCLUSIONS

An investigation was conducted at Mach 1.80 in the Langley 4-foot supersonic pressure tunnel to determine the effects of variation in reefing ratio and geometric porosity on the drag and stability characteristics of four basic canopy types deployed in the wake



of a cone-cylinder forebody. The basic designs included cross, hemisflo, disk-gap-band, and extended-skirt canopies; however, modular cross and standard flat canopies and a ballute were also investigated.

In general, the drag coefficient increased with increasing constructed reefing ratio and with increasing geometric porosity for the test range of porosities regardless of canopy design. Photographic data showed that, for all the canopies, the inflated reefing ratio attained during the test increased with increasing constructed reefing ratio. However, for the cross and hemisflo canopies, plateaus were reached such that further increases in constructed reefing ratio resulted in no substantial increase in inflated reefing ratio or drag coefficient.

In general, the canopies were fairly stable, with the exception of the cross canopies which experienced large drag variations due to both breathing and squidding of the canopy and coning motions of the parachute. Almost all the canopies exhibited some breathing and coning motions, but the amplitudes were less than those of the cross canopies.

An empirical correlation which provides a fair estimation of the drag coefficients in transonic and supersonic flow for parachutes of specified geometric porosity and reefing ratio was determined from the wind-tunnel data. Examination of the experimental measurements indicated that the parameters having the dominant effects on drag coefficient are reefing ratio, geometric porosity, and Mach number. Other variables, such as canopy type, dynamic pressure, and stiffness, apparently have only a minor influence on the drag coefficient.

Langley Research Center,  
National Aeronautics and Space Administration,  
Hampton, Va., December 16, 1974.

## APPENDIX A

### DETAILED DESCRIPTION OF THE DYNAMIC BEHAVIOR OF THE VARIOUS CONFIGURATIONS

Detailed descriptions of the dynamic behavior of the different configurations based on the photographic data and visual observations during the investigation are given in this appendix. Quantitative information obtained from the photographic data is given in tables IV and V.

#### Cross Canopies

The cross canopy parachutes, including configurations 19, 20, 28, 2, and 22, generally were somewhat unstable due to breathing, coning, and spinning motions, with the exception of configuration 22 which did not spin. The breathing frequency was sporadic and varied from about 70 to 125 Hz; the coning frequency was fairly constant at about 20 Hz; and the spinning frequency was about 20 Hz, with the exception of configuration 20 which was spinning at about 47 Hz.

During the breathing, there were extensive variations in the canopy shape and, as a result, in the behavior of the suspension lines and reefing line. The vents in the canopy typically became very narrow slits at the minimum canopy diameter and gaping openings at the maximum diameter. (See fig. 9.) At the minimum canopy diameter the suspension lines were extremely close together nearly forming a solid conical surface; as the maximum canopy diameter was approached, the suspension lines separated to the maximum spacing allowed by the canopy and reefing line. As the minimum canopy diameter (i.e., underinflation) was approached, the canopy tended to take a squidlike form and occasionally one or two of the suspension lines became slack and had a tendency to wrap together. However, during the subsequent canopy inflation, the suspension lines unwrapped and appeared to become taut. As the maximum canopy diameter (i.e., overinflation) was reached, the suspension lines occasionally bowed out, forming an extension of the canopy contour. During overinflation, the canopy had a rather small depth and a large inlet diameter. The reefing line generally was taut during breathing of configurations 19 and 20 (reefing ratios of 0.217 and 0.273); however, for canopies reefed at higher ratios, the reefing lines were not taut even when the canopies reached their maximum inflation. Nevertheless, the canopies with the larger reefing ratios (configurations 28, 2, and 22) maintained a fuller, more consistent inflation.

The cross canopies were observed during the investigation to have rather large coning angles compared with the other canopy types, consistent with observations of full-scale cross canopies as reported in reference 15. The canopy generally tended to align

## APPENDIX A

itself with the axis of symmetry of the suspension lines rather than the direction of the free-stream flow. In addition, there was a tendency for one of the panels to drift out from the generally symmetrical arrangement of the other three panels. This asymmetry, which was typical for the cross canopies, appeared to be related to the coning of the canopy and suspension lines.

### Modular Cross Canopy

The modular cross canopy (configuration 41) had a reefing ratio of 0.323 and twice as many suspension lines as the cross canopies, since it was constructed from two cross canopies. In contrast to the cross parachutes, this configuration was very stable.

### Hemisflo Canopies

The hemisflo canopies included configurations 26, 15, 16, 17, and 18 which had a geometric porosity of 0.085 and configurations 24, 12, 13, 25, 14, and 21 which had a geometric porosity of 0.147. No photographic data were obtained for configuration 17 as a result of operational difficulties. The hemisflo canopies were stable, having little or no coning and spinning and, generally, maintained a symmetric canopy shape. The photographic data indicated that all the hemisflo canopies were breathing, but the amplitude of the motion was quite small. The breathing frequency varied from approximately 100 to 200 Hz, and the canopy diameter changed very little and maintained a fully inflated shape. Two of these configurations, 26 and 18, did cone at a frequency of 67 and 30 Hz, respectively. These canopies became asymmetric during coning, but the coning motion involved mainly the canopy – there was no slackening of the suspension lines and essentially no movement of the suspension lines away from the system center line extending from the forebody. (In contrast, the coning experienced by the cross canopies involved both the canopy and suspension lines.) Ribbon flutter occurred just aft of the reefing line for all the reefed hemisflo configurations – indicating an underinflation in that part of the canopy. There was very little ribbon flutter in the canopy of configuration 27 (0.477 reefing ratio) and none in the canopy of configuration 18.

The hemisflo canopies with a 0.147 geometric porosity had breathing frequencies which varied from approximately 63 to 167 Hz. The coning frequencies averaged about 54 Hz for four configurations; configuration 24 had a much lower coning frequency (17 Hz) and configuration 21 experienced very little coning. The spinning frequency varied from approximately 6 to 17 Hz; configurations 12 and 21 did not spin. Generally, the characteristic behavior of the higher geometric-porosity hemisflo canopies was similar to that of the lower porosity hemisflo canopies; the magnitude of the canopy pulsations during breathing was quite small, the canopies remained fully inflated which resulted in very little ribbon flutter, and a uniform tension was maintained in the suspension lines. How-

## APPENDIX A

ever, configuration 14 (0.572 reefing ratio) exhibited extensive canopy pulsations in connection with the lowest breathing frequency (63 Hz) of any hemisflo canopy. As the canopy pulsed during breathing, the suspension lines behaved similarly to those of the cross canopies – tending to loose tension while at the minimum diameter conditions and to become bowed during overinflation. During coning the canopy shape developed asymmetry and, therefore, became underinflated in some regions of the canopy. The excess reefing line collected at one or two points and an extensive amount of ribbon flutter developed in the underinflated regions.

Configuration 21, which had no reefing line, had an unsteady breathing frequency – varying from 83 to 167 Hz. Coning was present, but insignificant; however, the canopy did develop some asymmetry with the accompanying underinflation and ribbon flutter. Configuration 29, which did not have continuous meridional tapes across the vent but was otherwise identical to configuration 21, behaved similarly to configuration 21 except the coning was more pronounced and the frequency was unsteady.

The large hemisflo canopy (configuration 42) had a breathing frequency of approximately 100 Hz, experienced a slight oscillation about the spin axis, and intermittently had a coning frequency of 10 Hz. The canopy developed an asymmetric shape but remained well inflated. The suspension lines occasionally became slack or bowed out, even though both the canopy coning and breathing were minor. Neither ribbon flutter nor spinning occurred.

### Extended-Skirt Canopies

The extended-skirt canopies, including configurations 8, 9, 10, and 11, had a breathing frequency which varied from approximately 125 to 200 Hz. The coning frequency varied from 56 to 83 Hz; and none of the canopies had any spin or oscillation about the spin axis. In addition, configuration 10 exhibited no coning.

Configurations 8 and 9 (reefing ratio of 0.18 and 0.279, respectively) were fairly stable, but had fairly large variations in canopy shape – incurring some canopy asymmetry and an occasional slack suspension line associated with coning. These two canopies did not develop well-inflated shapes but had excess, rumpled fabric just aft of the reefing line which resulted in continuous fabric flutter in that region. Configurations 10 and 11 maintained well-inflated shapes with an occasional slack suspension line. Fabric flutter, just aft of the canopy inlet, occurred for both canopies but was more extensive for configuration 11 which had no reefing line. In contrast to the cross canopies, during coning the extended-skirt canopies tended to align with the direction of the free-stream flow, rather than form an extension of the suspension lines.

## APPENDIX A

### Disk-Gap-Band Canopies

The disk-gap-band canopies, including configurations 39, 37, 31, and 34 which had a geometric porosity of 0.060, configurations 36, 30, and 32 which had a geometric porosity of 0.125, and configurations 38 and 33 which had a geometric porosity of 0.20, were generally quite stable and remained relatively symmetric. The breathing frequencies varied from approximately 100 to 200 Hz and the coning frequency was similar for all configurations at approximately 56 Hz. None of these canopies exhibited any spinning; however, several canopies did oscillate slightly about the spin axis.

Configurations 39 and 37 (band reefing ratio of 0.159 and 0.254, respectively) and configuration 31 (no reefing line) had well-inflated canopies and fairly well inflated bands. The reefed-band canopies exhibited some flutter in the aft regions of the band and the forward regions of the disks. Configuration 31 exhibited some flutter in the forward regions of the band. Although there was an occasional slight asymmetry between the band and disk, the small amount of coning allowed the system to remain relatively symmetric with respect to the extended forebody center line. Consequently, the suspension lines remained taut. As the maximum inflated disk diameter of configuration 39 was reached during breathing, the band followed and formed a smooth extension of the disk – fully inflated and well scalloped. However, as the minimum disk diameter was approached, the band decreased in inflated diameter but tended to neck down at about two-thirds of the bandwidth distance aft of the band leading edge. The band diameter aft of the necked-down region increased toward the disk inlet diameter and formed a spherically shaped extension of the inflated disk.

Configuration 34 (reefed on the disk to a ratio of 0.254) developed asymmetry between band and disk more frequently due to the more pronounced coning of this canopy than any of the other 0.06-geometric-porosity canopies. Consequently, the suspension lines were rather unstable and occasionally became slack. At one time during the coning, the canopy was stationary, remaining essentially on the forebody extended center line, and the suspension lines were moving in a manner similar to the motion they experienced during coning – but as if the lines were fixed at both ends. Both the disk and the band remained fairly well inflated and there was no flutter in the disk or band.

Configuration 36, which was reefed on the band to a ratio of 0.254 and had a geometric porosity of 0.125, had a very small amount of breathing and coning. The disk and band remained relatively symmetrical with respect to each other and, also, to the extended forebody longitudinal center line. The disk was well inflated, but the band was slightly underinflated, had some flutter in the gores, and did not form a smooth extension of the disk. Frequently, the disk and band of configuration 30 (no reefing line) became skewed even though the canopy and suspension lines were symmetric with respect to the extension of the forebody longitudinal center line. The disk maintained a well-inflated

## APPENDIX A

shape with no fabric flutter. The band – which had a moderate amount of flutter at all times – assumed a well-inflated shape and formed a good extension of the inflated disk as the disk reached the maximum breathing diameter. However, as minimum breathing diameter of the disk was approached, the band became underinflated, crumpled, lost its scalloped shape, and no longer formed a good extension of the inflated disk.

For configuration 32 (0.125 geometric porosity and reefed on the disk at a ratio of 0.254), the breathing occurred only in the band and there was no significant flutter in the band or the disk. The larger geometric porosity and the reefing line located at the disk leading edge allowed the band to assume a much larger diameter than the inflated disk. The band occasionally was fully inflated and well scalloped; however, it also became underinflated and did not maintain a circular shape. Large coning angles and one or two slack suspension lines frequently resulted when the band opened to a fully inflated shape.

Configuration 38 (0.20 geometric porosity and a band reefing ratio of 0.254) was quite stable with little breathing and coning. Both the disk and band were well inflated and well scalloped with a slight amount of flutter in the band. The band did not form a good extension of the inflated disk – probably due to the larger gap width at this geometric porosity. Configuration 33 (no reefing) was relatively unstable compared with configuration 38. The breathing was negligible, but there was a significant amount of erratic coning reaching large coning angles and allowing the band to develop asymmetry with respect to the disk. The disk was well inflated, but the band frequently became underinflated and nearly collapsed in some regions with the nearby suspension lines becoming slack and twisting together. However, as the band reinflated, the suspension lines would untwist and regain their tension.

### Standard Flat Canopy

Configuration 40 was extremely unstable and had erratic coning at large angles. The breathing frequency was difficult to determine because of the large amount of coning. However, there was a pronounced longitudinal motion which appeared to be an extreme version of breathing: The canopy shape varied from completely collapsed with fully extended suspension lines to an essentially flat disk with totally slack suspension lines. Infrequently, short periods did occur during which the canopy was relatively stable with only moderate coning. Eventually, the riser line failed due to snap loading and the parachute was lost.

## APPENDIX B

### DETAILED DESCRIPTION OF SHOCK-WAVE PATTERNS OF THE VARIOUS CONFIGURATIONS

Detailed descriptions of the shock-wave patterns of the different configurations, based on the schlieren photographic data, are given in this appendix. Selected schlieren photographs of the various configurations are presented in figure 9.

#### Cross Canopies

The shock-wave pattern for the cross canopies generally consisted of the double shock-wave system, which was discussed previously. However, the shock-wave pattern was more complex for the cross canopies with reefing ratios greater than 0.40. (See configurations 2, 3, and 22 shown in fig. 9(a).) The two basic shock waves mentioned previously were present, but the downstream shock wave was a bow shock which, depending on the canopy inlet diameter, moved upstream joining either partially or completely with the upstream shock wave, just ahead of the canopy inlet, or stood just inside the canopy inlet. When the downstream shock wave was inside the canopy, rather weak, oblique shock waves could be seen which were attached externally to the canopy inlet lip. (See fig. 9(a) – configuration 22.) The schlieren movies of these configurations showed that the bow shock wave popped in and out of the canopy in direct correspondence to the canopy breathing. As the canopy approached its maximum inflated diameter in breathing, the shock wave moved out in front of the canopy inlet; as breathing continued, the canopy decreased to its minimum diameter with decreased inlet diameter and the shock wave moved into the canopy (i.e., was swallowed by the canopy). The schlieren movies showed that at minimum inlet diameter the canopy assumed a shape that was similar to the configurations that were reefed. The upstream shock-wave position and included angle also varied with changing canopy diameter and the changing included angle of the suspension lines during canopy breathing.

The preceding discussion applied to configurations which either were not coning or were coning such a small amount that the canopy remained within the symmetric flow field of the forebody. When the canopy moved out of this symmetric flow field (e.g., during pronounced coning), a portion or all the canopy and suspension lines could have been exposed to several different flow fields due to the presence of the forebody and struts. Generally, the large coning angles experienced by the cross canopies resulted in substantial asymmetry in the shock-wave patterns. During coning, both the upstream and downstream shock waves on the windward side became somewhat bowed near the suspension

## APPENDIX B

lines and also near the inlet lip on the leeward side of the canopy; however, these shock waves remained essentially oblique.

### Modular Cross Canopy

The modular cross canopy (configuration 41) had essentially the same double shock-wave pattern as the cross parachutes (during their short periods of stability).

### Hemisflo Canopies

The shock-wave pattern for the hemisflo canopies, shown for configuration 18 at four different times in figure 9(b), had essentially the same basic double shock-wave pattern. Frequently, however, there would appear to be a "ball of air" moving with a circular motion around the inside of the hemisflo canopies. This phenomenon occurred only in canopies which were reefed at the lower ratios below 0.30 (i.e., configurations 26, 15, 24, and 12). The larger portion of the canopy that the ball of air occupied was well inflated, but the remainder of the canopy was underinflated and exhibited ribbon flutter. The movement of this ball of air in the canopy appeared to be related to a coning motion - the suspension lines developed an angle, as if the system was coning, but the ball of air in the canopy remained on the extended forebody center line producing an asymmetric canopy shape. At these lower reefing ratios, generally, the downstream shock wave had been swallowed by the canopy.

### Extended-Skirt Canopies

The shock-wave pattern for the extended-skirt canopies generally consisted of the double shock-wave system as shown in figure 9(d). An additional shock wave occasionally appeared on the canopy due to some asymmetry in the canopy contour. As the unreefed canopy of configuration 11 approached its maximum inflated diameter during breathing, the upstream shock wave moved further upstream and merged with the shock wave emanating from the confluence point. The other extended-skirt canopies (configurations 8, 9, and 10) exhibited the same upstream shock-wave movement but to a lesser degree. The downstream shock wave generally appeared to stand at the canopy inlet; however, the 16 suspension lines frequently blocked out the flow details enclosed by the lines.

### Disk-Gap-Band Canopies

The shock-wave pattern of the disk-gap-band canopies (fig. 9(c)) which either had a reefing line at the band leading edge or were not reefed, consisted of the three shock waves discussed previously for this type of canopy. A fourth shock wave occurred both symmetrically, when the canopy assumed a light-bulb shape, and asymmetrically, when



## APPENDIX B

one section of the band assumed a concave shape between leading and trailing edges and the diametrically opposite section of the band assumed a convex shape. The asymmetry occurred mainly during coning when band and disk became misaligned. Configuration 33, which was unreefed and had a 0.20 geometric porosity, had a double shock-wave system consisting of a conical shock wave from the suspension lines and a bow shock wave ahead of the band. Immediately following the shock-wave pattern just described, the bow shock was swallowed and a conical shock wave formed at the leading edge of the disk. Additional undesirable characteristics of this large geometric porosity canopy were occasional extensive coning, extreme disk-band asymmetry, and extensive band flutter. Apparently, the gap for this geometric porosity was so large that the band no longer acted as an extension of the disk (i.e., it was no longer effective in providing stability).

Configurations 34 and 32 were both reefed to the same ratio at the leading edge of the disk rather than the band. These parachutes had a double shock-wave system: a conical shock wave from the suspension lines and a bow-conical combination shock wave from the band leading edge. The band shock wave for configuration 34 (0.06 geometric porosity) was generally much stronger than the band shock wave for configuration 32, which had a geometric porosity double that of configuration 34 (i.e., less resistance to mass flow). A third shock wave occasionally formed near the disk leading edge of the larger porosity canopy. (See lower right photograph of configuration 32 in fig. 9(c).)

### Standard Flat Canopy

The standard flat canopy (configuration 40), which consisted of the disk from one of the disk-gap-band canopies, had the basic double shock-wave pattern – a conical shock wave from the suspension lines and a bow shock wave immediately upstream of this canopy inlet.

## REFERENCES

1. Fredette, R. O.: Parachute Research Above Critical Aerodynamic Velocities. P-1031C (Contracts AF 33(616)-3346, AF 33(038)-10653, AF 33(616)-5507, and AF 33(616)-5991), Cook Res. Lab., Cook Elec. Co., c.1961.
2. Heinrich, H. G.; Rose, R. E.; and Kovacevic, N. D.: Flow Characteristics of Rigid Ribbon Parachute Canopies in Supersonic Flow. AFFDL-TR-65-100, U.S. Air Force, Dec. 1965. (Available from DDC as AD 478 442.)
3. Roberts, B. G.: An Experimental Study of the Drag of Rigid Models Representing Two Parachute Designs at  $M = 1.40$  and  $2.19$ . C.P. No. 565, Brit. A.R.C., Dec. 1960.
4. Maynard, Julian D.: Aerodynamic Characteristics of Parachutes at Mach Numbers From 1.6 to 3. NASA TN D-752, 1961.
5. Braslow, Albert L.; and Knox, Eugene C.: Simplified Method for Determination of Critical Height of Distributed Roughness Particles for Boundary-Layer Transition at Mach Numbers From 0 to 5. NACA TN 4363, 1958.
6. Braslow, Albert L.; Hicks, Raymond M.; and Harris, Roy V., Jr.: Use of Grit-Type Boundary-Layer-Transition Trips on Wind-Tunnel Models. NASA TN D-3579, 1966.
7. Homan, M. L.: Aerodynamic Characteristics of Several Flexible Decelerators at Mach Numbers From 1.8 to 2.5. AEDC-TR-71-6, U.S. Air Force, Jan. 1971. (Available from DDC as AD 879 024.)
8. Reichenau, David E. A.: Wake Properties Behind an Ejection Seat Escape System and Aerodynamic Characteristics With Stabilization Parachutes at Mach Numbers From 0.6 to 1.5. AEDC-TR-71-30, U.S. Air Force, Feb. 1971. (Available from DDC as AD 880 650.)
9. Galigher, Lawrence L.: Investigation of F-111 Crew Module Stabilization Parachute Models at Mach Numbers of 0.5, 2.0, 2.2, and 2.5. Phase I. AEDC-TR-65-83, U.S. Air Force, Apr. 1965. (Available from DDC as AD 461 730.)
10. Deitering, J. S.; and Hilliard, E. E.: Wind Tunnel Investigation of Flexible Aerodynamic Decelerator Characteristics at Mach Number 1.5 to 6. AEDC-TR-65-110, U.S. Air Force, June 1965. (Available from DDC as AD 464 786.)
11. Foughner, Jerome T., Jr.; and Alexander, William C.: Wind-Tunnel Tests of Modified Cross, Hemisflo, and Disk-Gap-Band Parachutes With Emphasis in the Transonic Range. NASA TN D-7759, 1974.

12. Alexander, William C.; and Foughner, Jerome T., Jr.: Drag and Stability Characteristics of High-Speed Parachutes in the Transonic Range. AIAA Paper No. 73-473, May 1973.
13. Bobbitt, P. J.; Mayhue, R. J.; Faurote, G. L.; and Galigher, L. L.: Supersonic and Subsonic Wind-Tunnel Tests of Reefed and Unreefed Disk-Gap-Band Parachutes. AIAA Paper No. 70-1172, Sept. 1970.
14. Deitering, J. S.: Performance of Flexible Aerodynamic Decelerators at Mach Numbers From 1.5 to 6. AEDC-TDR-63-119, U.S. Air Force, July 1963. (Available from DDC as AD 338 412.)
15. Murrow, Harold N.; and McFall, John C., Jr.: Summary of Experimental Results Obtained From the NASA Planetary Entry Parachute Program. AIAA Paper No. 68-934, Sept. 1968.
16. Charczenko, Nickolai: Wind-Tunnel Investigation of Drag and Stability of Parachutes at Supersonic Speeds. NASA TM X-991, 1964.
17. Anon.: Study and Exploratory Free-Flight Investigation of Deployable Aerodynamic Decelerators Operating at High Altitudes and at High Mach Numbers. FDL-TDR-64-35, Vol. I, U.S. Air Force, July 1964. (Available from DDC as AD 606 569.)
18. Eckstrom, Clinton V.: Flight Test of a 40-Foot-Nominal-Diameter Disk-Gap-Band Parachute Deployed at a Mach Number of 3.31 and a Dynamic Pressure of 10.6 Pounds Per Square Foot. NASA TM X-1924, 1970.
19. Reichenau, David E. A.: Investigation of Various Full-Scale Parachutes at Mach Number 3.0. AEDC-TR-65-241, U.S. Air Force, Dec. 1965. (Available from DDC as AD 474 473.)
20. Bloetscher, F.; and Arnold, W. V.: Aerodynamic Deployable Decelerator Performance-Evaluation Program. Phase III. AFFDL-TR-67-60, U.S. Air Force, Oct. 1967. (Available from DDC as AD 823 864.)

TABLE I. - DECELERATOR SYSTEM SPECIFICATIONS

## (a) Canopy

Canopy type	Nominal diameter, cm	Porosity	Number of canopy legs	Number of gores	Band width, cm	Band length, cm	Cloth material	Weight, N/m <sup>2</sup>	Cloth rated strength - warp, N/cm	Cloth rated strength - fill, N/cm
Cross	30.48	0.413	4	—	8.05	30.48	Nylon - dobby taffeta	1.264	332.74	Unknown
Modular cross	30.48	0.086	8	—	8.05	30.48	Nylon - dobby taffeta	1.264	332.74	Unknown
Disk-gap-band	25.40	0.060	—	18	—	—	Dacron - square weave	0.748	140.1	140.1
	25.40	0.125	—	18	—	—	Dacron - square weave	0.748	140.1	140.1
	25.40	0.200	—	18	—	—	Dacron - square weave	0.748	140.1	140.1
Extended skirt	40.64	—	—	16	—	—	Dacron - square weave	0.748	140.1	140.1
Standard flat	18.49	—	—	18	—	—	Dacron - square weave	0.74	140.1	140.1

TABLE I.- DECELERATOR SYSTEM SPECIFICATIONS - Continued

(a) Canopy - Concluded

Canopy type	Nominal diameter, cm	Porosity	Number of gores	Number of horizontal ribbons	Horizontal ribbon spacing, cm	Horizontal ribbon width, cm	Horizontal ribbon military specification	Horizontal ribbon strength, N	Vertical ribbon width, cm	Vertical ribbon military specification	Vertical ribbon strength, N	Radial ribbon width, cm	Radial ribbon material	Radial ribbon strength, N
Hemisflo	25.40	0.085	12	12	0.152	0.635	Nylon	MIL-R-5608 Class C Type II	0.396	MIL-T-5038	311.38	0.635	Nylon	173.48
	25.40	0.147	12	11	0.254	0.953	Nylon	MIL-R-5608 Class C Type II	0.396	MIL-T-5038	311.38	0.635	Nylon	173.48
	33.02	0.147	16	23	0.102	0.635	Nylon	MIL-R-5608 Class C Type I	0.330	—	355.86	0.635	Nylon	173.48



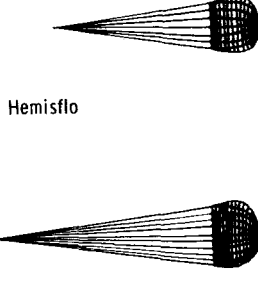



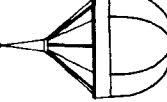
Canopy type	Nominal diameter, cm	Number of gores	Constructed nose apex angle, deg	Constructed aft-end shape	Cloth material	Weave	Weight, N/m <sup>2</sup>	Cloth rated strength - warp, N/cm	Cloth rated strength - fill, N/cm	Cloth military specification	Number of inlets	Inlet diameter, cm	Band strength - fill, N/cm	Band weight, N/m <sup>2</sup>	Band military specification
Ballute	Inflated 20.32	6	90	Hemisphere	Nylon "ripstop" calendered	Square	0.366	73.55	73.55	MIL-C-70200 Type I	24	1.27	472.84	1.330	MIL-C-43128

TABLE I. - DECELERATOR SYSTEM SPECIFICATIONS - Concluded

(b) Suspension lines and reefing lines

Canopy and Support Lines													
Canopy type	Suspension lines					Reefing lines			Reefing rings				
	Number of lines	Line length, cm	Rated strength, V	Material	Material military specification	Rated strength, N	Material	Material military specification	Number of rings	Ring inside diameter, cm	Ring outside diameter, cm	Ring length, cm	Material
Cross	12	42.67	222.41	Nylon tubular braid	MIL-C-17183 Revision B	1334.47	Dacron cord-coreless	MIL-C-7515B	12	0.465	0.635	0.318	Aluminum
Modular cross	24	42.67	222.41	Nylon tubular braid	MIL-C-17183 Revision B	1334.47	Dacron cord-coreless	MIL-C-7515B	24	0.465	0.635	0.318	Aluminum
Hemisflo	12	38.10	444.82	Nylon cord - shrouded	MIL-C-5040 Type I	1334.47	Dacron cord-coreless	MIL-C-7515B	12	0.465	0.635	0.318	Aluminum
	16	54.89	444.82	Nylon cord - shrouded	MIL-C-5040 Type I	—	—	—	—	—	—	—	—
Disk-gap-band	18	25.40	444.82	Nylon cord - shrouded	MIL-C-5040 Type I	1334.47	Dacron cord-coreless	MIL-C-7515B	18	0.465	0.635	0.318	Aluminum
Extended skirt	16	40.64	444.82	Nylon cord - shrouded	MIL-C-5040 Type I	1334.47	Dacron cord-coreless	MIL-C-7515B	16	0.465	0.635	0.318	Aluminum
Standard flat	18	25.40	444.82	Nylon cord - shrouded	MIL-C-5040 Type I	—	—	—	—	—	—	—	—
Ballute	6	19.05	355.86	Nylon-shroud only	MIL-C-5040 Type III	—	—	—	—	—	—	—	—

TABLE II. - GEOMETRIC CHARACTERISTICS AND DRAG DATA OF PARACHUTES

Canopy type	Configuration number	Constructed reefing ratio	Geometric porosity	x/d	D <sub>0</sub> /d	Drag, N	C <sub>D0</sub> (a)	C <sub>D0</sub> A <sub>0</sub> m <sup>2</sup>	Reefing line length, m	Dynamic pressure, kN/m <sup>2</sup>
Cross 	19	0.217	0.413	8.40	5.04	131.954	0.257	0.0109	0.208	12.1
	20	.273	↓	↓	↓	158.304	.308	.0131	.262	↓
	28	.323	↓	↓	↓	198.319	.386	.0164	.310	↓
	2	.410	↓	↓	↓	257.948	.504	.0214	.394	↓
	3	.547	↓	↓	↓	217.952	.426	.0180	.523	↓
	22	.547	↓	↓	↓	210.866	.411	.0175	.523	↓
	23	.273	↓	6.38	↓	177.920	.347	.0148	.262	↓
Modular cross 	41	.323	.086	8.40	↓	160.542	.199	.0133	.310	↓
Hemisflo 	26	0.261	0.085	7.65	4.20	114.847	0.187	0.00948	0.208	12.1
	15	.286	↓	↓	↓	115.159	.187	.00948	.229	↓
	16	.429	↓	↓	↓	155.511	.254	.0128	.343	↓
	27	.477	↓	↓	↓	164.576	.270	.0137	.381	↓
	17	.572	↓	↓	↓	185.855	.304	.0154	.457	↓
	18	unreefed	↓	↓	↓	186.865	.303	.0153	unreefed	↓
	24	.261	.147	↓	↓	117.930	.192	.00975	.208	↓
	12	.286	↓	↓	↓	131.728	.214	.0109	.229	↓
	13	.429	↓	↓	↓	175.549	.286	.0145	.343	↓
	25	.477	↓	↓	↓	180.749	.295	.0150	.381	↓
	14	.572	↓	↓	↓	197.785	.321	.0163	.457	↓
	21	unreefed	↓	↓	↓	162.334	.265	.0134	unreefed	↓
	29	unreefed	↓	↓	↓	177.422	.289	.0147	unreefed	↓
	42	unreefed	↓	10.42	5.46	416.915	.401	.0344	unreefed	↓
Extended skirt 	8	0.180	—	8.07	6.72	125.540	0.144	0.0187	0.229	6.8
	9	.279	—	↓	↓	147.344	.169	.0217	.356	↓
	10	.358	—	↓	↓	150.262	.173	.0223	.457	↓
	11	unreefed	—	↓	↓	167.908	.193	.0250	unreefed	↓
Disk-gap-band 	39	0.159	0.060	5.55	4.20	69.304	0.113	0.00567	0.127	12.1
	37	.254	↓	↓	↓	79.446	.130	.00660	.203	↓
	31	unreefed	↓	↓	↓	174.998	.285	.0144	unreefed	↓
	34	<sup>b</sup> .254	↓	↓	↓	88.880	.145	.00734	.203	↓
	36	.254	.125	↓	↓	77.911	.126	.00641	.203	↓
	30	unreefed	↓	↓	↓	107.490	.175	.00883	unreefed	↓
	32	<sup>b</sup> .254	↓	↓	↓	82.635	.135	.00678	.203	↓
	38	.254	.200	↓	↓	91.647	.150	.00762	.203	↓
Standard flat 	40	unreefed	—	6.22	3.06	185.268	0.715	0.0153	unreefed	12.1
Ballute 	35	—	—	4.50	3.36	361.720	0.929	0.0299	—	12.1

<sup>a</sup>Drag coefficient of cross and modular cross canopies computed using fabric surface area.

<sup>b</sup>Reefing line located at leading edge of disk for configurations 32 and 34.

TABLE III. - AVERAGED, MEASURED PARAMETERS FROM PHOTOGRAPHIC DATA


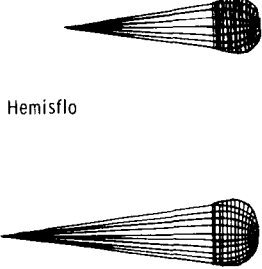


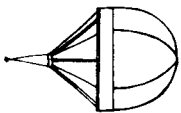
Canopy type	Configuration number	$D_i$ , m	Max. inlet diameter, m	$D_{max}$ , m	Max. canopy depth, m	$\epsilon_{inf}$	$\epsilon$	$\frac{D_{max}}{D_o}$	Max. canopy depth $\frac{D_{max}}{D_{max}}$	Max. inlet diameter $\frac{D_{max}}{D_{max}}$
<p>Cross</p> 	19	0.0702	0.0702	0.1110	0.1109	0.632	0.231	0.364	0.999	0.632
	20	.0833	.0864	.1176	.1124	.709	.274	.386	.956	.734
	28	.1074	.1144	.1287	.1130	.834	.353	.422	.859	.889
	2	.1162	.1281	.1339	.1083	.868	.382	.439	.844	.957
	3	.1182	.1229	.1319	.1088	.896	.388	.433	.821	.932
	22	.1179	.1179	.1324	.1082	.891	.387	.434	.817	.891
	23	.0859	.0859	.1149	.1106	.748	.282	.377	.947	.748
	41	.1071	.1173	.1417	—	.756	.352	.465	—	.828
Modular cross										
<p>Hemisflo</p> 	26	0.0667	0.0774	0.1013	0.1018	0.659	0.263	0.399	1.005	0.764
	15	.0827	.0899	.1124	.0998	.736	.326	.443	.888	.799
	16	.1092	.1143	.1292	.0955	.846	.430	.509	.739	.884
	27	.1103	.1127	.1271	.0944	.868	.434	.500	.743	.887
	17	—	—	—	—	—	—	—	—	—
	18	.1171	.1171	.1318	.0952	.889	.461	.519	.723	.889
	24	.0783	.0880	.1066	.1018	.734	.308	.420	.954	.826
	12	.0768	.0807	.1072	.1033	.716	.302	.422	.963	.753
	13	.1037	.1110	.1231	.0986	.843	.409	.485	.801	.902
	25	.1129	.1185	.1286	.0949	.878	.445	.506	.738	.922
	14	.1130	.1158	.1307	.0955	.865	.445	.515	.731	.886
	21	.1147	.1159	.1290	.0940	.889	.452	.508	.728	.898
	29	.1149	.1182	.1295	.0911	.887	.452	.510	.704	.913
	42	—	—	—	—	—	—	—	—	—
	—	—	—	—	—	—	—	—	—	—
	—	—	—	—	—	—	—	—	—	—
<p>Extended skirt</p> 	8	0.0859	0.1062	0.1554	—	0.553	0.212	0.382	—	0.683
	9	.1207	.1434	.1783	—	.677	.297	.439	—	.804
	10	.1476	.1758	.1953	—	.765	.363	.481	—	.900
	11	.1732	.1862	.2084	—	.831	.426	.513	—	.893
	—	—	—	—	—	—	—	—	—	—
<p>Disk-gap-band</p> 	39	0.0588	0.0755	0.1011	0.0950	0.581	0.232	0.398	0.940	0.747
	37	.0693	.0807	.1078	.0896	.643	.273	.424	.831	.749
	31	.1088	.1200	.1287	.0823	.845	.428	.507	.640	.933
	34	.0928	.1112	.0972	.0515	.955	.365	.382	.530	1.144
	36	.0696	.0803	.1123	.0904	.620	.274	.442	.805	.715
	30	.0841	.0947	.1115	.0790	.754	.331	.439	.709	.850
	32	.0797	.0957	.0909	.0536	.876	.314	.358	.590	1.052
	38	.0708	.0832	.1088	.0895	.651	.279	.428	.823	.765
	33	.1046	.1159	.1267	.0870	.826	.412	.499	.687	.915
	—	—	—	—	—	—	—	—	—	—
Standard flat										
Ballute										
<p>Ballute</p> 	40	—	—	—	—	—	—	—	—	—
	35	0.0502	—	0.1909	0.2164	—	—	—	—	—



TABLE IV.- MEASURED PARAMETERS FROM PHOTOGRAPHIC AND  
OSCILLOGRAPHIC DATA





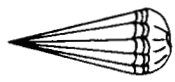
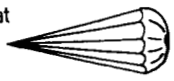
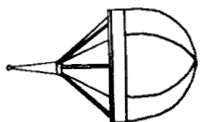







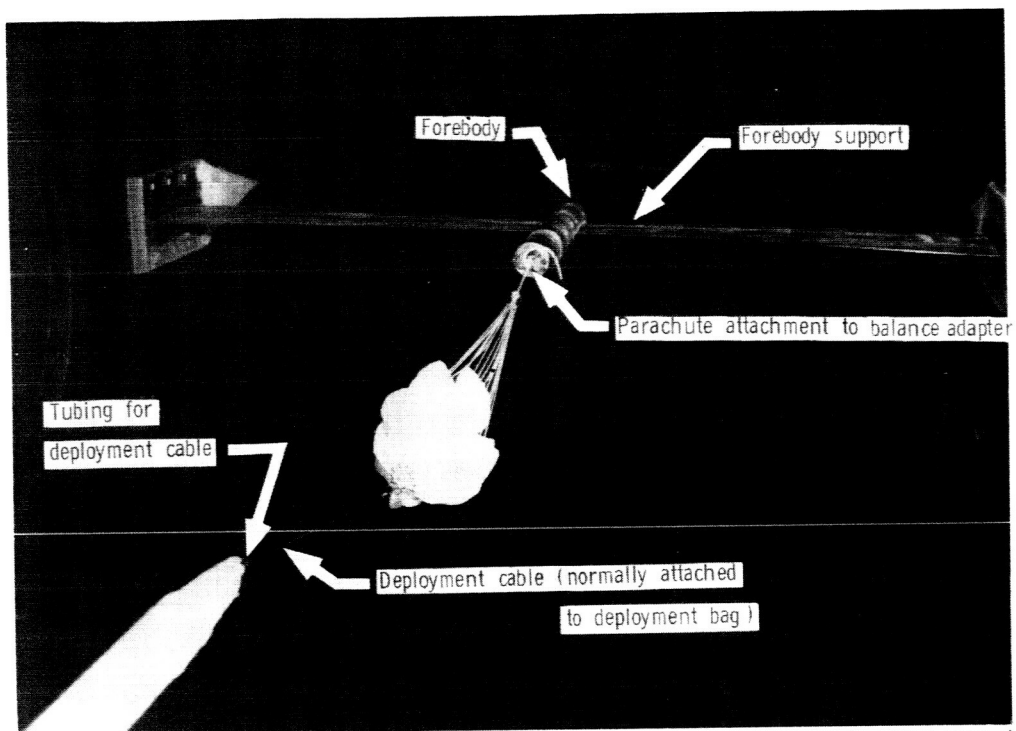
Canopy type	Configuration number	$A_e$ m <sup>2</sup>	$A_i$ m <sup>2</sup>	$\frac{A_i}{A_e}$	$C_{D_i}$	Max. angular deflection, deg
Cross 	19	0.0302	0.0039	0.129	2.809	2.5
	20		.0059	.196	2.236	0
	28		.0103	.342	1.592	5.0
	2		.0106	.352	2.019	12.0
	3		.0110	.365	1.636	6.0
	22		.0109	.362	1.606	2.0
	23		.0058	.192	2.552	5.0
Modular cross 	41	.00627	.0108	1.722	1.232	0
Hemisflo 	26	0.00431	0.0035	0.813	2.709	0
	15		.0054	1.249	1.762	2.0
	16		.0094	2.178	1.365	1.5
	27		.0096	2.221	1.433	0
	17		-	-	-	-
	18		.0108	2.506	1.417	1.0
	24	.00745	.0047	.647	2.601	1.0
	12		.0046	.622	2.354	2.5
	13		.0085	1.136	1.714	1.5
	25		.0100	1.345	1.500	4.0
	14		.0100	1.349	1.630	2.0
	21		.0103	1.389	1.301	1.0
	29		.0110	1.475	1.336	2.0
Extended skirt 	42	.0126	—	—	—	0
	8	—	0.0089	—	2.111	4.0
	9	—	.0162	—	1.340	0
	10	—	.0243	—	.918	0
	11	—	.0272	—	.919	0
Disk-gap-band 	39	0.00304	.0027	0.893	2.085	0
	37		.0038	1.241	1.746	0
	31		.0093	3.056	1.548	3.0
	34		.0068	2.223	1.084	0
	36	.00634	.0038	.601	1.682	0
	30		.0056	.877	1.588	1.0
	32		.0072	1.135	.943	0
	38	.0101	.0039	.389	1.934	0
	33		.0086	.849	1.824	1.5
Standard flat 	40	—	—	—	—	10.0
Ballute 	35	—	—	—	—	3.0

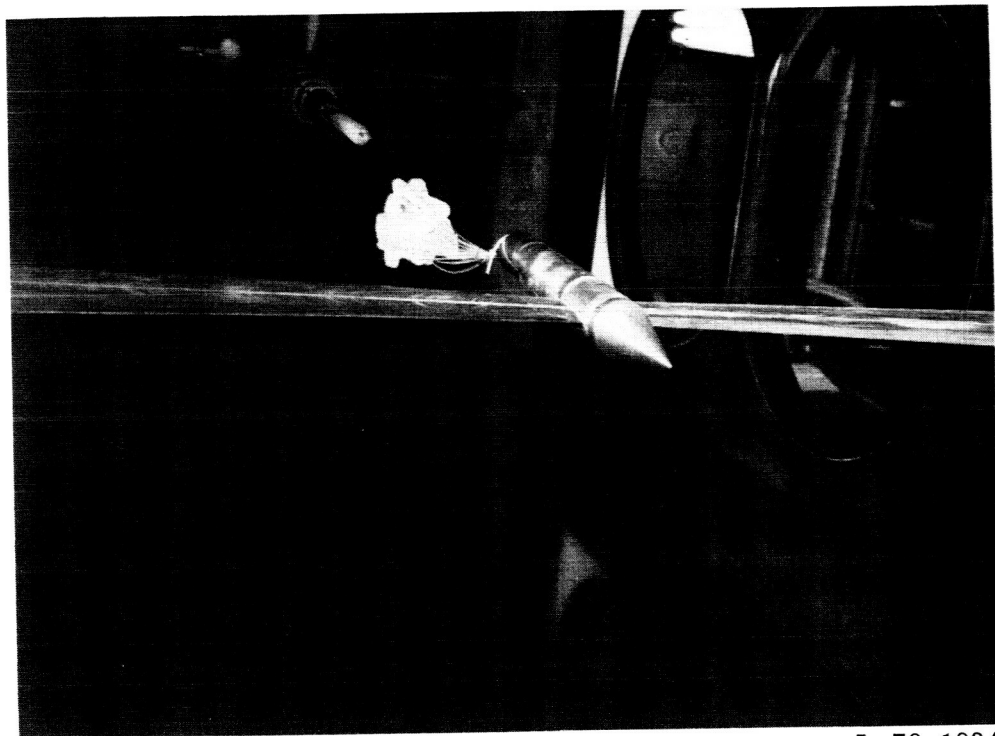
TABLE V.- MEASUREMENTS OF AND COMMENTS ON DYNAMIC BEHAVIOR OF PARACHUTES

Canopy type	Configuration number	Breathing frequency, Hz	Coning frequency, Hz	Spinning frequency, Hz	Comments
 Cross	19	80 to 100	20	18	Extensive breathing and variation in canopy and vent shapes; fairly large coning angle
	20	125	29	47	Good inflation; some canopy asymmetry; taut reefing and suspension lines
 Modular cross	2	100	22	25	Extremely large coning angle; frequent slack reefing line; canopy asymmetry
	3	71 to 100	19	8	Moderately large coning angle; slack reefing line; fairly good canopy inflation
	22	100	20	17	Good inflation; excess reefing line
	23	67 to 80	17	None	Good inflation; large variation in canopy shape - frequent asymmetry
	41	125	20	21	Large coning angle; extensive canopy asymmetry
 Hemisfla	26	143 to 167	67	10	Fairly good inflation; little fabric flutter; frequent variation in canopy shape
	15	167 to 200	Generally none	None	Extremely stable; very little change in canopy shape
	16	167 to 200	None	8	Good inflation; very little fabric flutter
	27	Small deviations	—	—	—
	18	100	30	6	Canopy asymmetry during coning
	24	143	17	11	Good inflation - very little fabric flutter; taut suspension lines
	12	142	48	None	Fairly well inflated; frequent canopy asymmetry
	13	125	59	8	Good inflation; canopy asymmetry during coning
	25	71 to 83	59	17	Good inflation; canopy asymmetry during coning
	14	63	50	6	Extensive breathing; poor inflation; extensive coning; taut reefing and suspension lines
 Extended skirt	21	125 to 167	None	None	Fairly well inflated; some fabric flutter; some canopy asymmetry
	29	67	7	10	Good inflation; some fabric flutter; extensive canopy asymmetry
	42	100	10	Occasional slight roll	Good inflation; extensive canopy asymmetry; occasional slack suspension line
	8	167	83	None	Canopy underinflated with some shape asymmetry
	9	125	56	None	Canopy underinflated - asymmetric shape; occasional slack suspension line
 Disk-gap-band	10	167 to 200	None	None	Fairly well inflated; some fabric flutter
	11	167 to 200	77	None	Good inflation; fairly extensive fabric flutter; occasional slack suspension line
	39	133 to 200	55	Very slight roll	Fairly stable; well inflated; fabric flutter in band and at inlet of disk
	37	100	56	None	Well inflated; extremely stable; asymmetry between band and disk
	31	180	56	None	Disk well inflated; band fairly well inflated
	34	167 to 200	58	None	Disk well inflated; excess reefing line; frequent asymmetry and slack suspension lines
	36	167 to 200	58	Very slight roll	Extremely stable; good disk inflation - fair inflation in band; band-disk symmetry maintained
	30	100	56	None	Disk well inflated; band underinflated; frequent band-disk asymmetry
	32	67 to 80	58	Very slight roll	Fairly good inflation; asymmetric band shape; occasional slack suspension lines
	38	160	56	Very slight roll	Good inflation; stable; slight amount of fabric flutter in band
 Standard flat	33	100	55	Very slight roll	Disk well inflated; band underinflated; frequently one or two slack suspension lines
	40	—	—	—	Extremely unstable; extensive irregular coning and breathing; riser line failed
 Ballute	35	20	45	None	Extremely stable; good inflation; decrease in apex angle during test - little effect on stability



L-70-1032.1

(a) View of installation looking upstream.



L-70-1034

(b) View of installation looking downstream.

Figure 1.- Installation of model in test section.

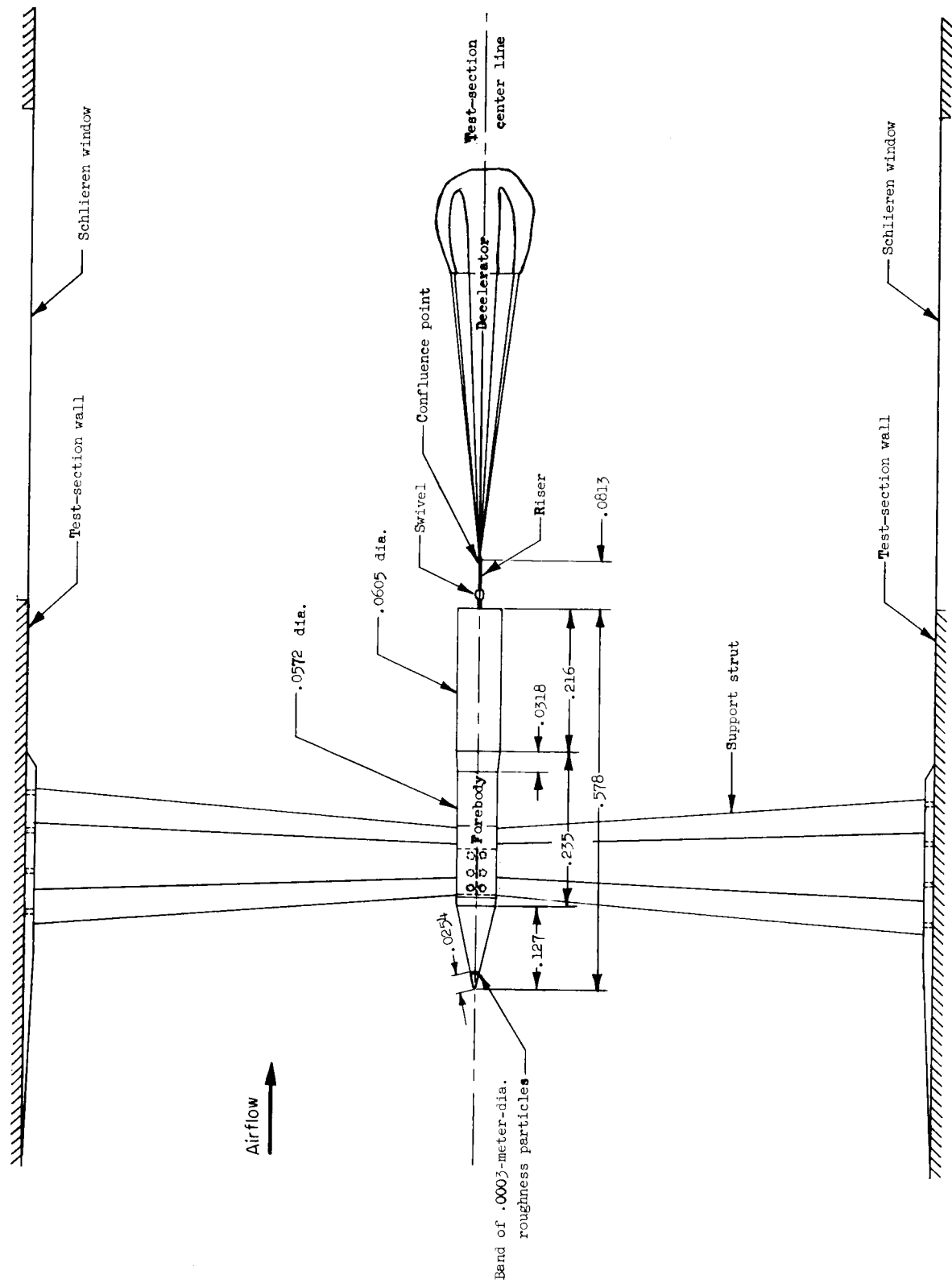
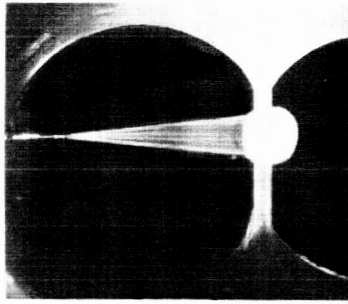
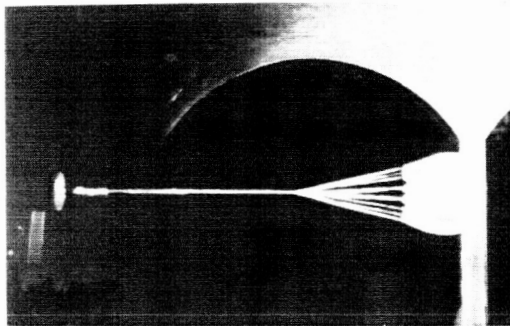


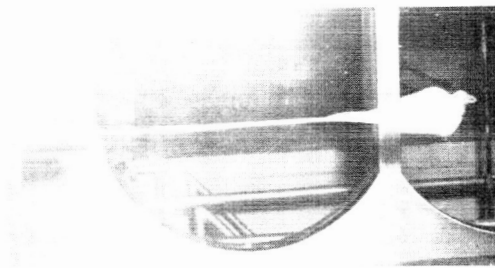
Figure 2.- Installation of forebody, support system, and decelerator in test section. (All dimensions are in meters.)



(a) Suspension lines and canopy spinning.

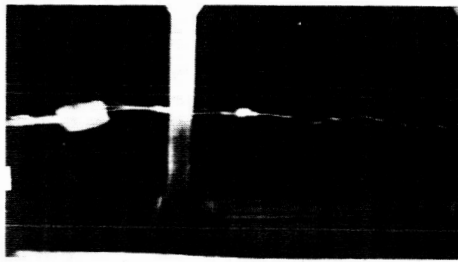


(b) Partially wrapped suspension lines.

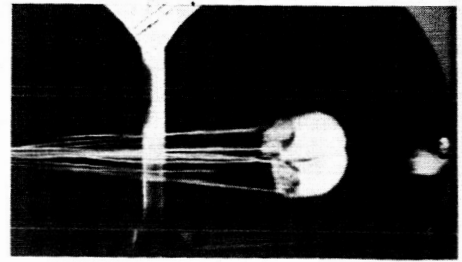


(c) Wrapped suspension lines and collapsed canopy.

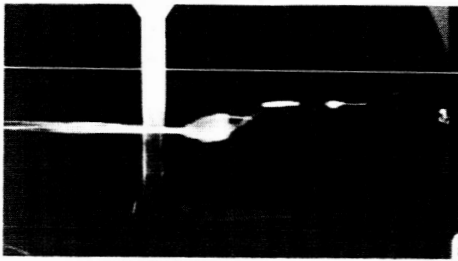
Figure 3.- Behavior of canopy and suspension lines due to binding of swivel. L-75-101



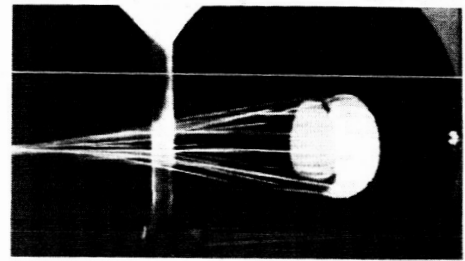
$t = 0 \text{ sec}$



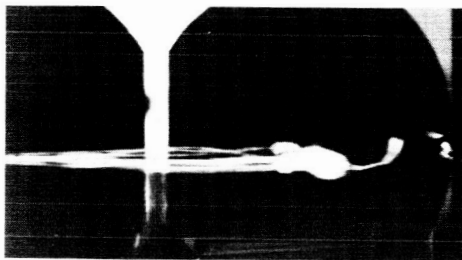
$t = 0.030 \text{ sec}$



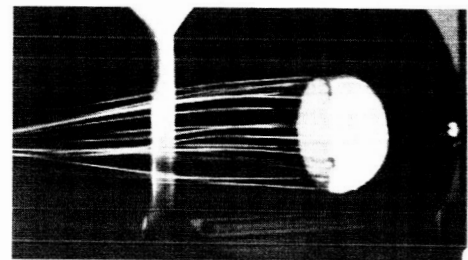
$t = 0.018 \text{ sec}$



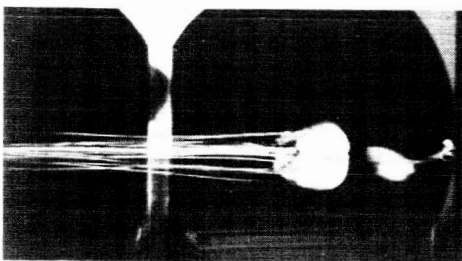
$t = 0.038 \text{ sec}$



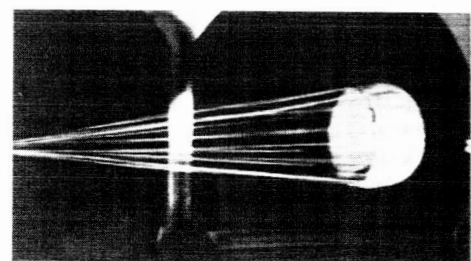
$t = 0.023 \text{ sec}$



$t = 0.043 \text{ sec}$

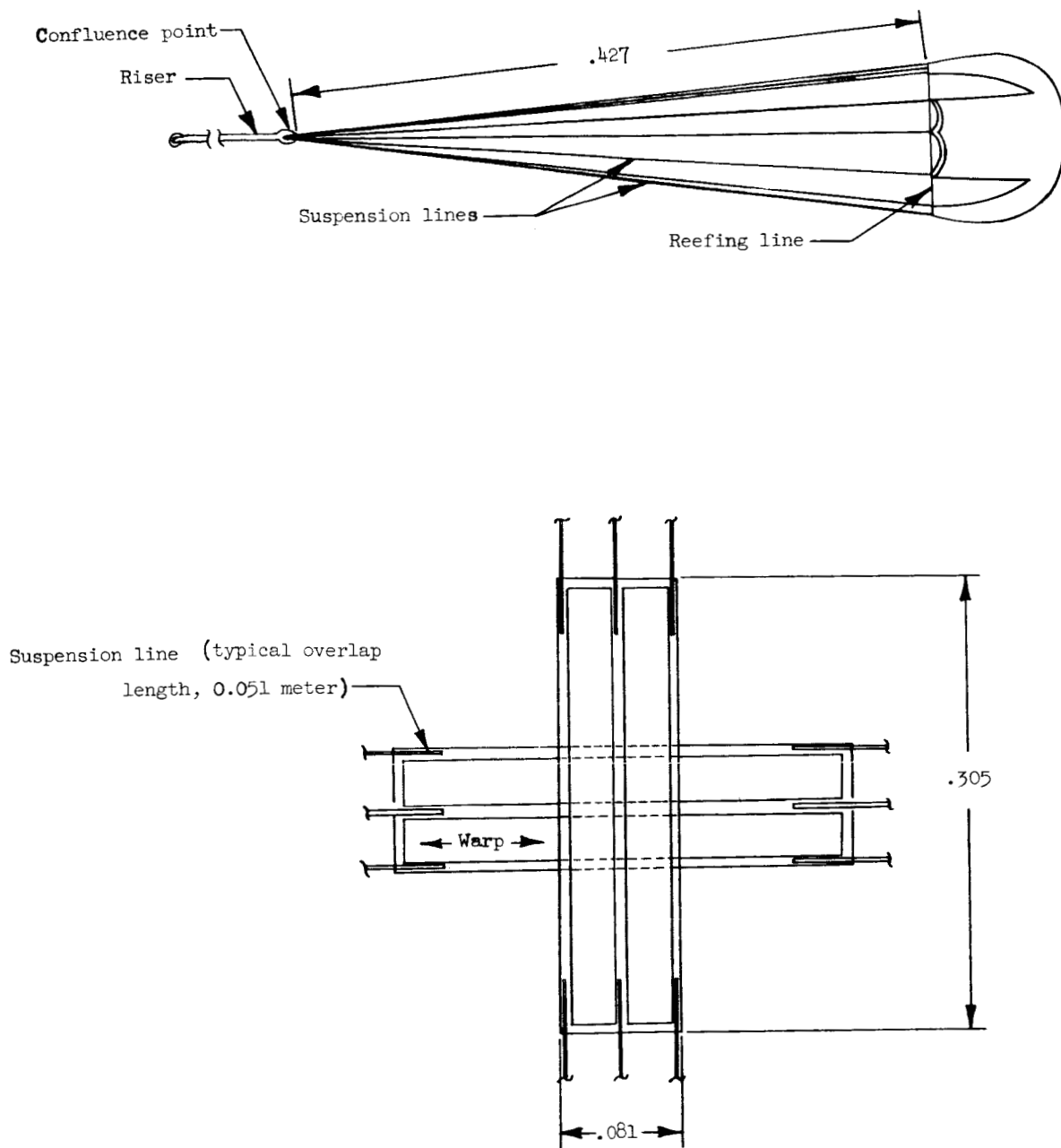


$t = 0.028 \text{ sec}$



Steady state

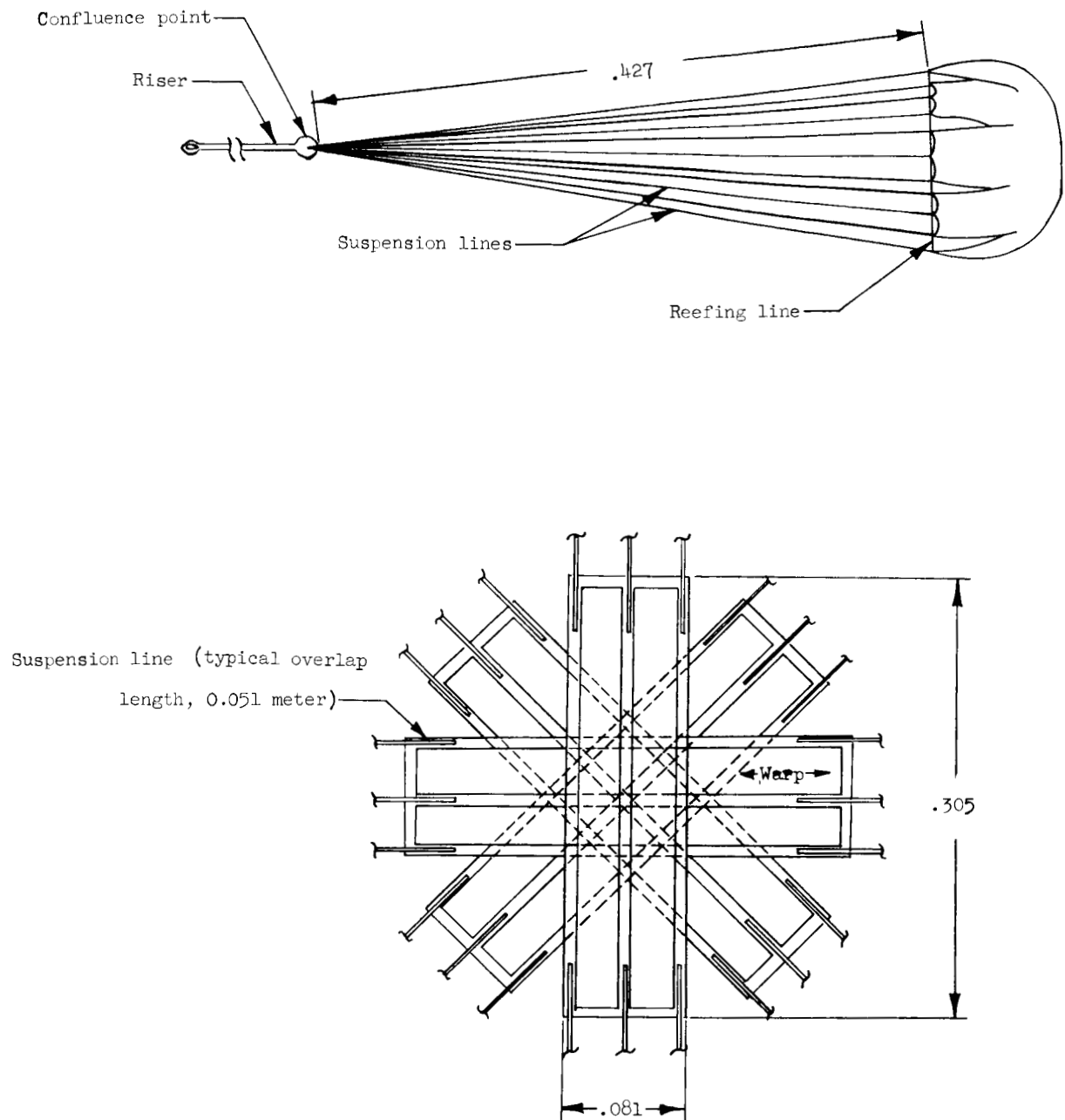
Figure 4.- Deployment sequence of 0.33-meter-nominal-diameter hemisflo parachute. L-75-102



Canopy detail.

(a) Cross canopy.

Figure 5.- Details of decelerator configurations. (All dimensions are in meters.)

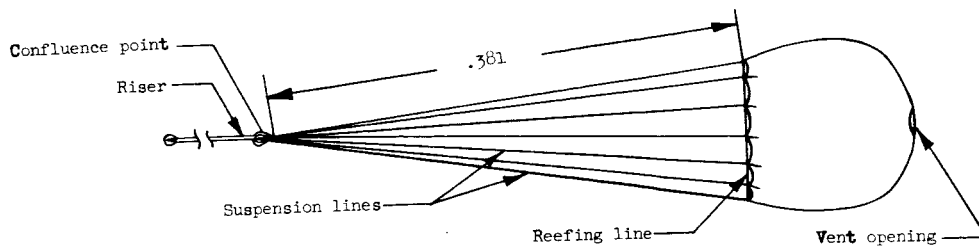


Canopy detail

(b) Modular cross canopy.

Figure 5. - Continued.



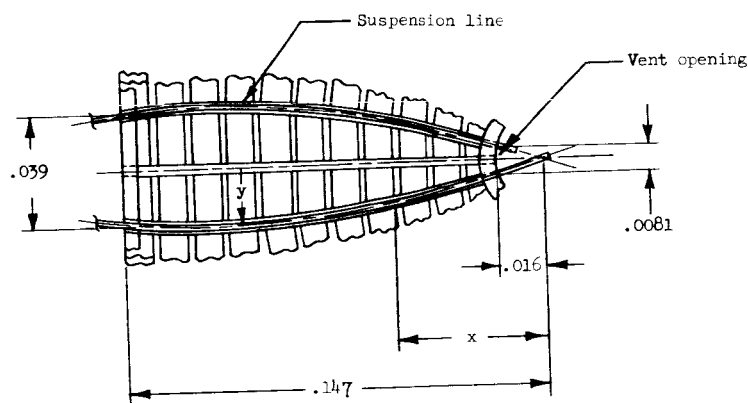


Gore Coordinates  
(0.085 geometric porosity)

x	y
0.0160	0.0041
.0267	.0069
.0377	.0099
.0488	.0127
.0598	.0152
.0709	.0173
.0819	.0188
.0930	.0201
.1040	.0206
.1150	.0203
.1260	.0198
.1370	.0196
.1470	.0196

Gore Coordinates  
(0.147 geometric porosity)

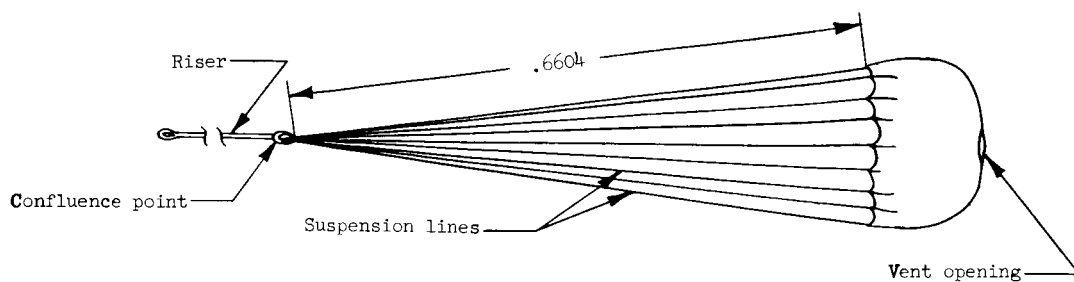
x	y
0.0160	0.0041
.0267	.0069
.0389	.0099
.0511	.0127
.0632	.0152
.0754	.0173
.0876	.0188
.0998	.0201
.1120	.0206
.1242	.0203
.1364	.0198
.1473	.0196



Canopy gore ( 12 required )

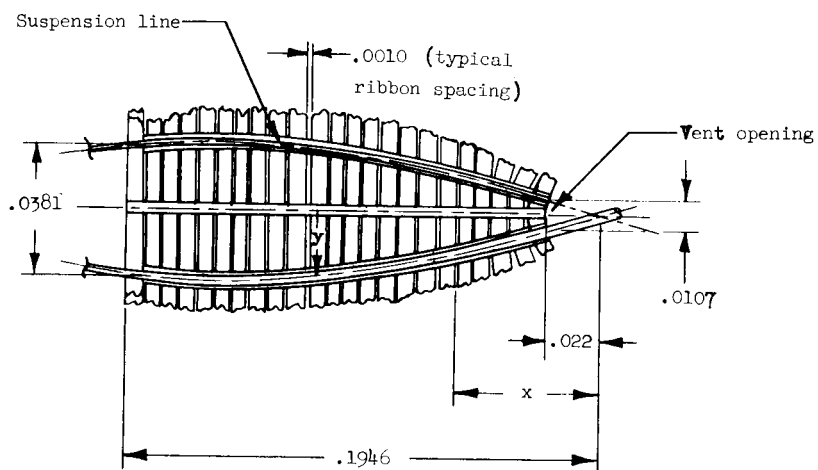
(c) Hemisflo canopy, 0.254-meter diameter.

Figure 5.- Continued.



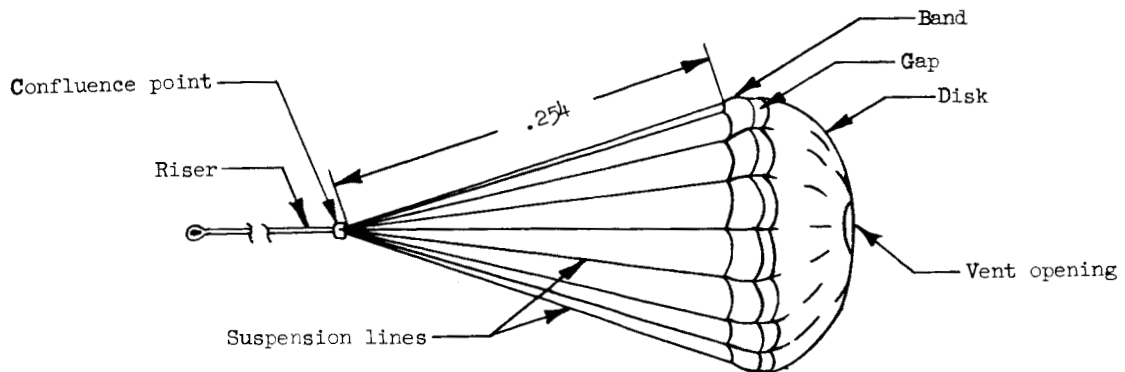
Gore Coordinates  
(0.147 geometric porosity)

x	y
0.0221	0.0053
.0353	.0066
.0513	.0097
.0676	.0124
.0836	.0147
.0996	.0168
.1158	.0183
.1285	.0196
.1481	.0201
.1641	.0198
.1803	.0193
.1946	.0191



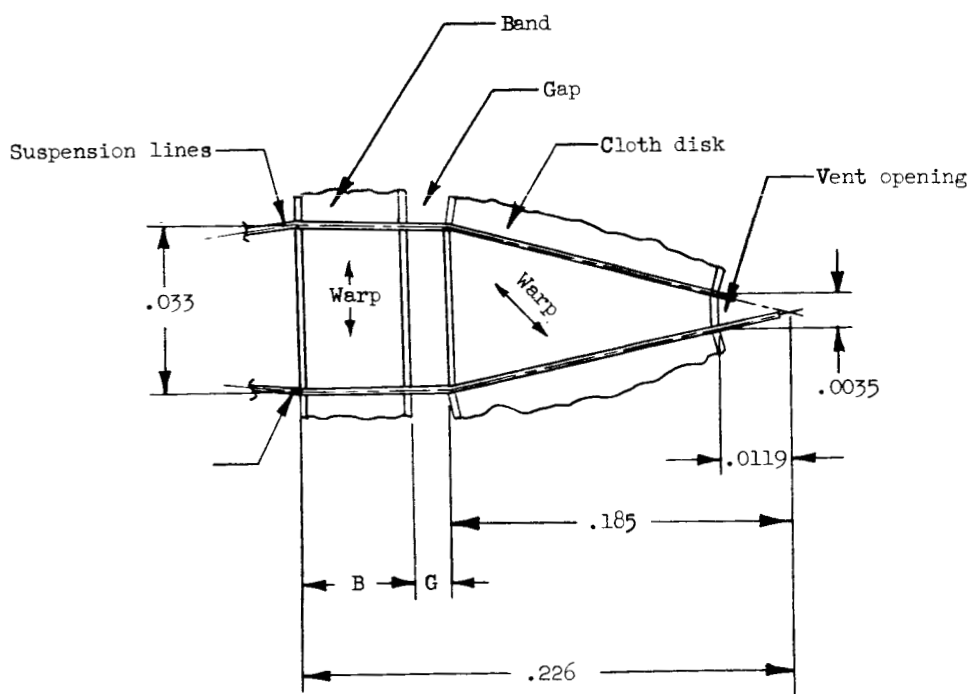
Canopy gore ( 16 required )  
(d) Hemisflo canopy, 0.33-meter diameter.

Figure 5.- Continued.



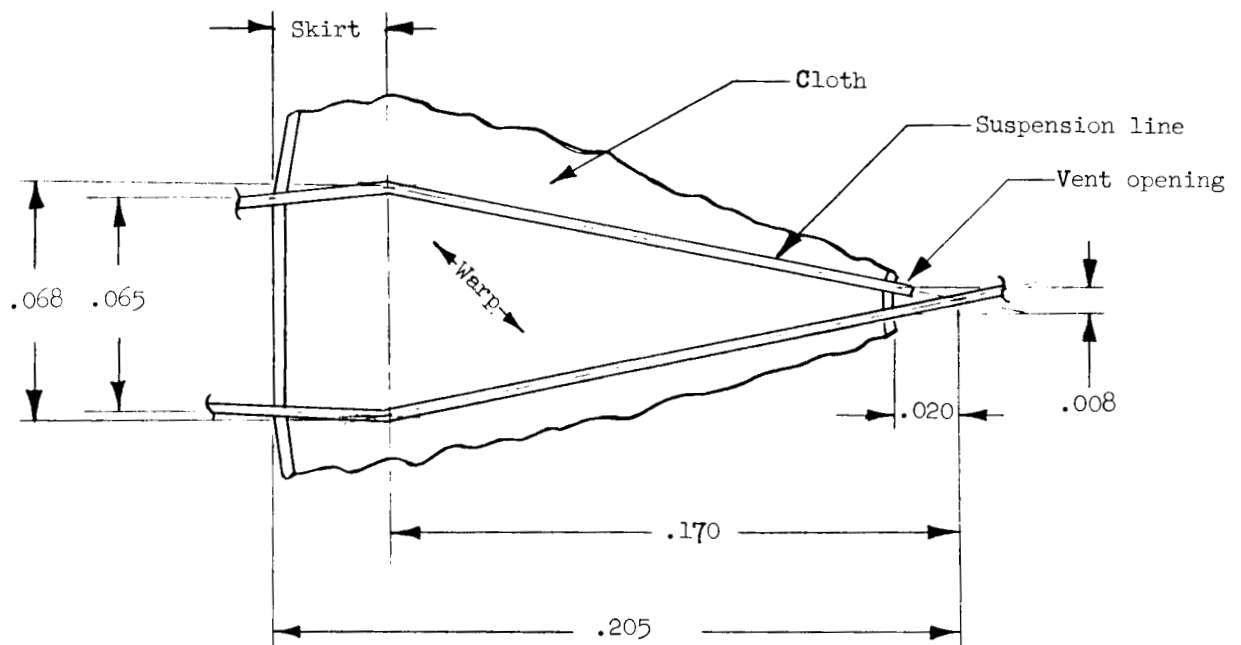
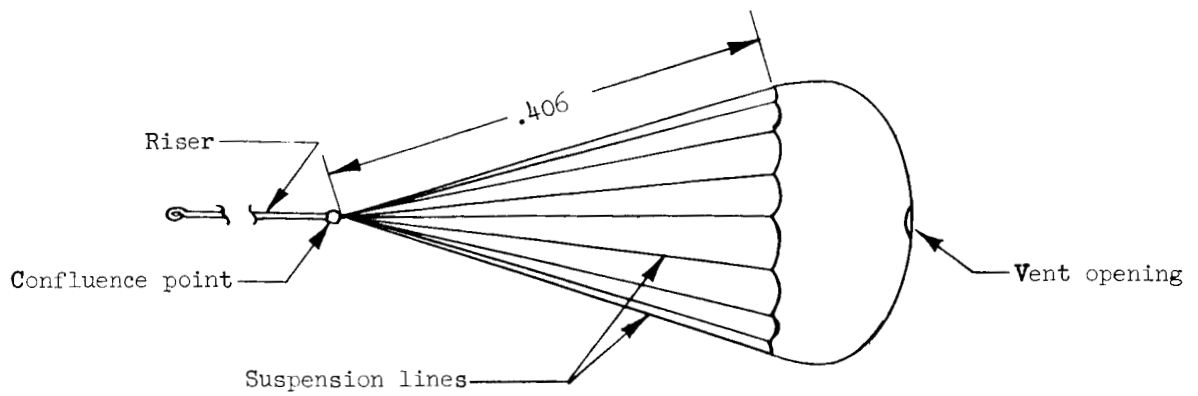
Gap and Band Dimensions

Porosity	0.060	0.125	0.200
G	0.0048	0.0104	0.0170
B	.0361	.0305	.0239



Canopy gore ( 18 required )  
(e) Disk-gap-band canopy.

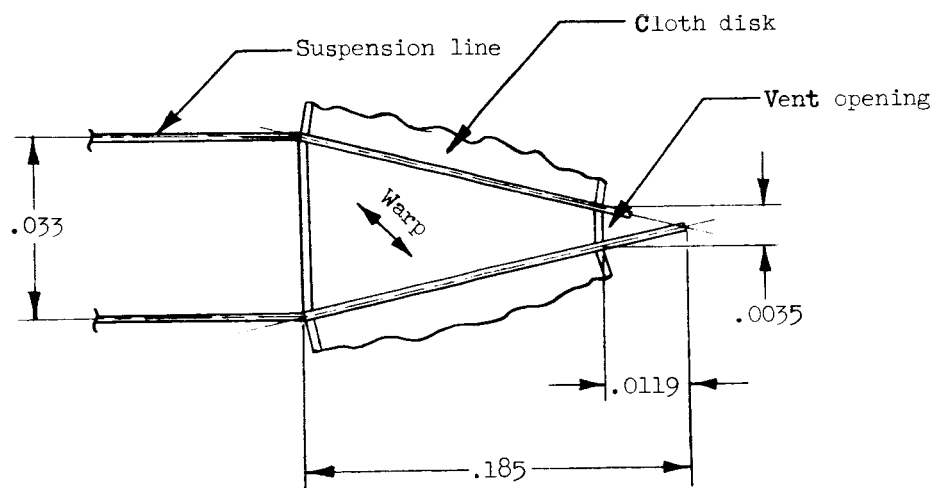
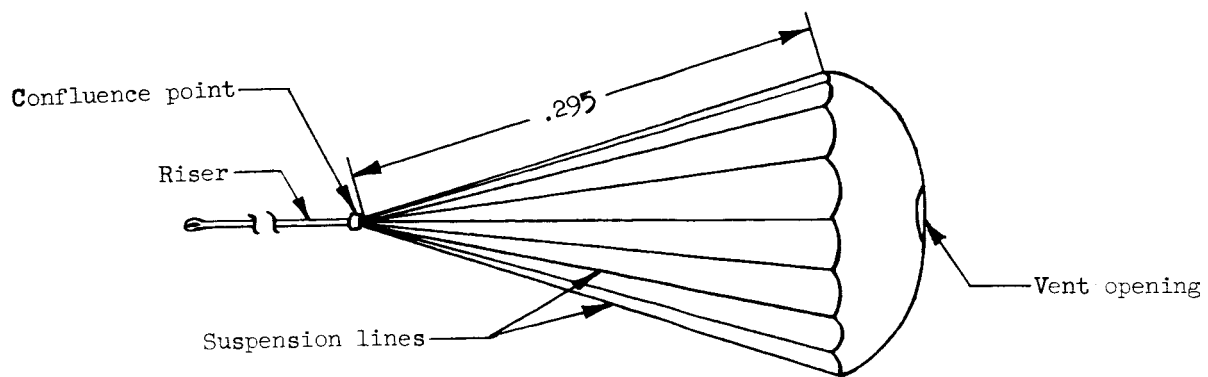
Figure 5.- Continued.



Canopy gore ( 16 required )

(f) Extended-skirt canopy.

Figure 5.- Continued.



Canopy gore ( 16 required )

(g) Standard flat canopy.

Figure 5.- Continued.

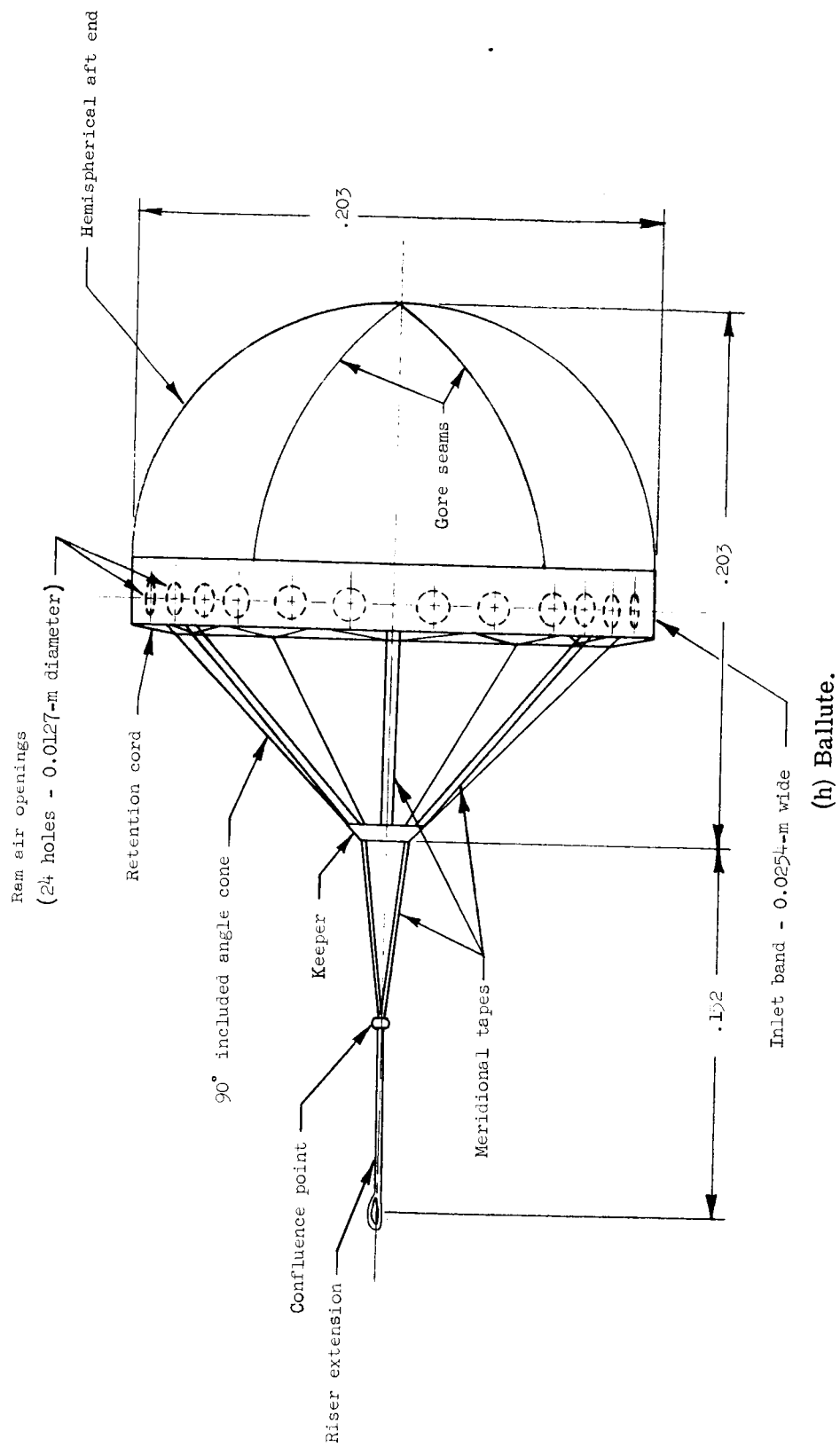
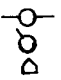
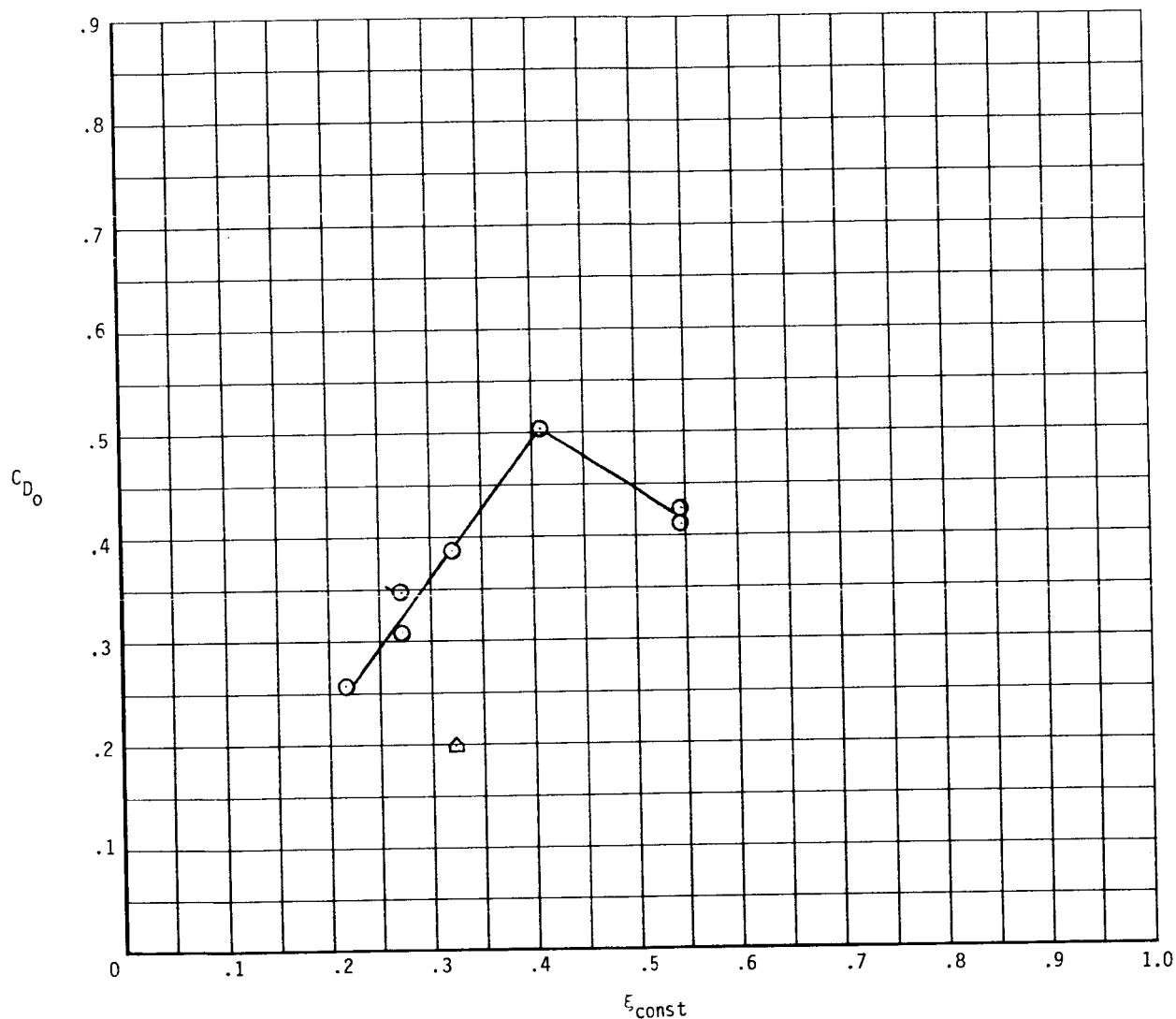


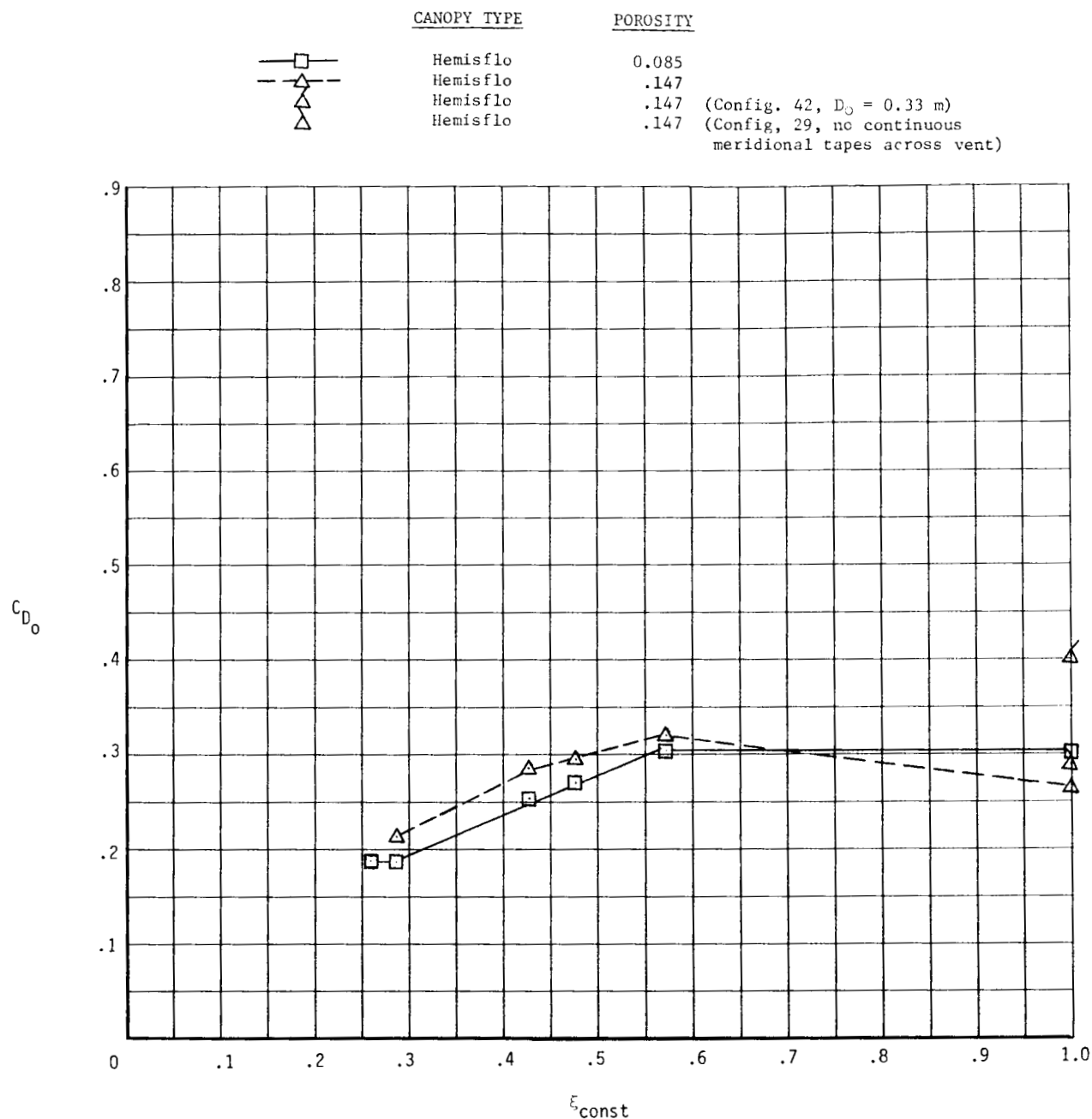
Figure 5.- Concluded.

	CANOPY TYPE	POROSITY
	Cross	0.413
	Cross	.413 (Config. 23, 1 D <sub>0</sub> suspension line length)
	Modular cross	.086



(a) Cross parachutes.

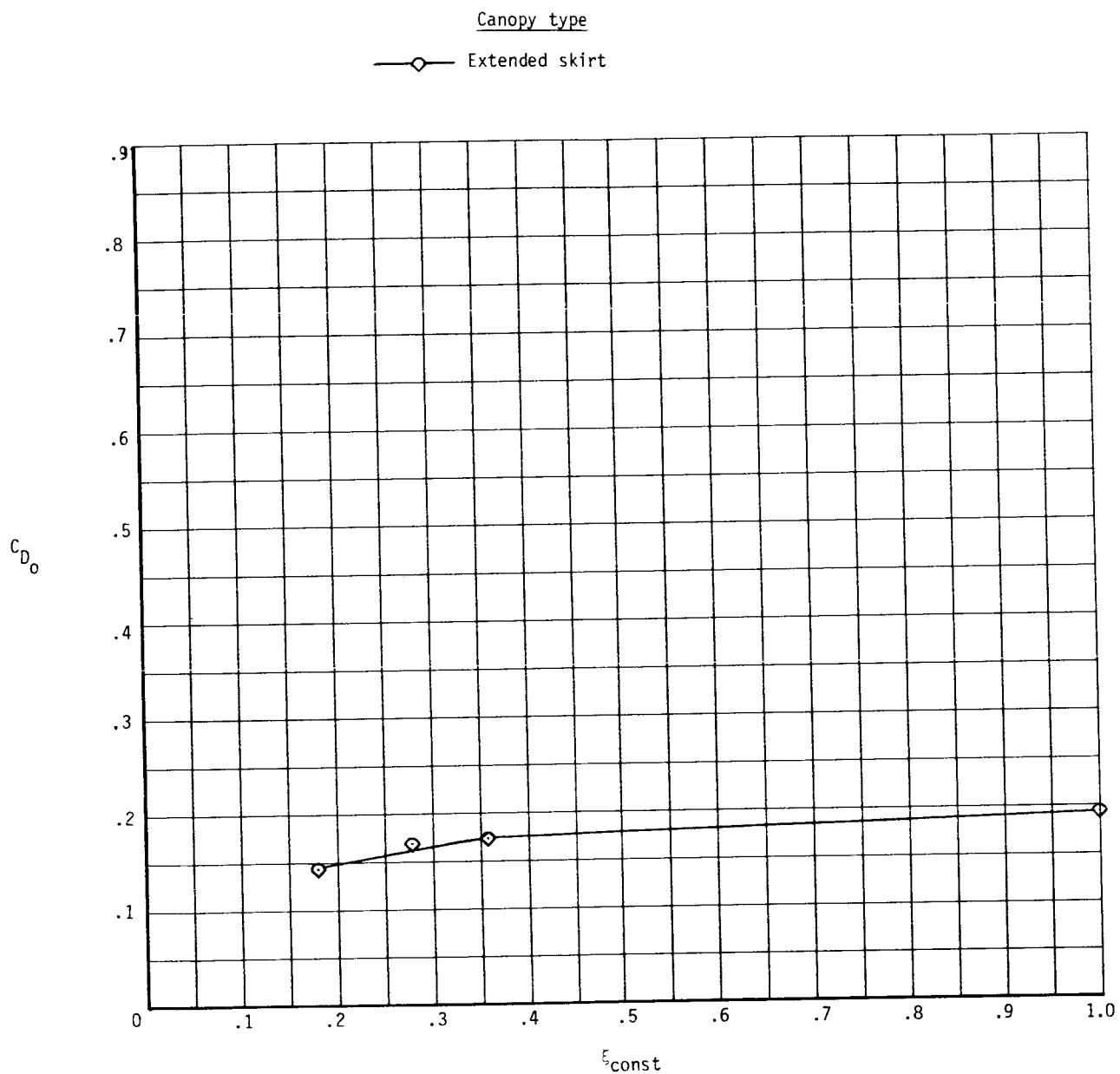
Figure 6.- Variation of drag coefficient with constructed reefing ratio for the various types of parachutes at  $M = 1.80$ .



(b) Hemisflo parachutes.

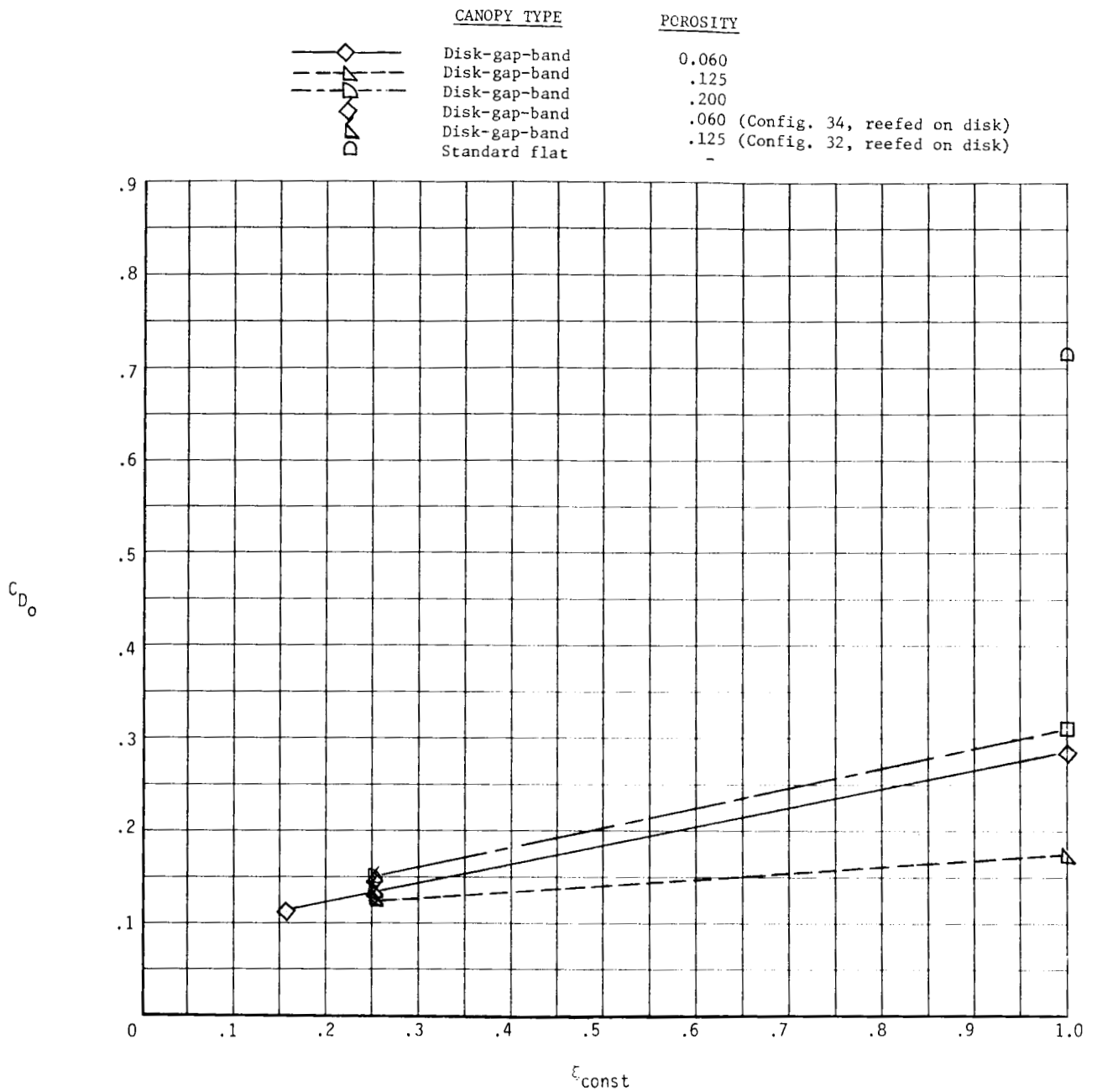
Figure 6.- Continued.





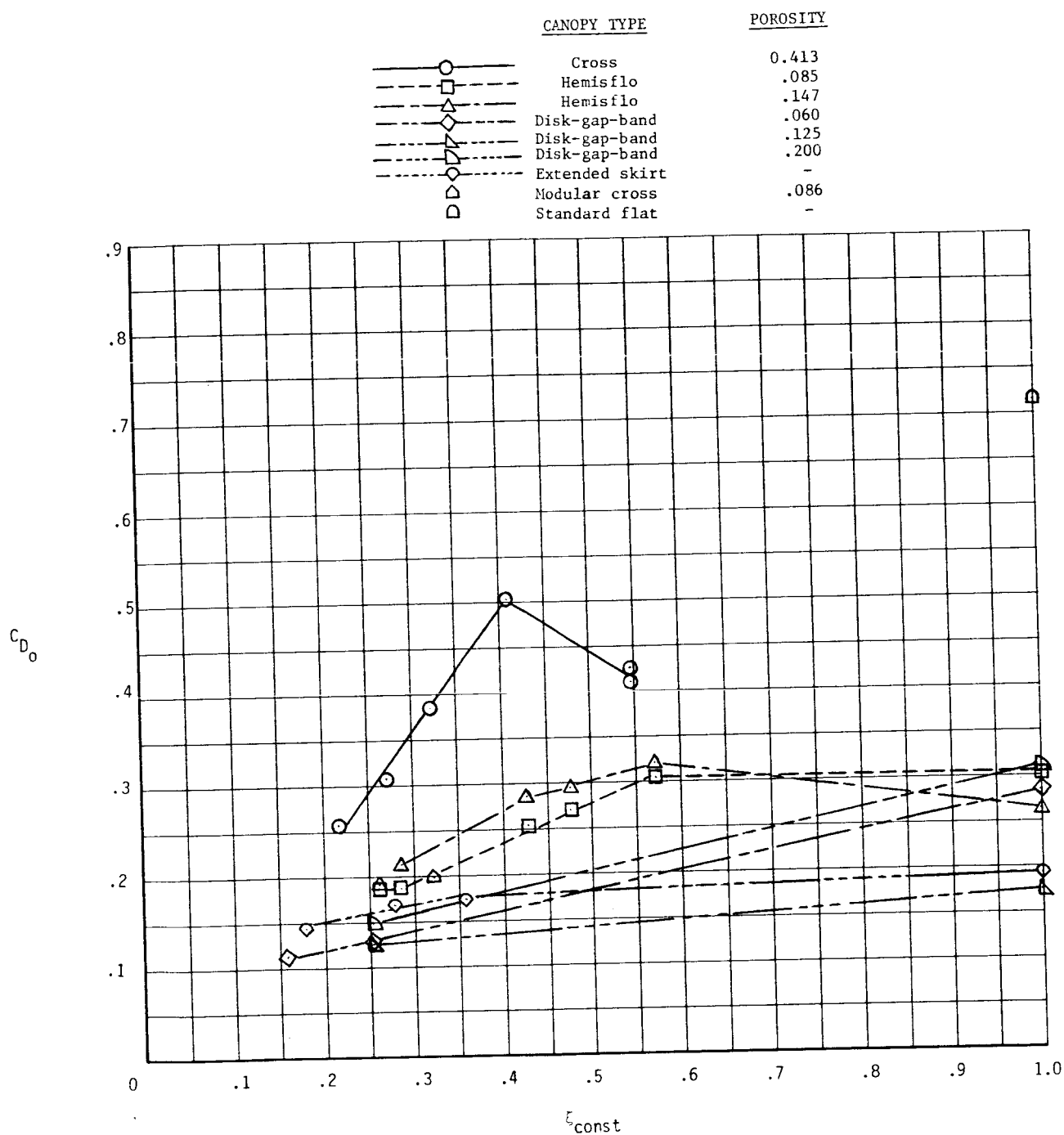
(c) Extended-skirt parachutes.

Figure 6.- Continued.



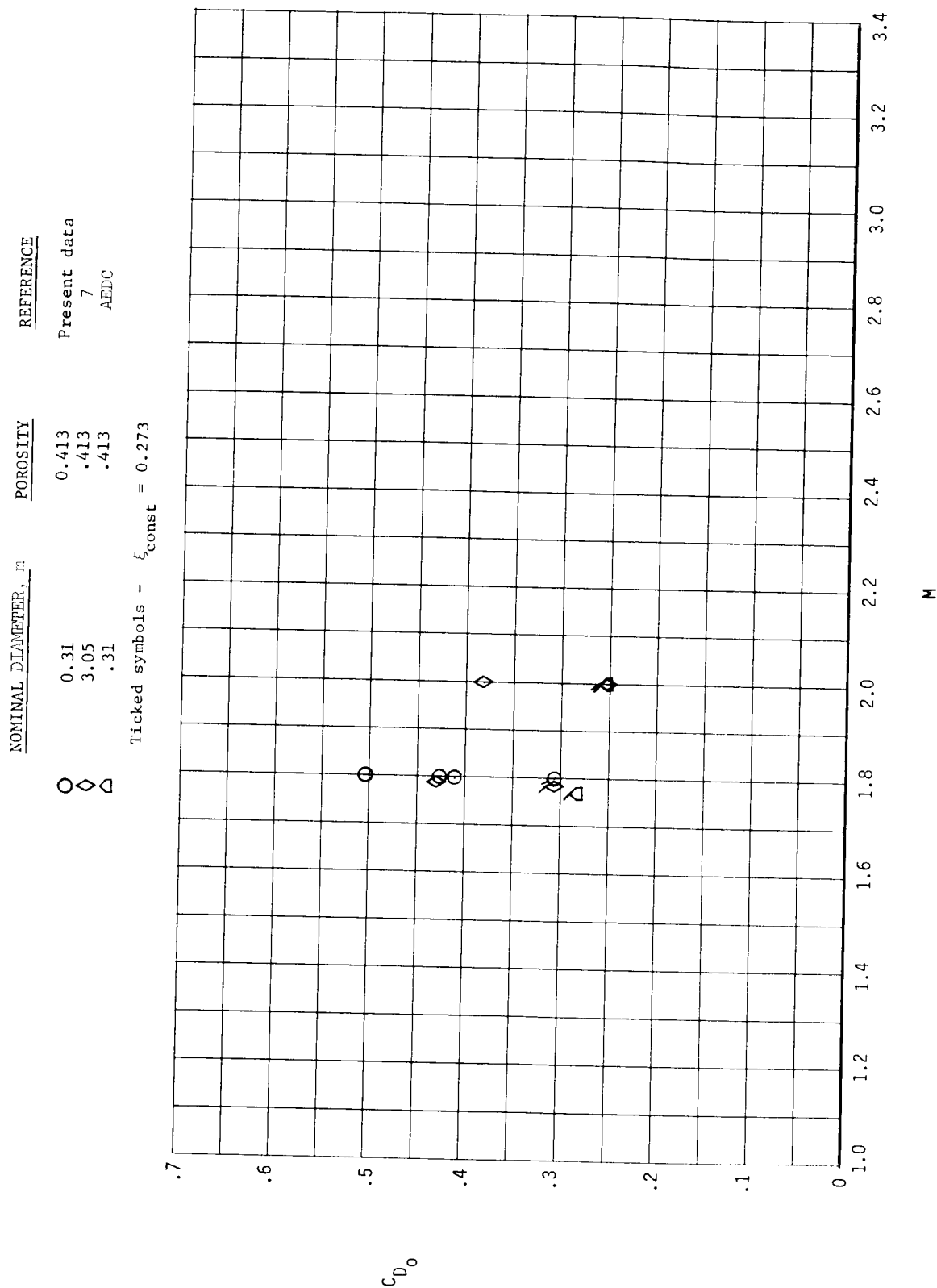
(d) Disk-gap-band parachutes.

Figure 6.- Continued.



(e) Summary.

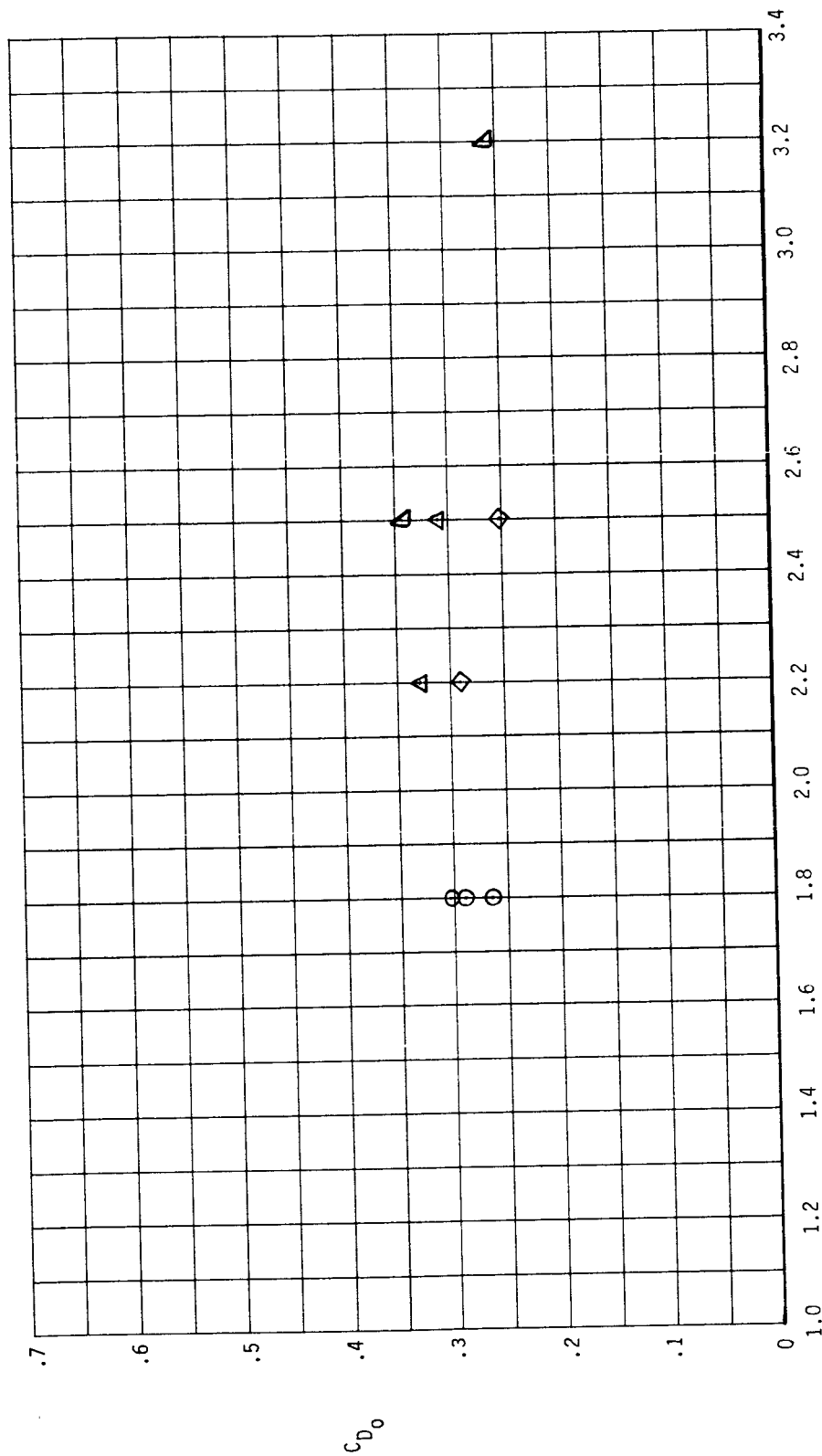
Figure 6.- Concluded.



(a) Cross canopies.

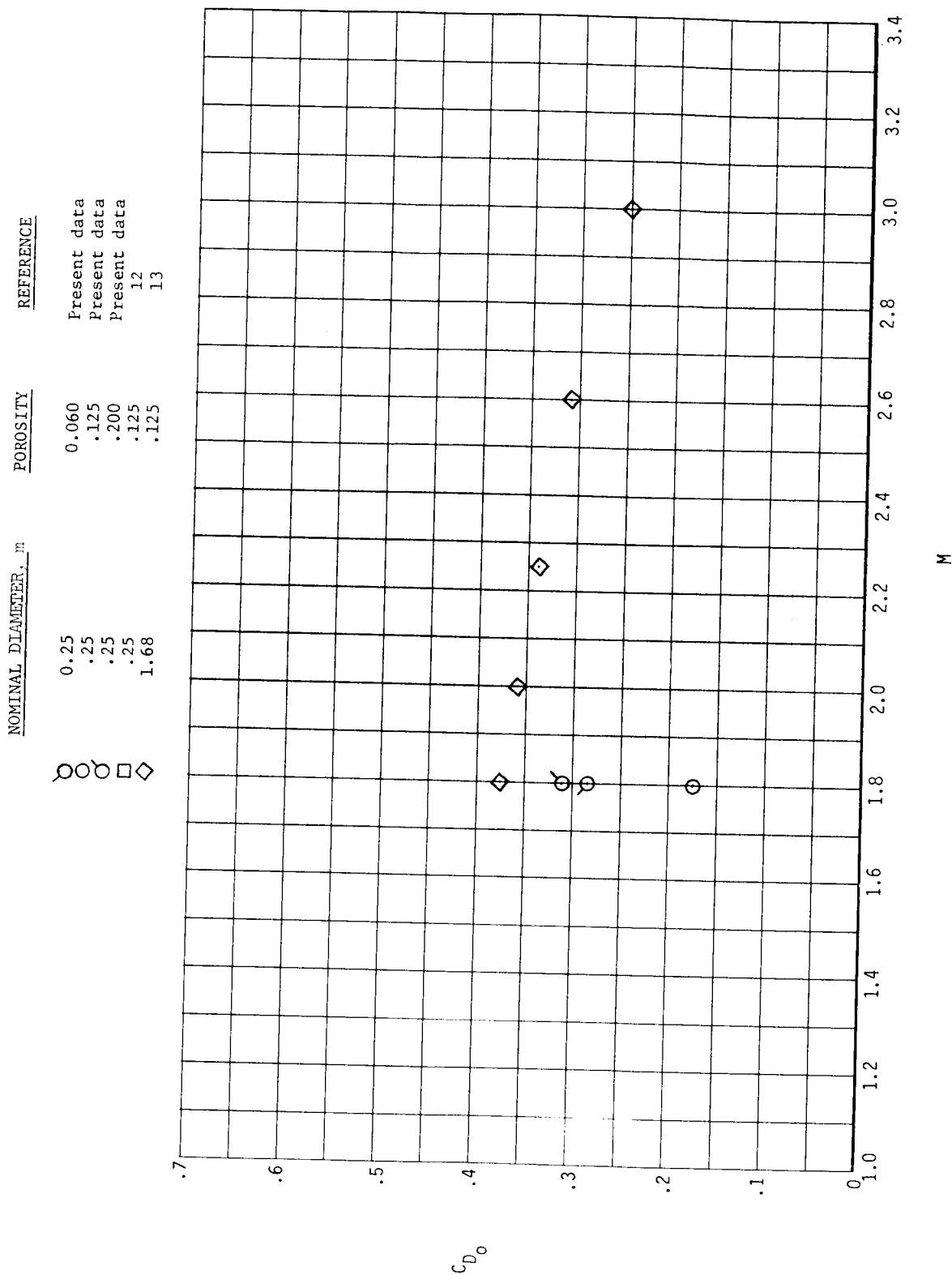
Figure 7.- Comparison of drag coefficients obtained for various types of parachutes with other wind-tunnel data.

	NOMINAL DIAMETER, m	POROSITY	REFERENCE
○	0.25	0.147	Present data
◇	1.83	.210	9
△	.46	.210	9
▽	.33	.143	10



(b) Hemisflo parachutes (no reefing).

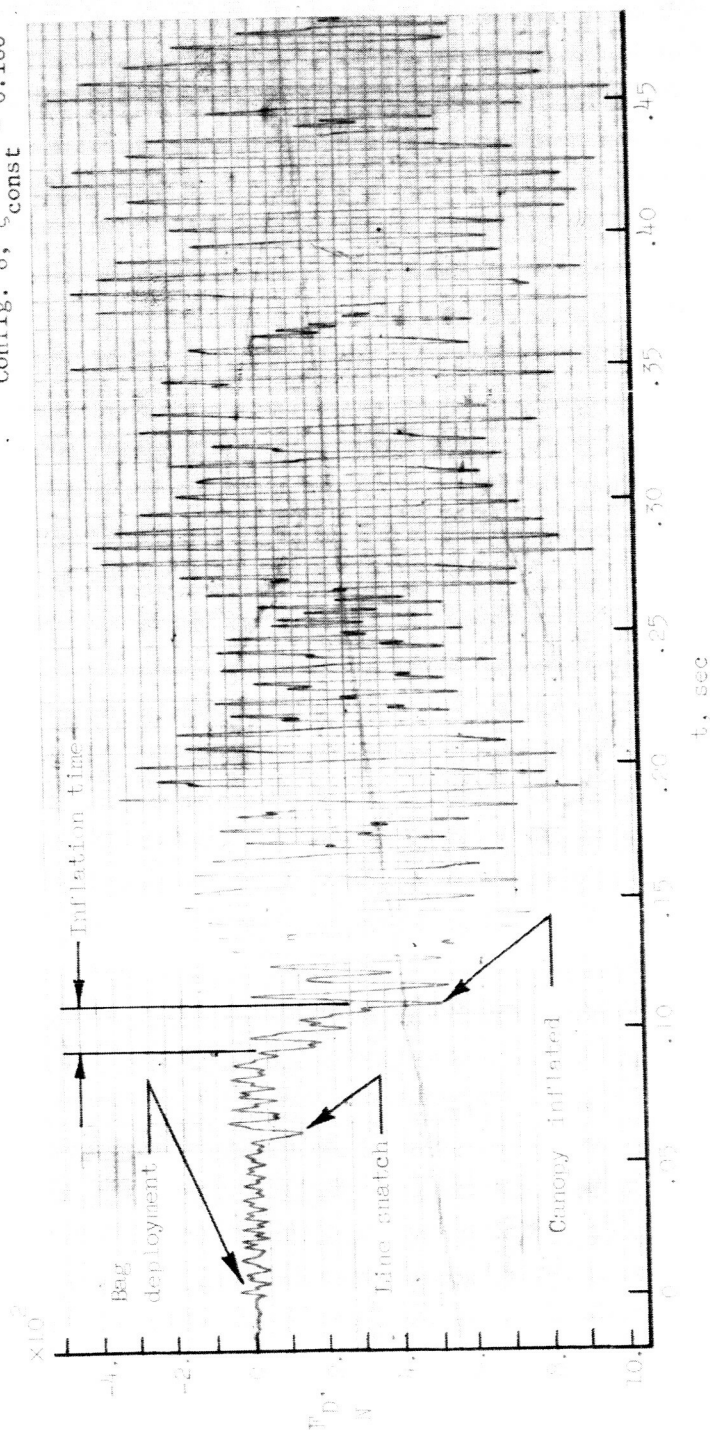
Figure 7. - Continued.



(c) Disk-gap-band parachutes (no reefing).

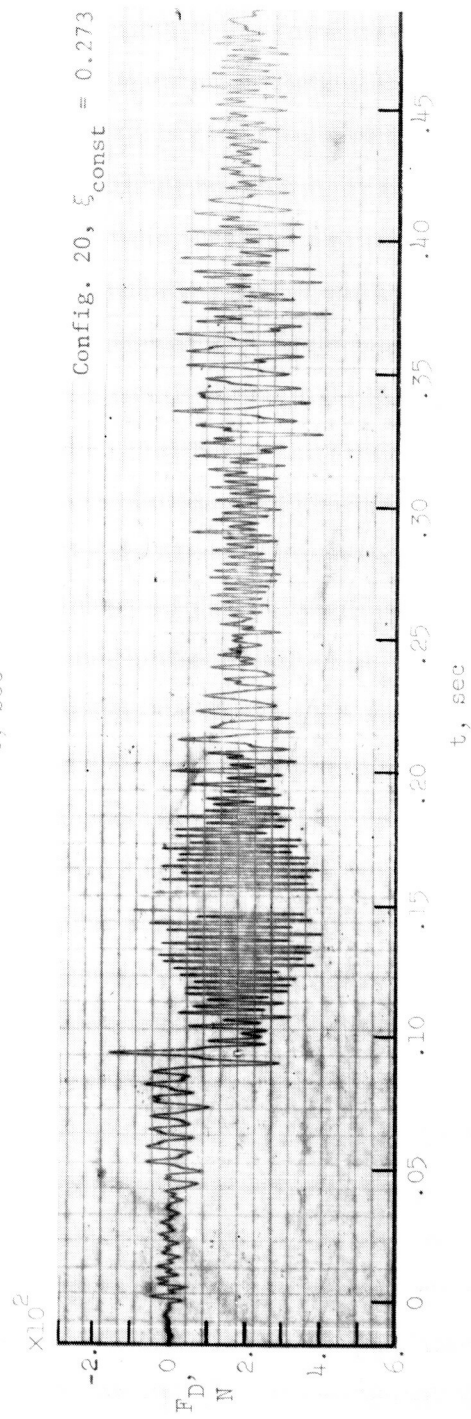
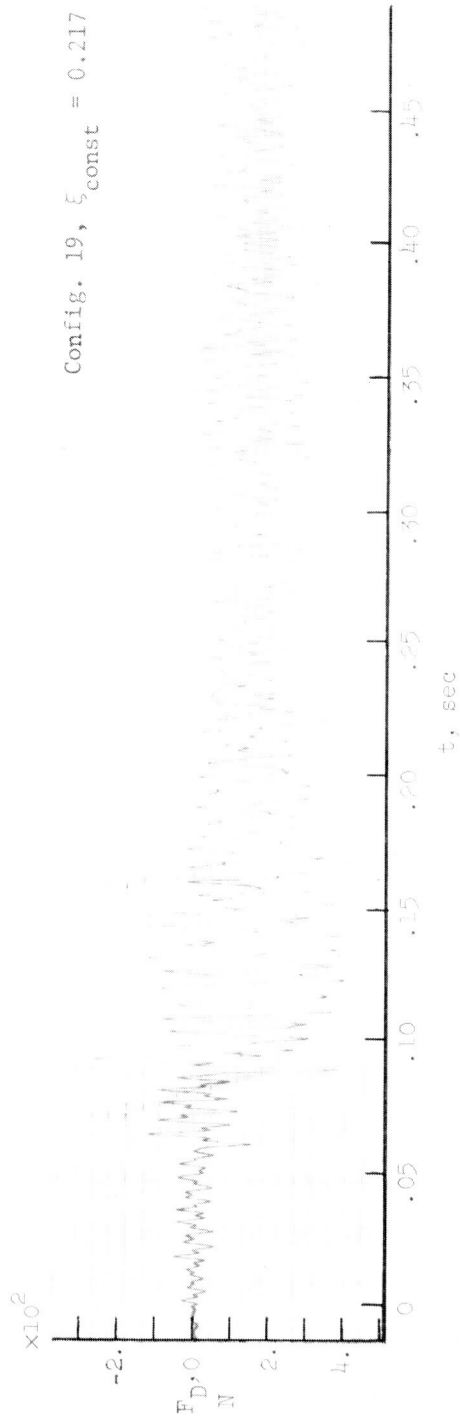
Figure 7. - Concluded.

Config. 8,  $\xi_{\text{const}} = 0.180$



(a) Typical analysis of trace; extended-skirt canopy.

Figure 8.- Oscillograph records of drag for configurations tested.

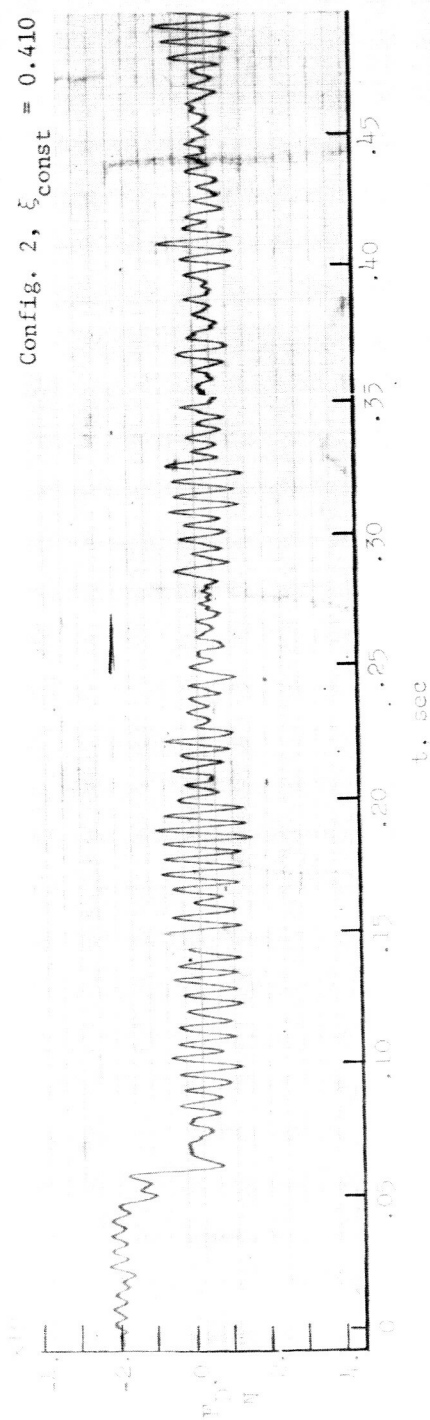


(b) Cross canopies.

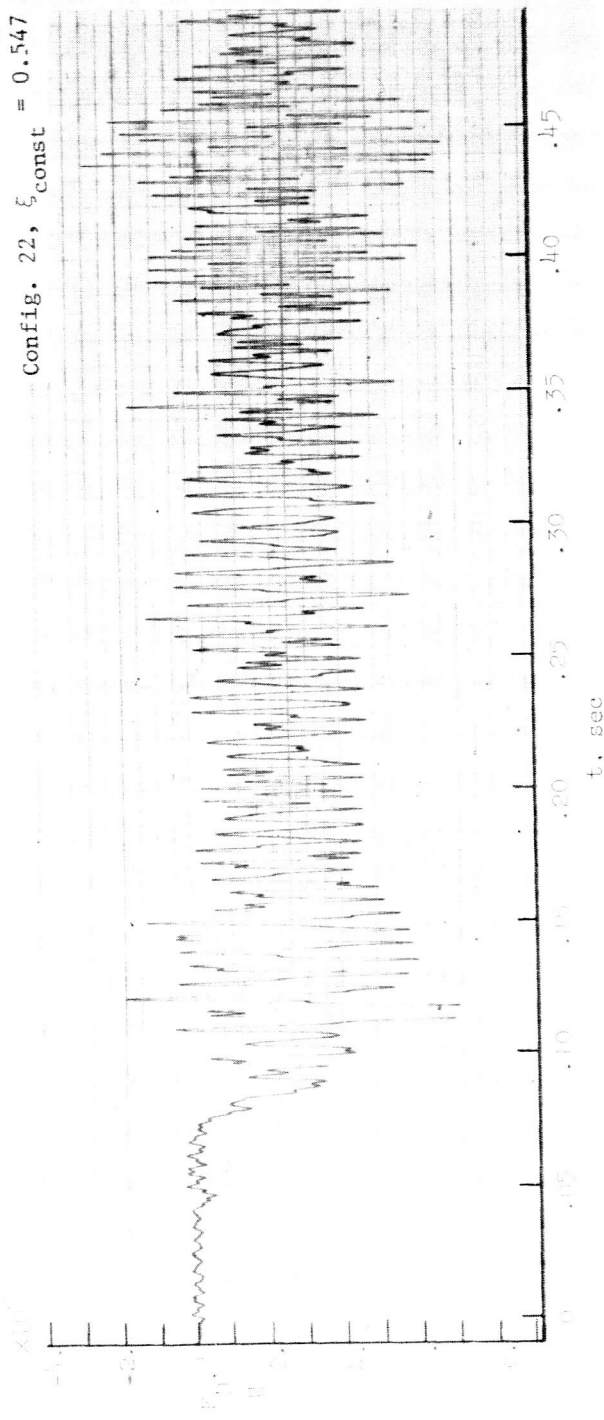
Figure 8.- Continued.



Config. 2,  $\xi_{\text{const}} = 0.410$

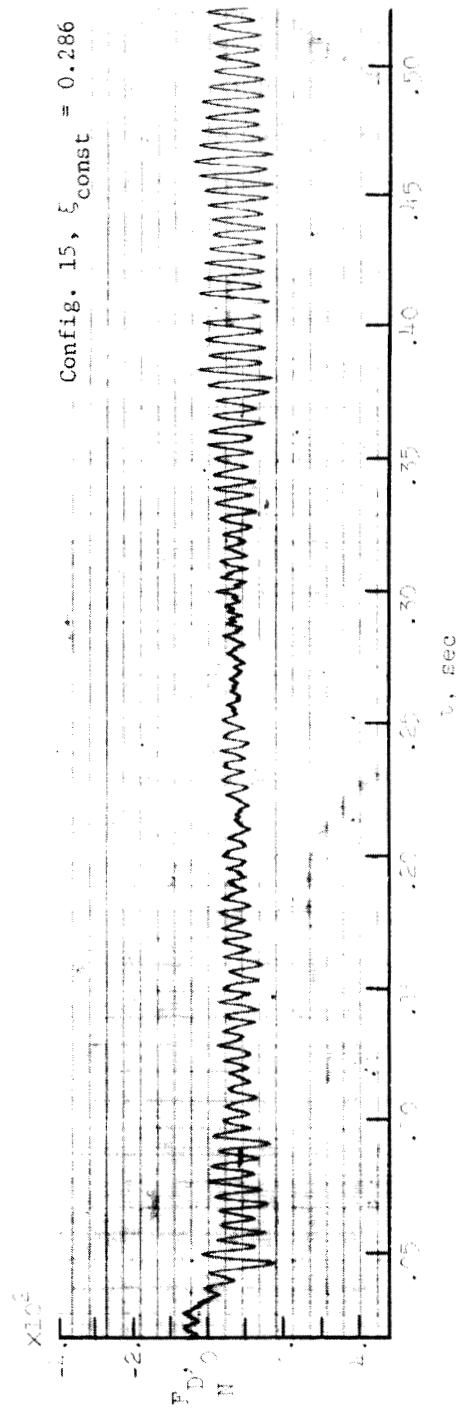
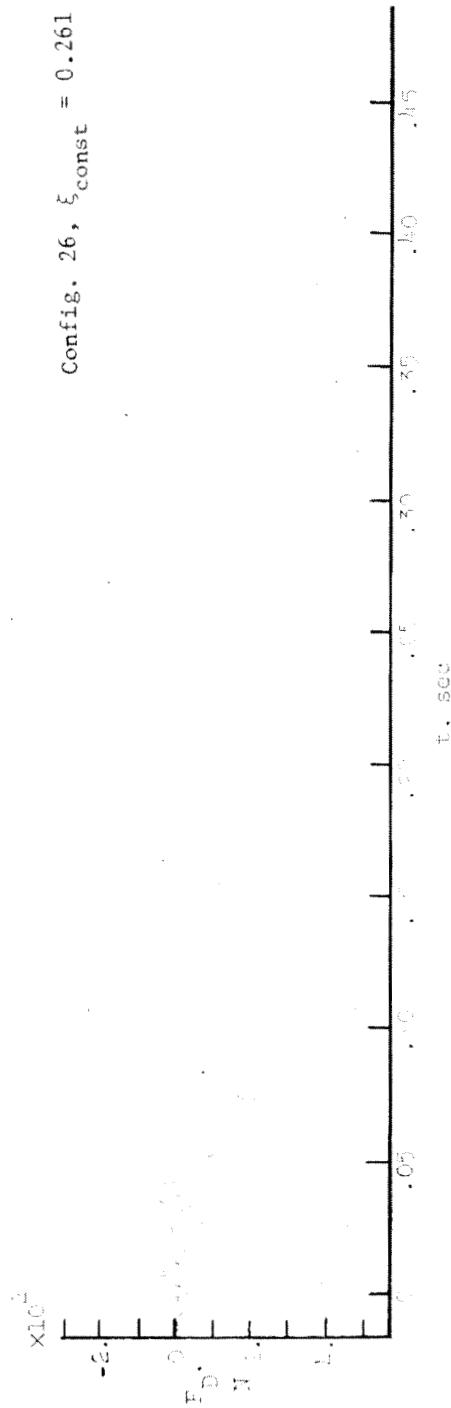


Config. 22,  $\xi_{\text{const}} = 0.547$



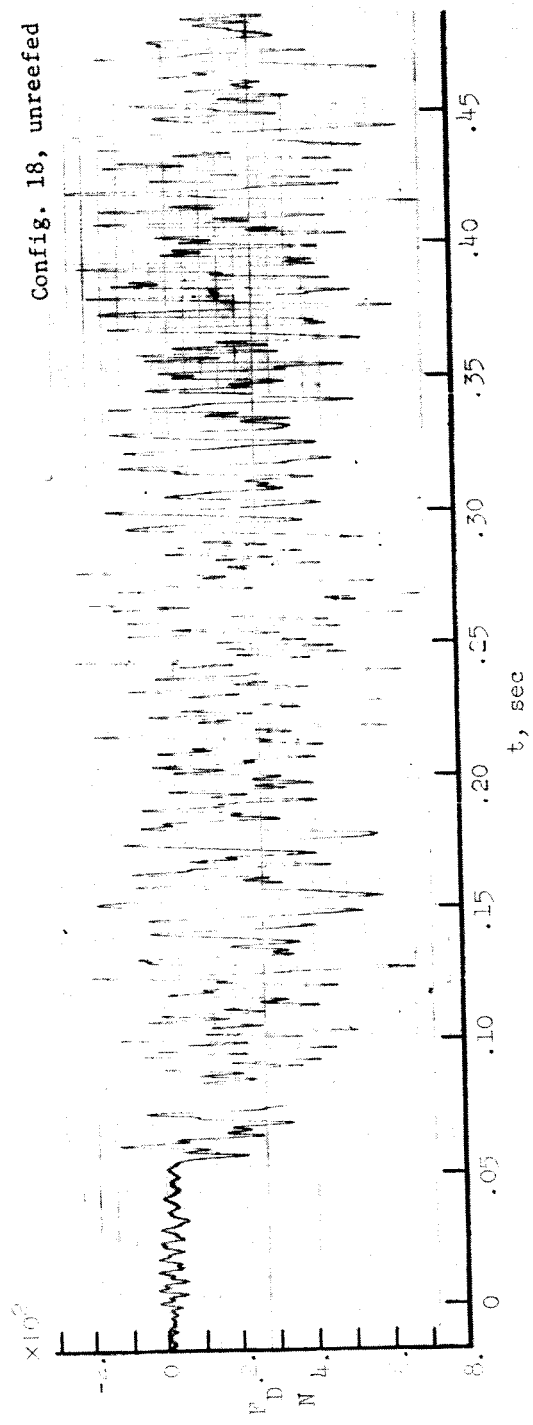
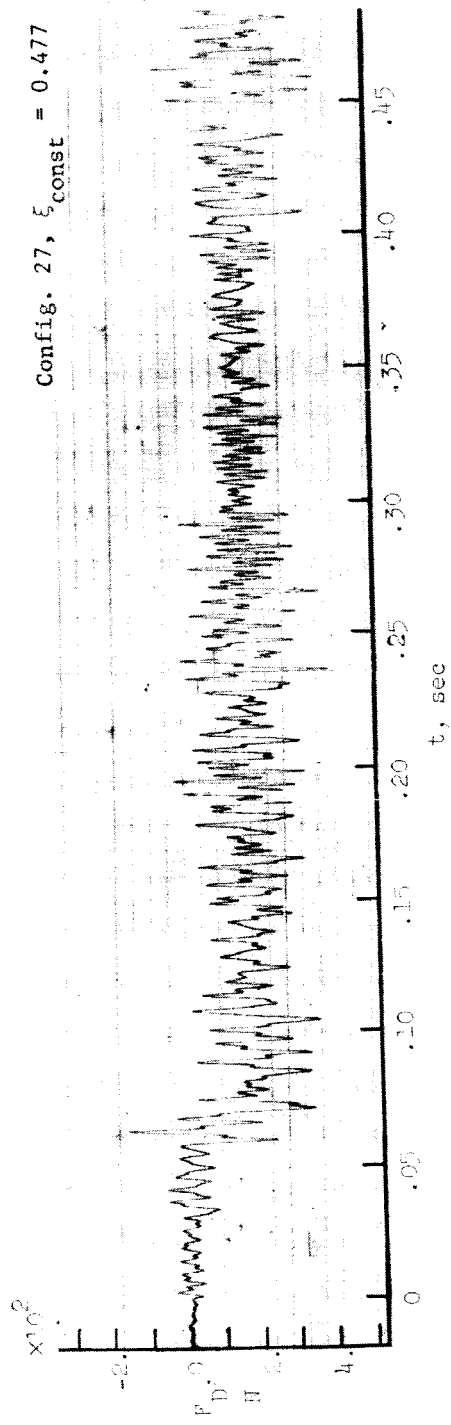
(b) Cross canopies - Concluded.

Figure 8. - Continued.



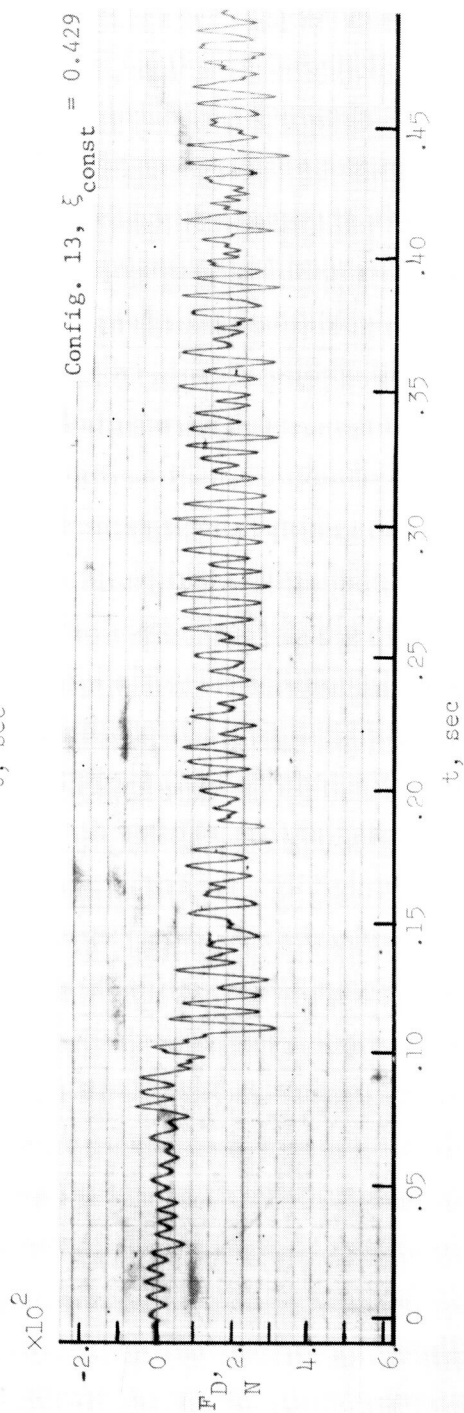
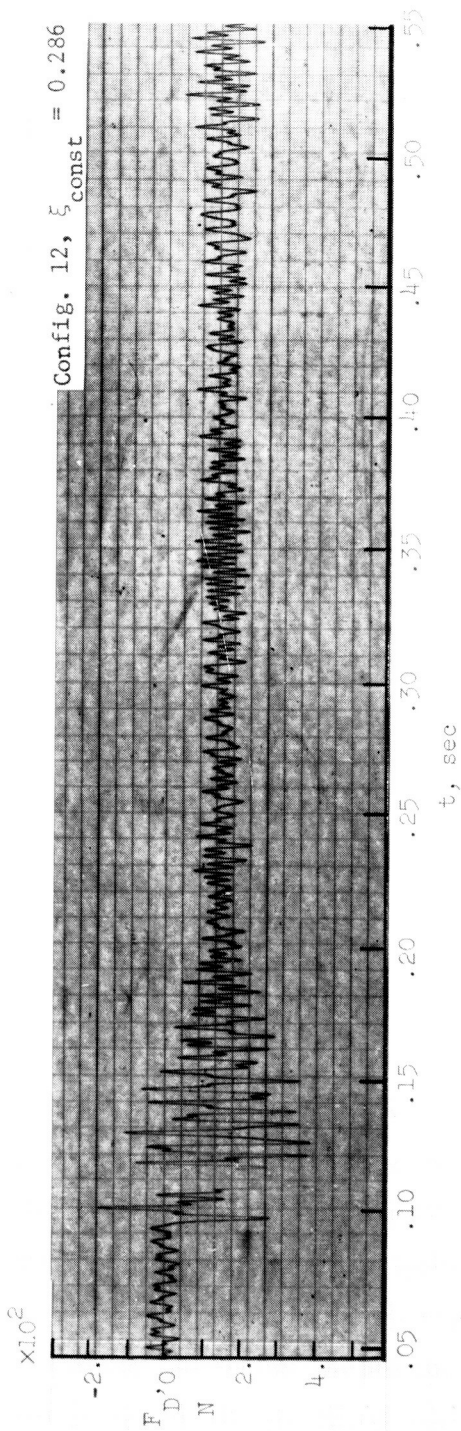
(c) Hemisflo canopies.

Figure 8. - Continued.



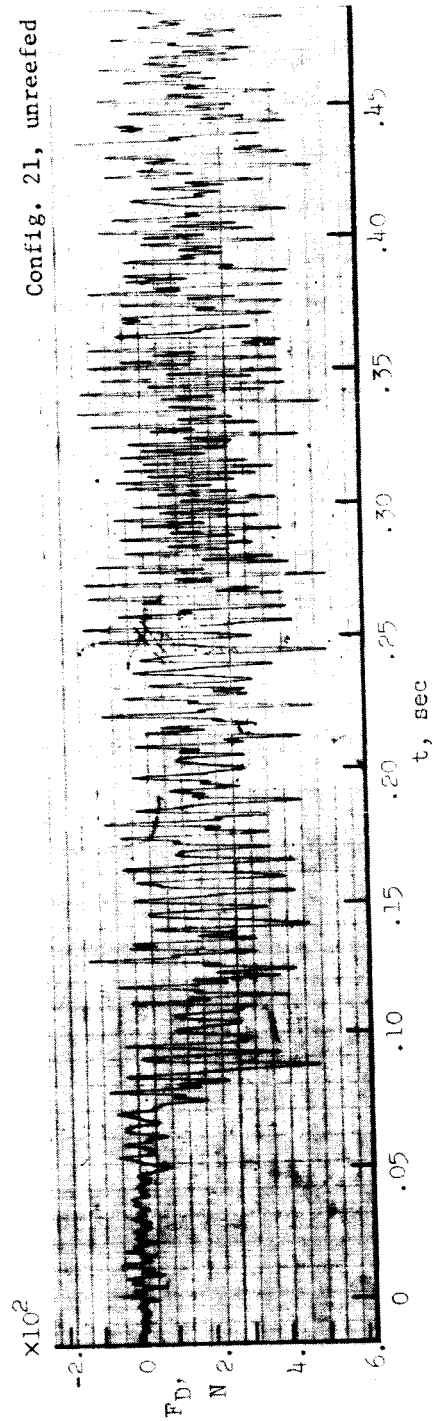
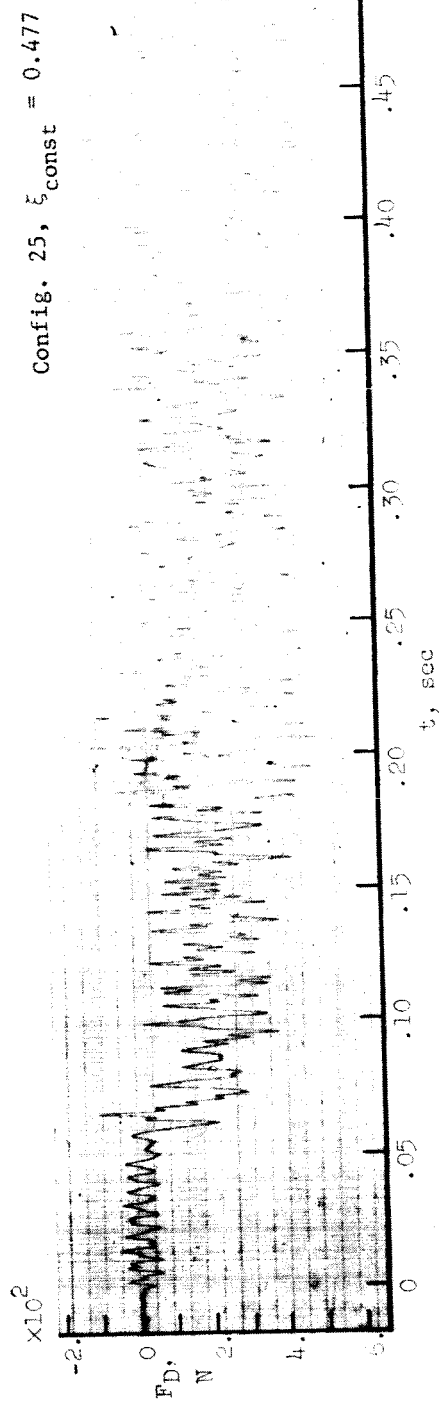
(c) Hemisflo canopies - Continued.

Figure 8. - Continued.



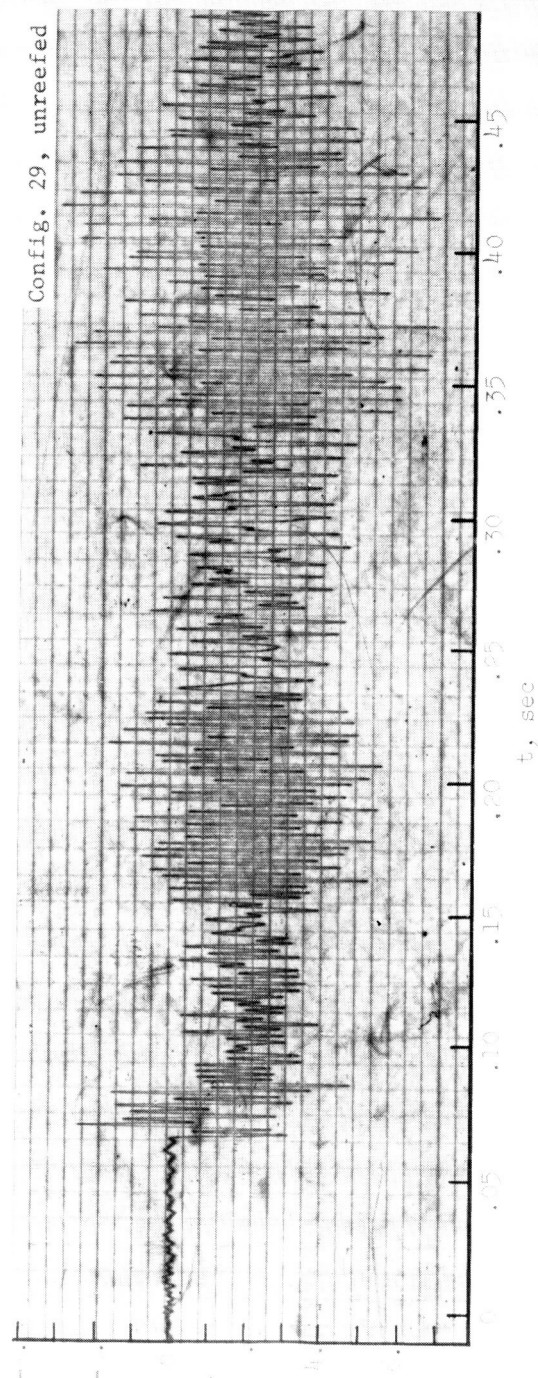
(c) Hemisflo canopies - Continued.

Figure 8. - Continued.



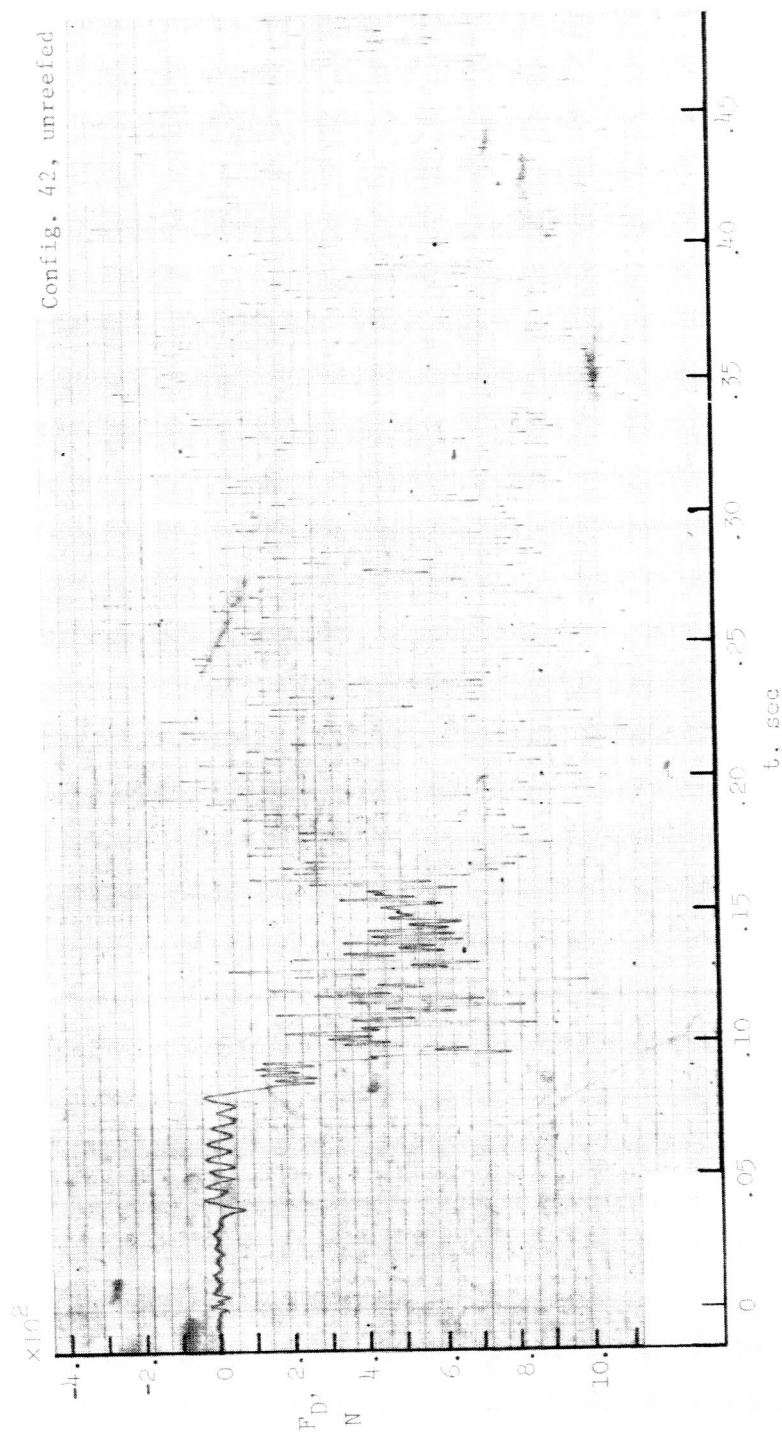
(c) Hemisflo canopies - Continued.

Figure 8.- Continued.



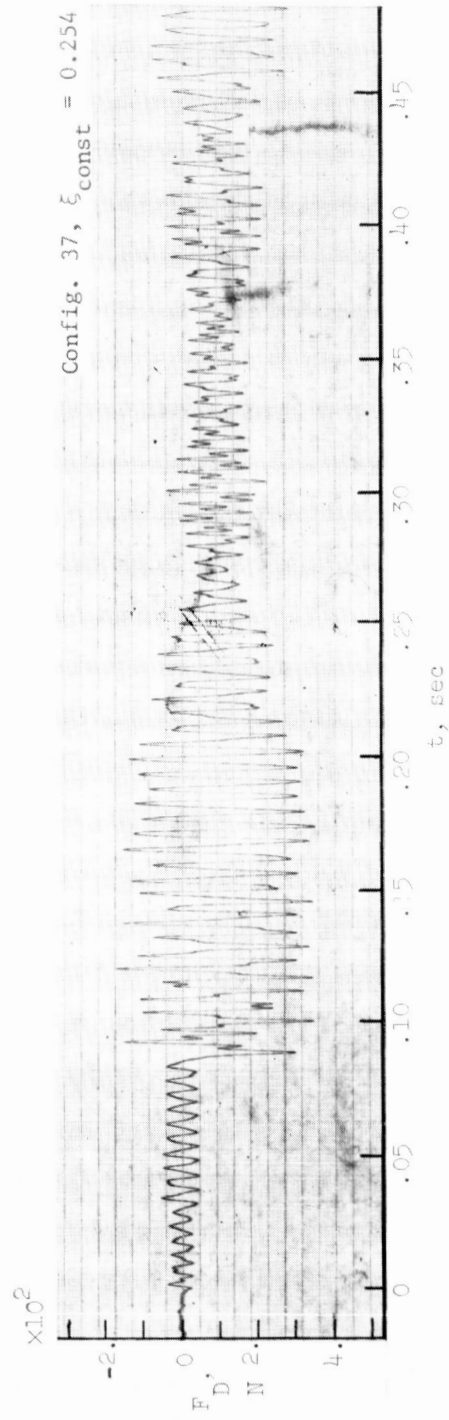
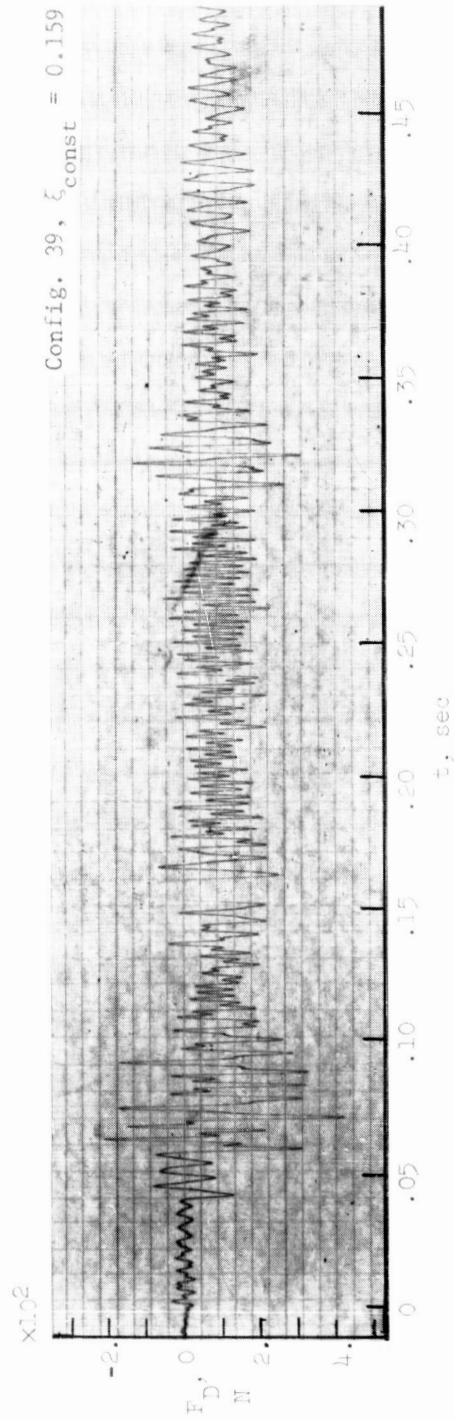
(c) Hemisflo canopies - Continued.

Figure 8. - Continued.



(c) Hemisflo canopies - Concluded.

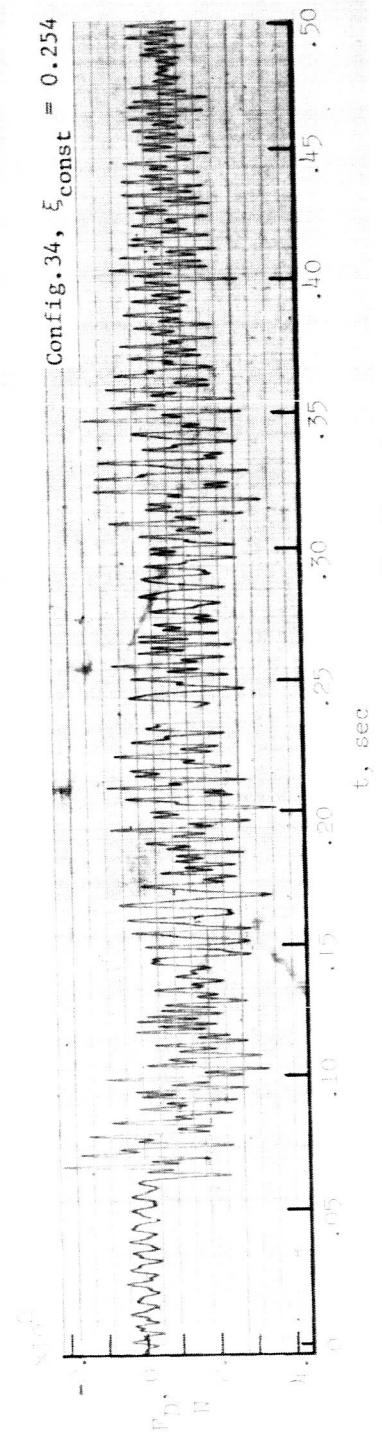
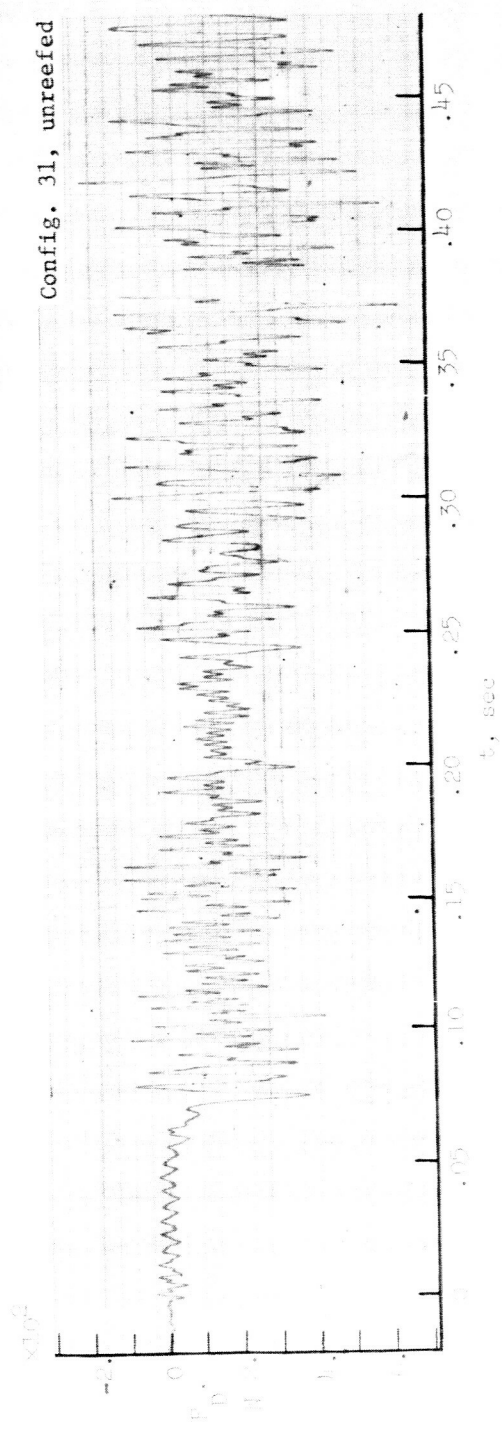
Figure 8. - Continued.



(d) Disk-gap-band canopies.

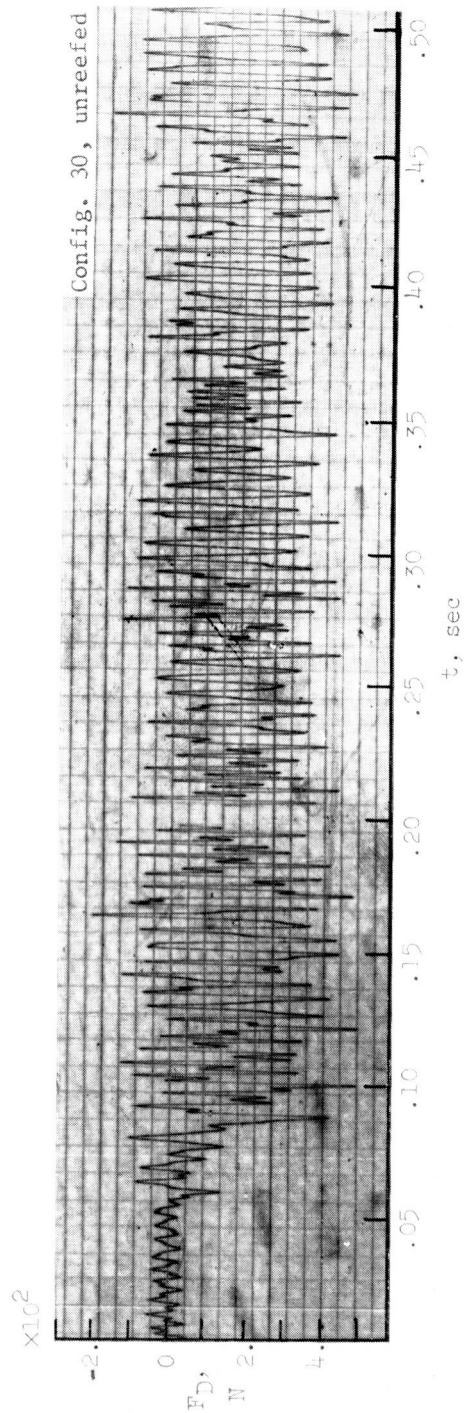
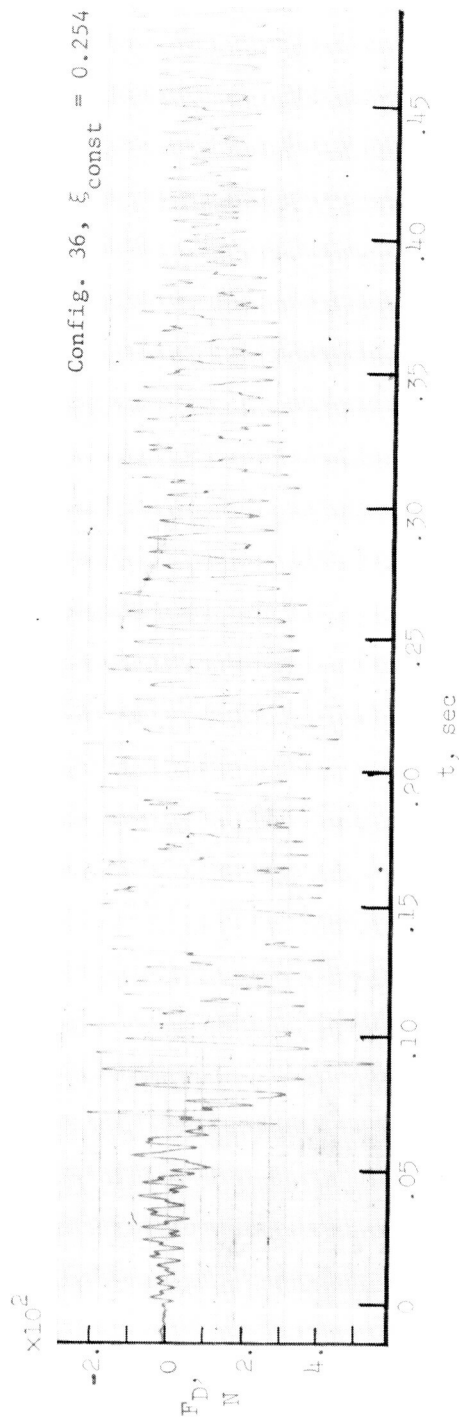
Figure 8. - Continued.





(d) Disk-gap-band canopies - Continued.

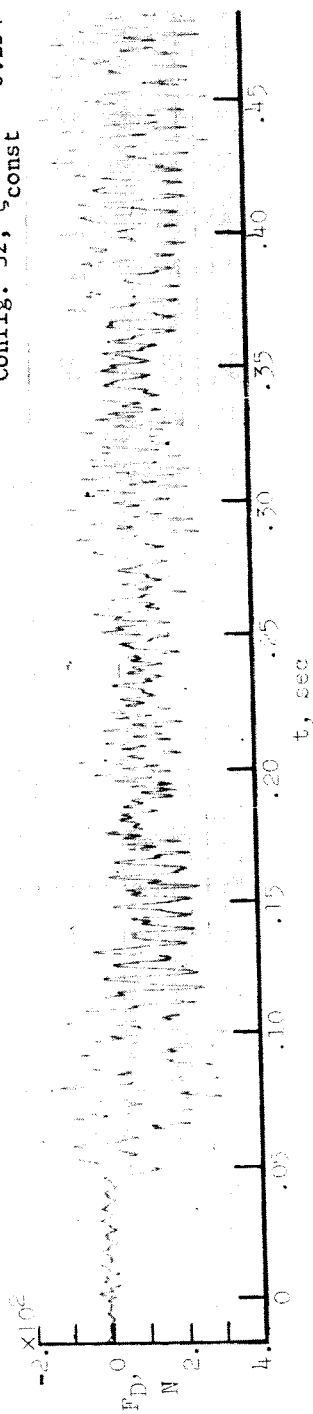
Figure 8.- Continued.



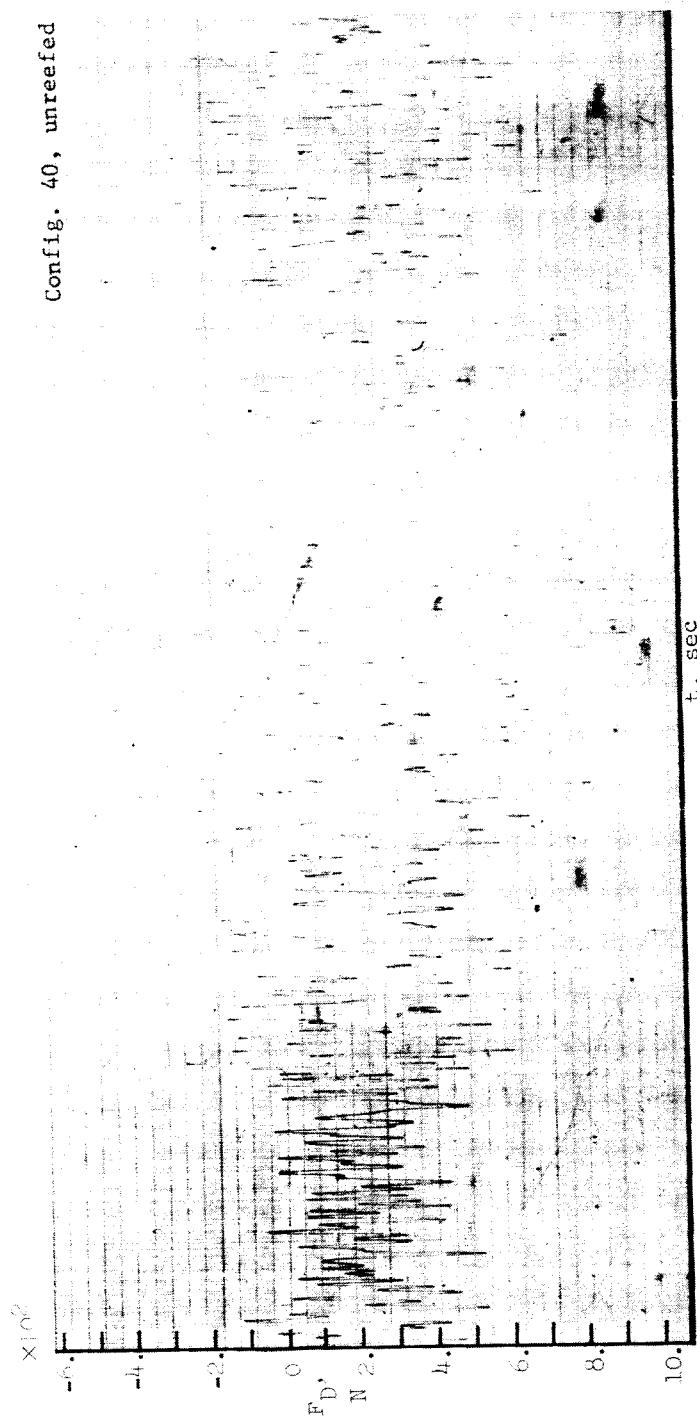
(d) Disk-gap-band canopies - Continued.

Figure 8. - Continued.

Config. 32,  $\xi_{\text{const}} = 0.254$

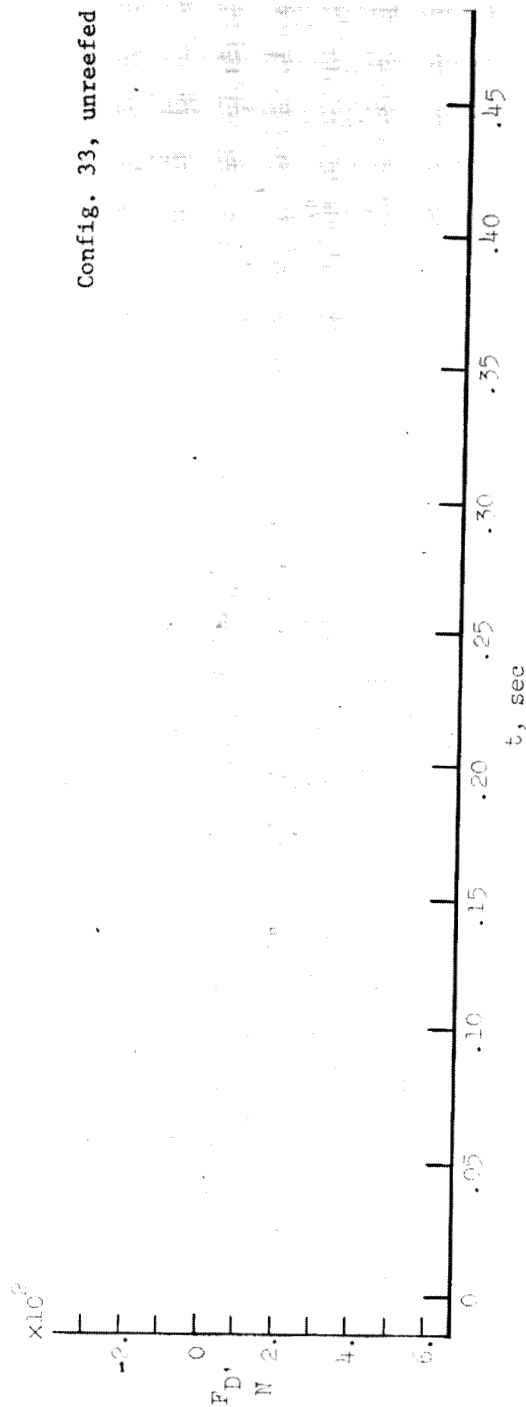
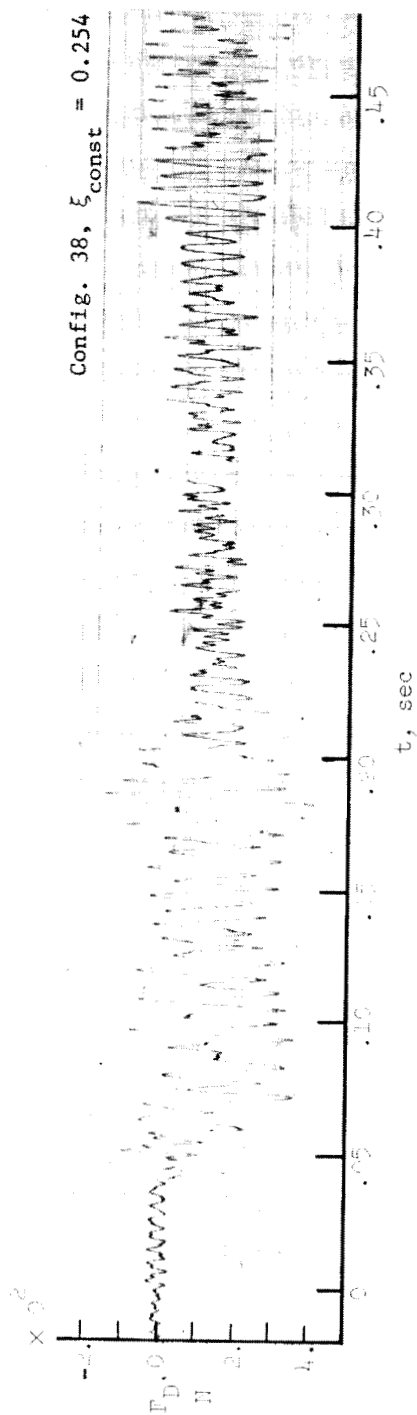


Config. 40, unreefed



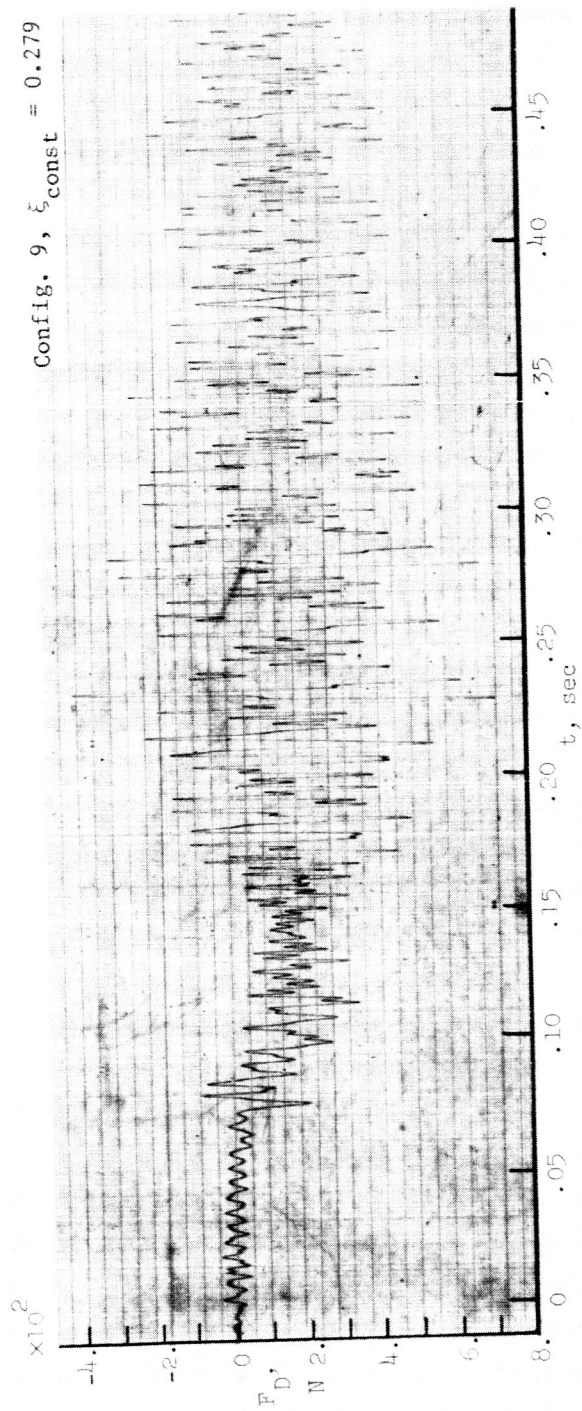
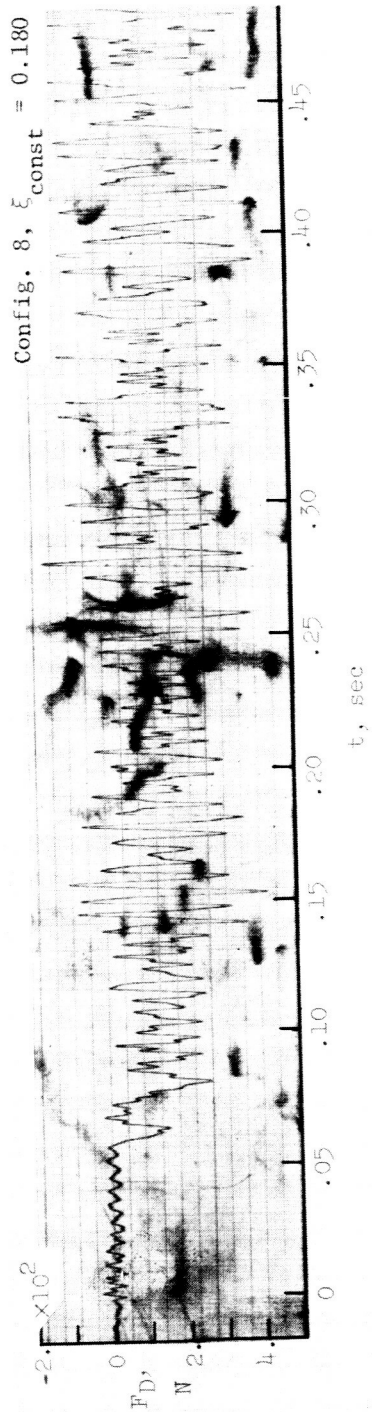
(d) Disk-gap-band canopies - Continued.

Figure 8.- Continued.



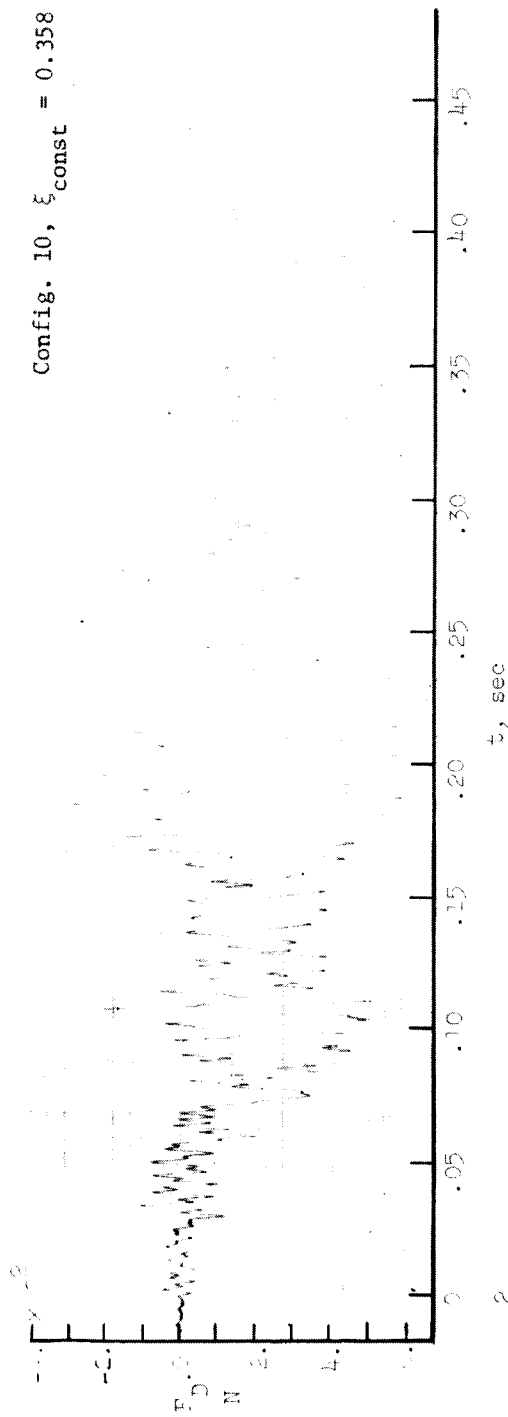
(d) Disk-gap-band canopies - Concluded.

Figure 8. - Continued.

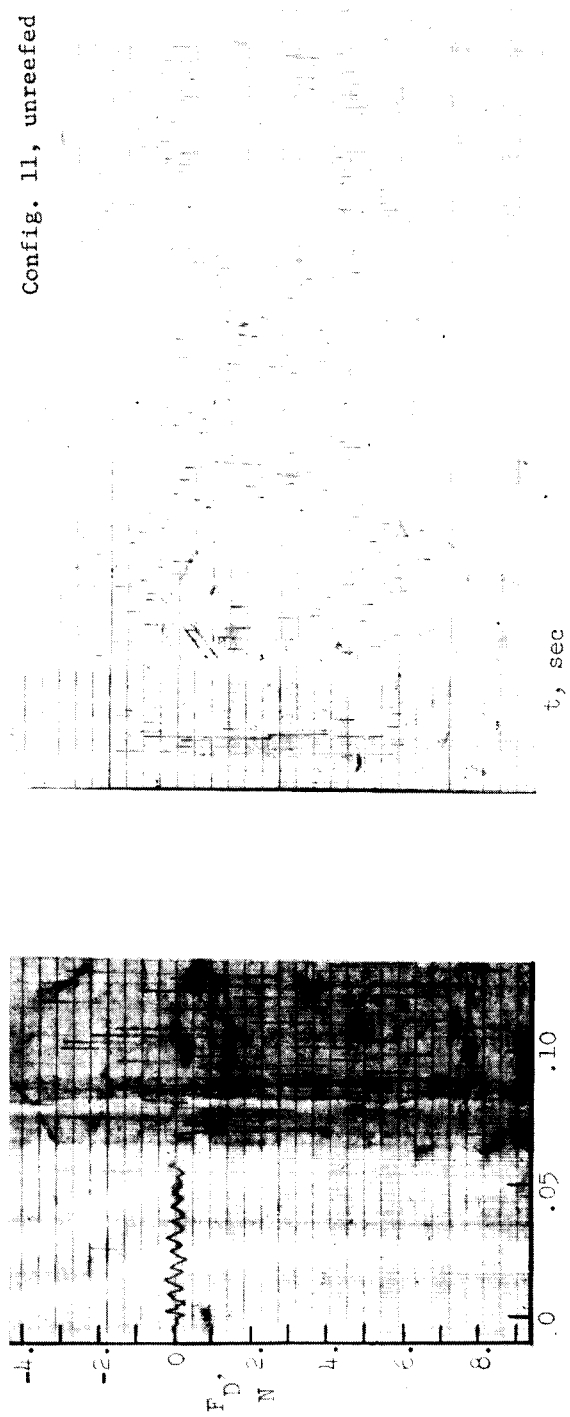


(e) Extended-skirt canopies.

Figure 8. - Continued.

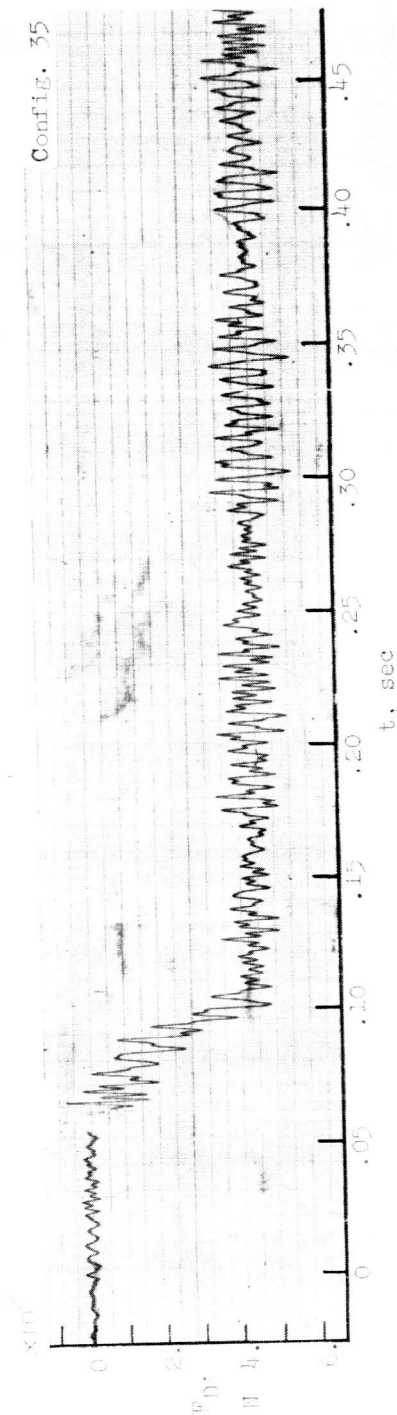
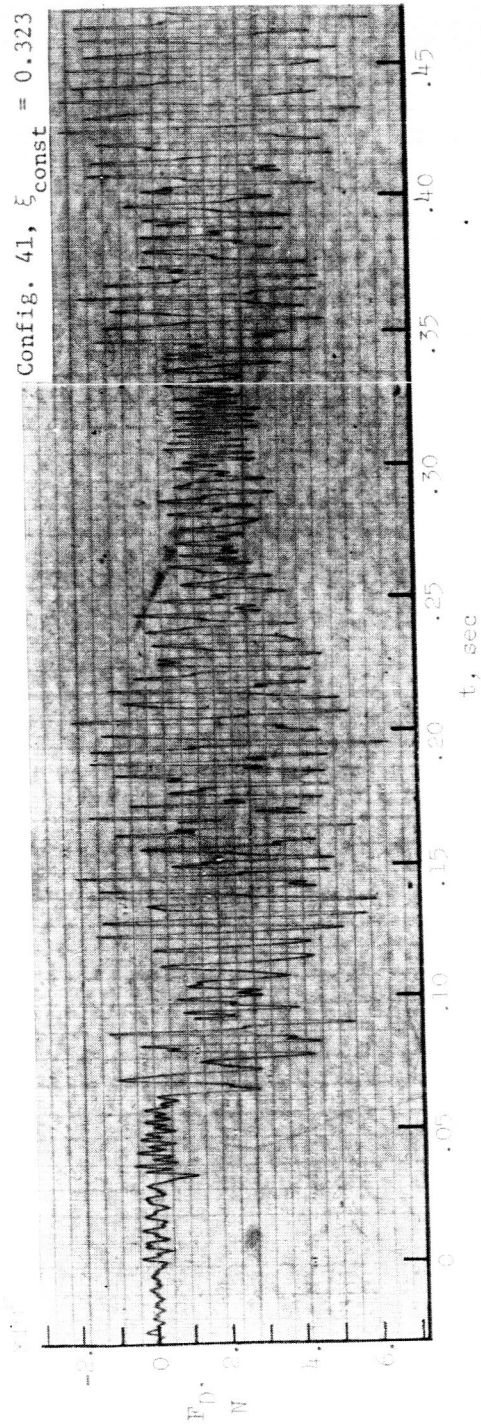
Config. 10,  $\xi_{\text{const}} = 0.358$ 

Config. 11, unreefed



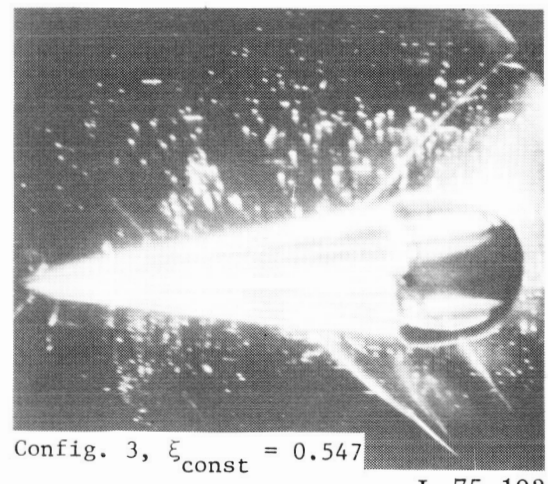
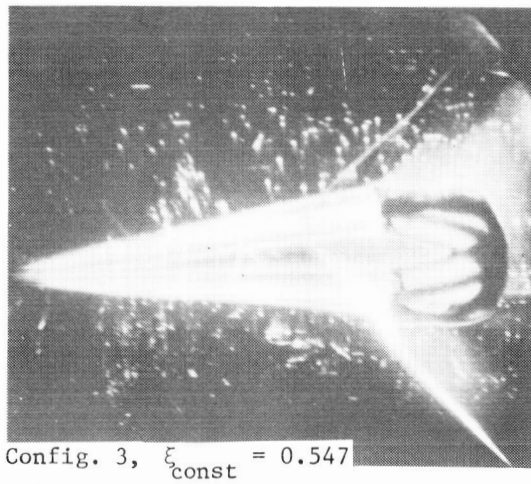
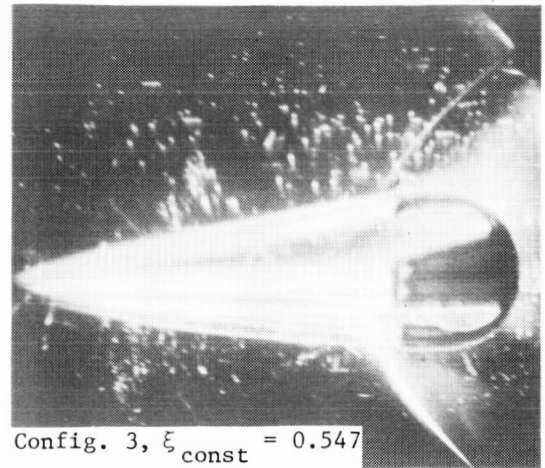
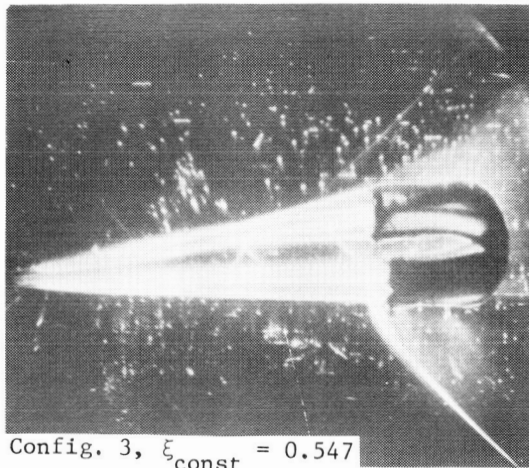
(e) Extended-skirt canopies - Concluded.

Figure 8. - Continued.



(f) Modular cross canopy and ballute.

Figure 8.- Concluded.

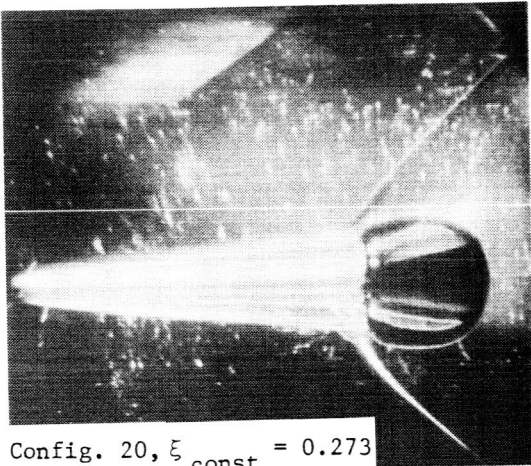


L-75-103

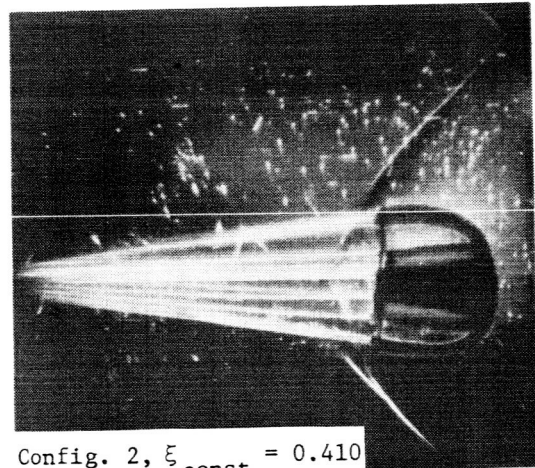
(a) Cross canopies.

Figure 9.- Schlieren photographs of configurations tested.

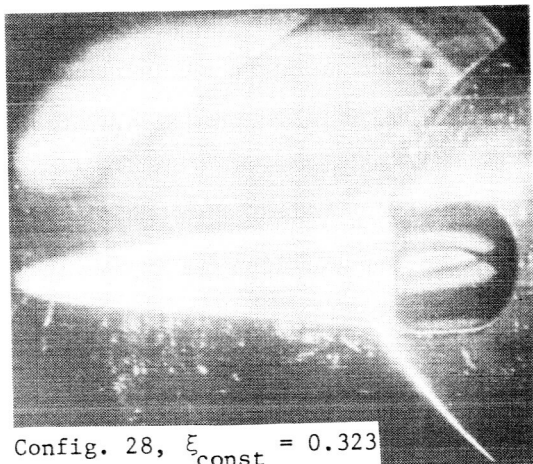




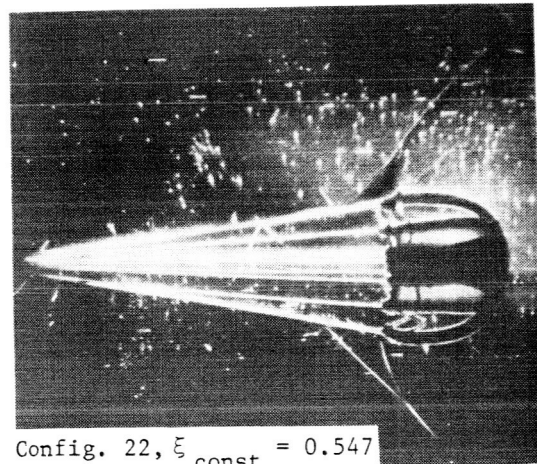
Config. 20,  $\xi_{\text{const}} = 0.273$



Config. 2,  $\xi_{\text{const}} = 0.410$



Config. 28,  $\xi_{\text{const}} = 0.323$

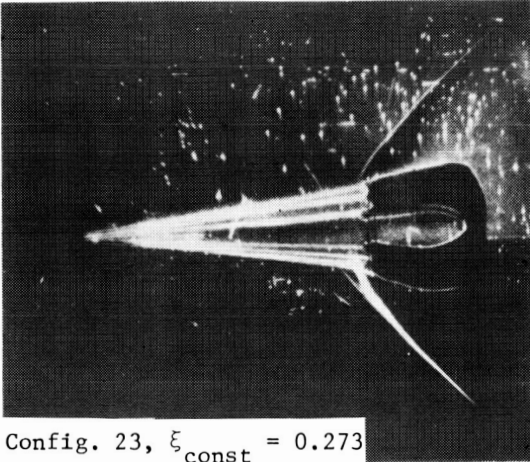


Config. 22,  $\xi_{\text{const}} = 0.547$

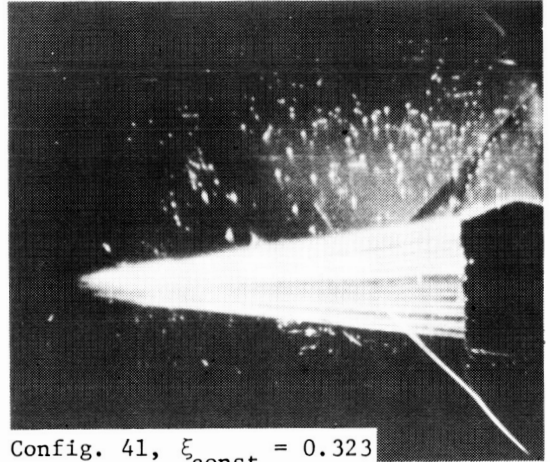
L-75-104

(a) Cross canopies - Continued.

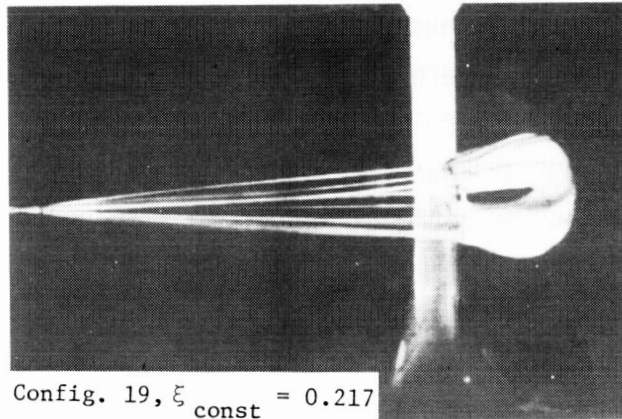
Figure 9.- Continued.



Config. 23,  $\xi_{\text{const}} = 0.273$



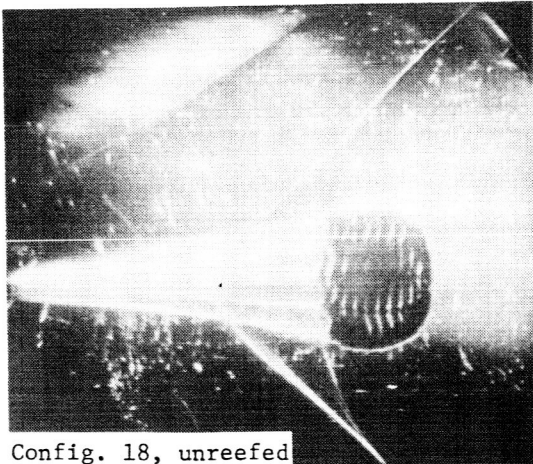
Config. 41,  $\xi_{\text{const}} = 0.323$



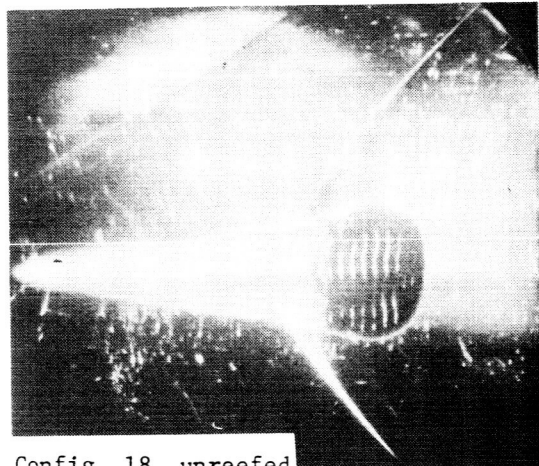
Config. 19,  $\xi_{\text{const}} = 0.217$

(a) Cross canopies - Concluded.

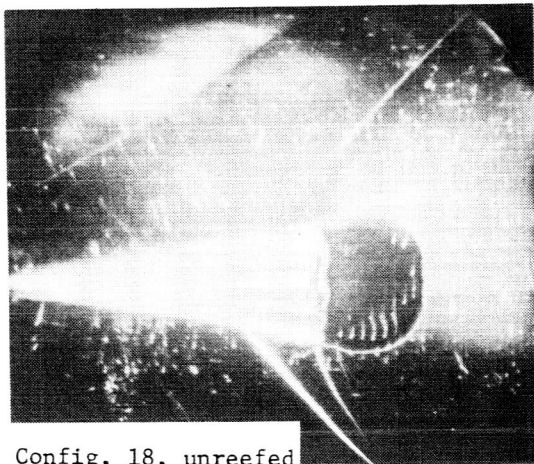
Figure 9.- Continued. L-75-105



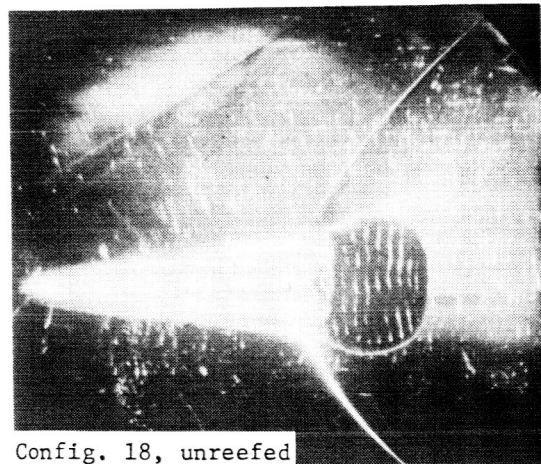
Config. 18, unreefed



Config. 18, unreefed



Config. 18, unreefed

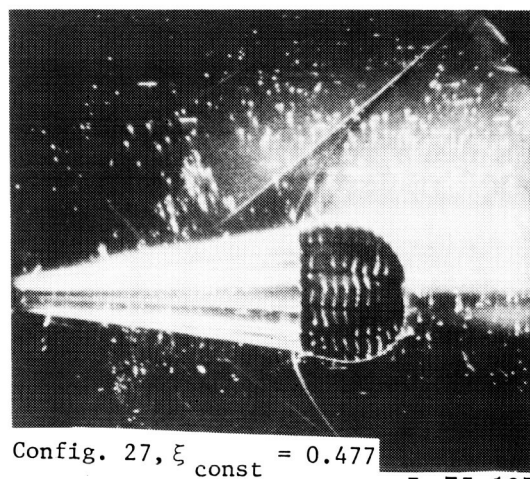
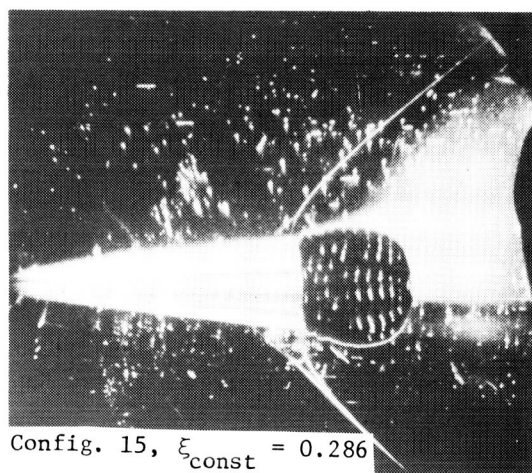
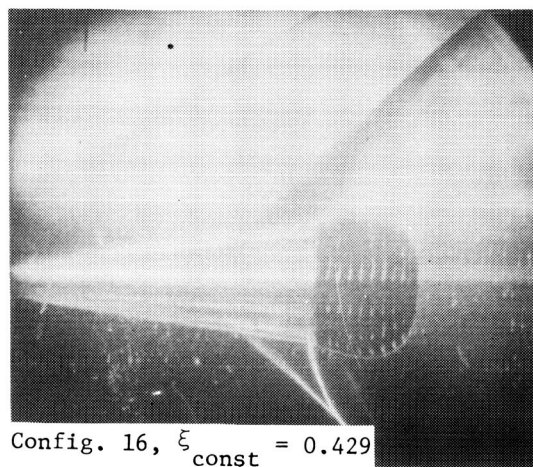
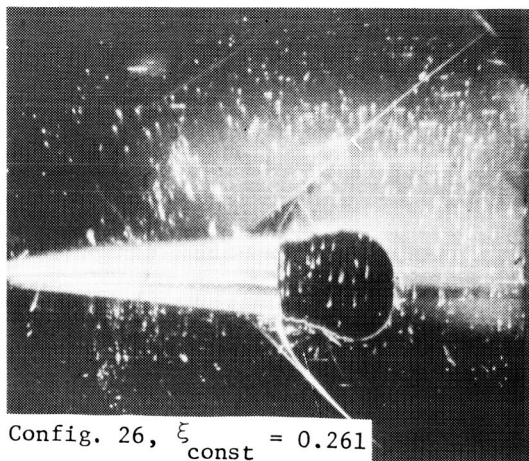


Config. 18, unreefed

L-75-106

(b) Hemisflo canopies.

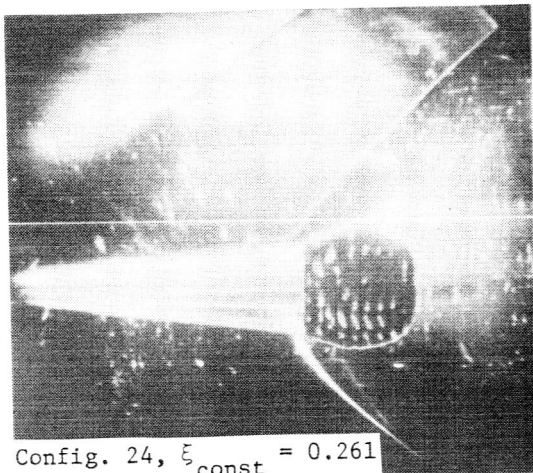
Figure 9.- Continued.



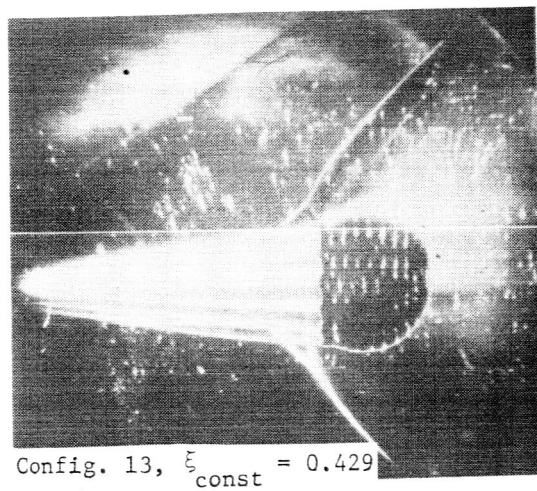
L-75-107

(b) Hemisflo canopies - Continued.

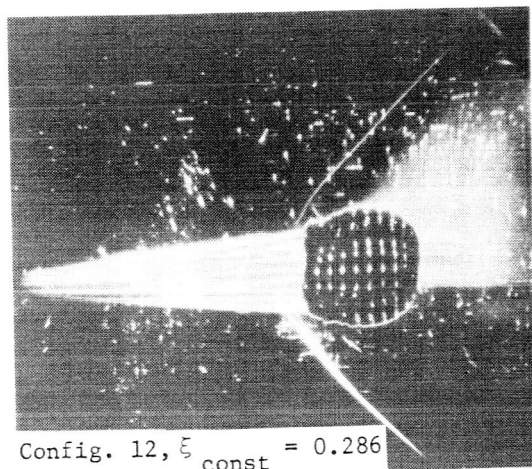
Figure 9.- Continued.



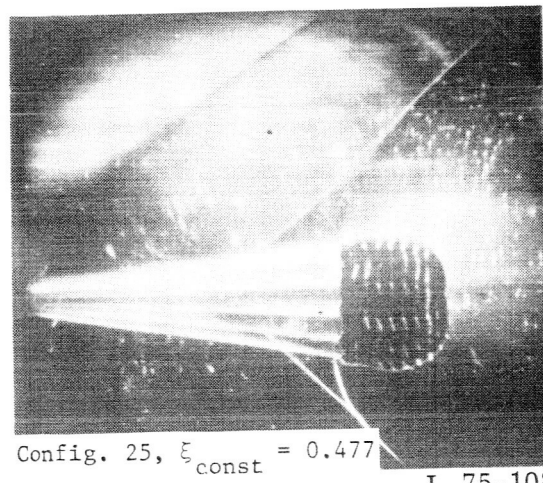
Config. 24,  $\xi_{\text{const}} = 0.261$



Config. 13,  $\xi_{\text{const}} = 0.429$



Config. 12,  $\xi_{\text{const}} = 0.286$



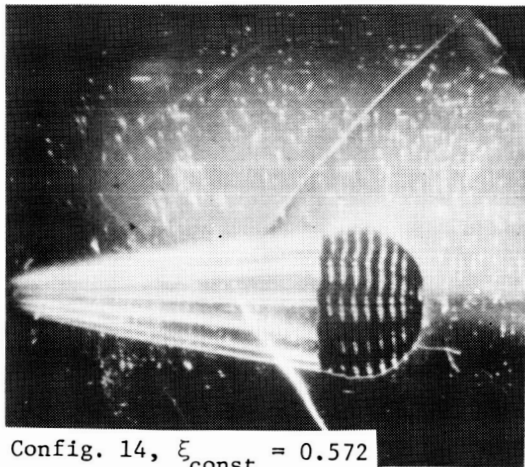
Config. 25,  $\xi_{\text{const}} = 0.477$

L-75-108

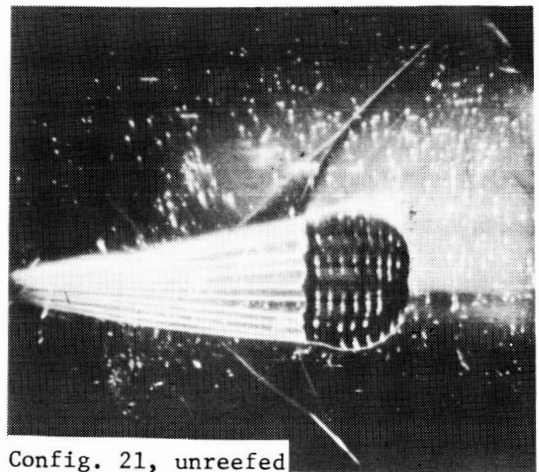
(b) Hemisflo canopies - Continued.

Figure 9.- Continued.

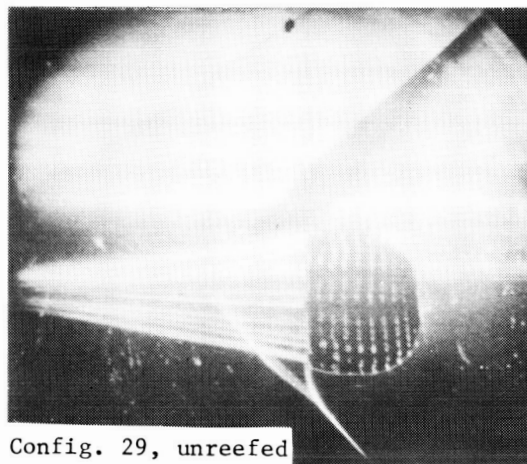




Config. 14,  $\xi_{\text{const}} = 0.572$



Config. 21, unreefed

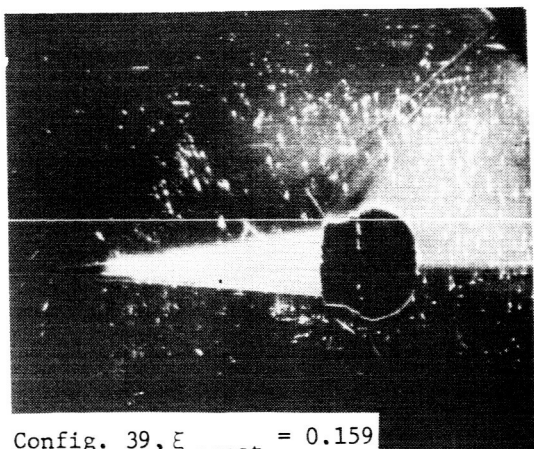


Config. 29, unreefed

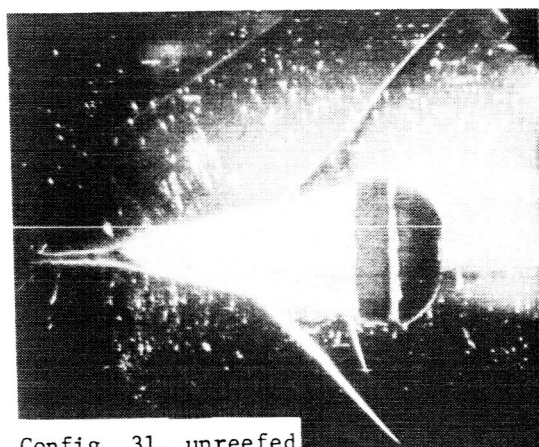
(b) Hemisflo canopies - Concluded.

L-75-109

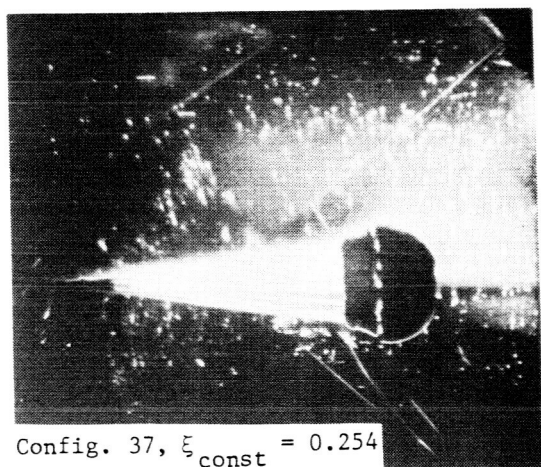
Figure 9.- Continued.



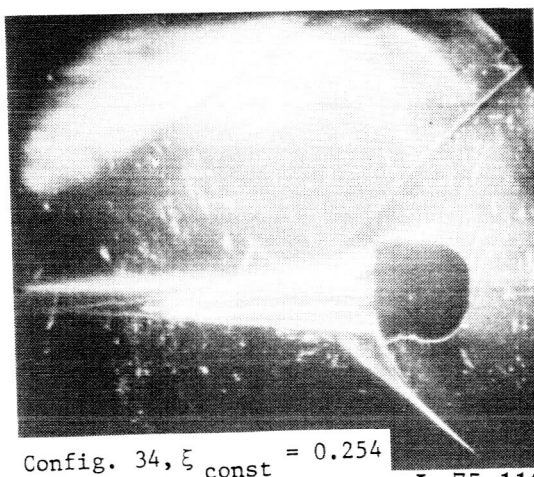
Config. 39,  $\xi_{\text{const}} = 0.159$



Config. 31, unreefed



Config. 37,  $\xi_{\text{const}} = 0.254$

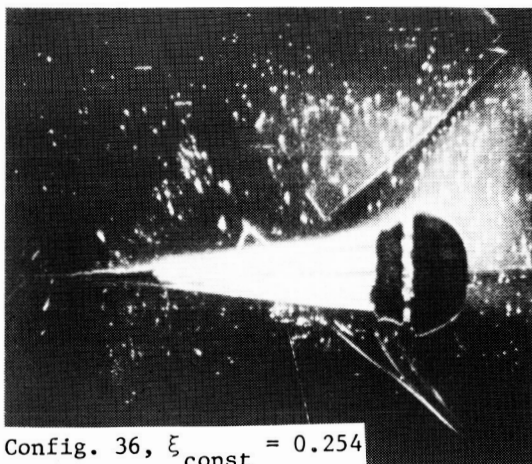


Config. 34,  $\xi_{\text{const}} = 0.254$

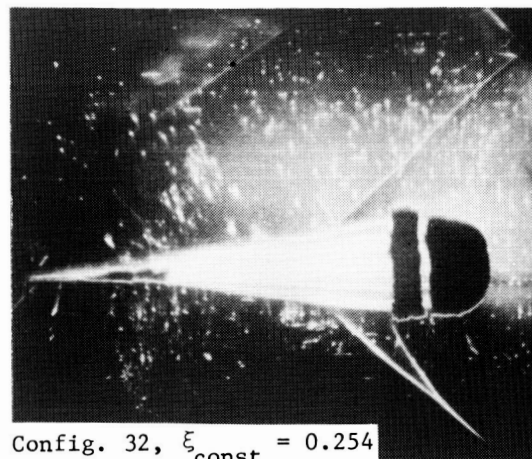
L-75-110

(c) Disk-gap-band canopies.

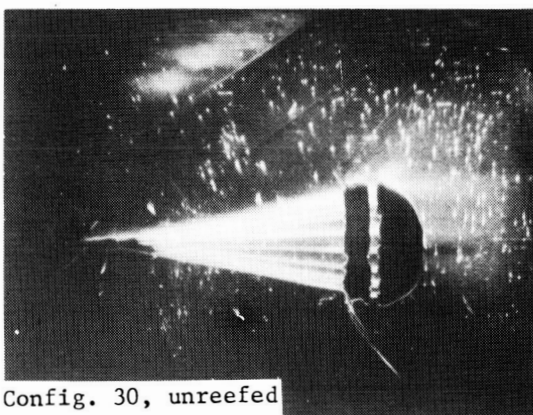
Figure 9.- Continued.



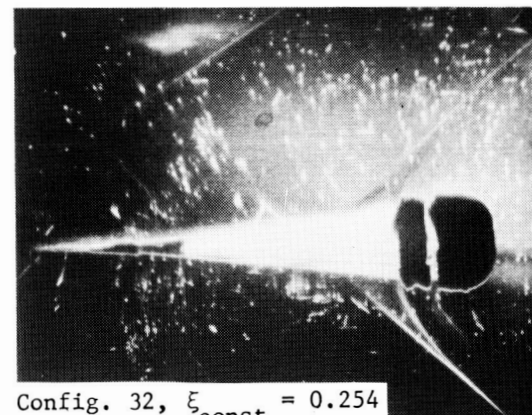
Config. 36,  $\xi_{\text{const}} = 0.254$



Config. 32,  $\xi_{\text{const}} = 0.254$



Config. 30, unreefed



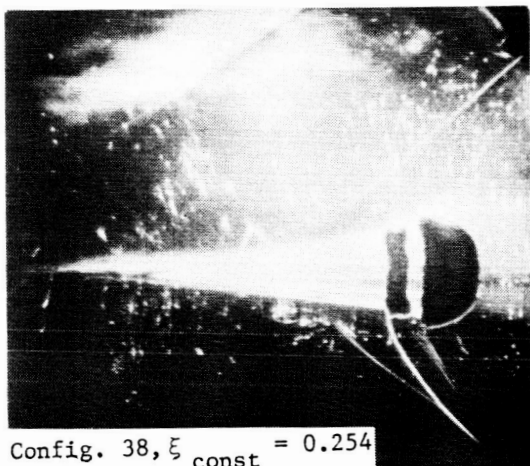
Config. 32,  $\xi_{\text{const}} = 0.254$

L-75-111

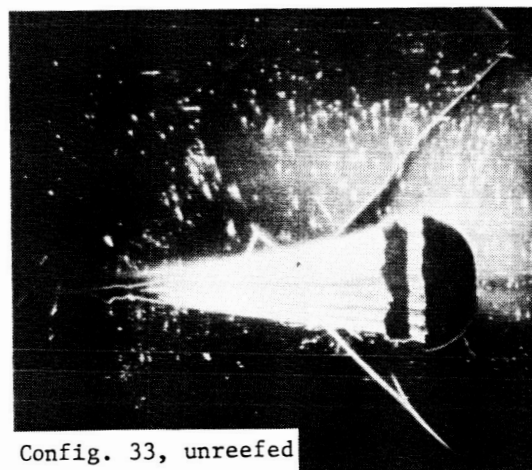
(c) Disk-gap-band canopies – Continued.

Figure 9.- Continued.





Config. 38,  $\xi_{\text{const}} = 0.254$

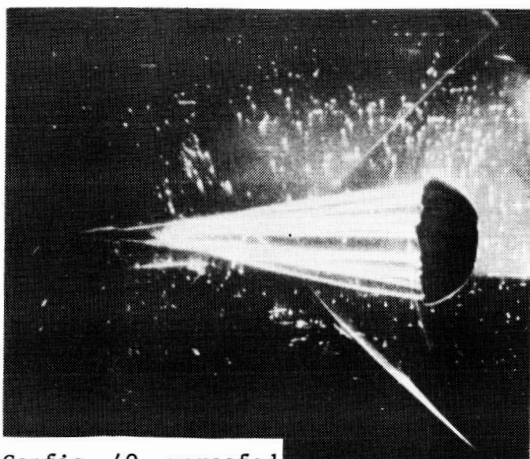


Config. 33, unreefed

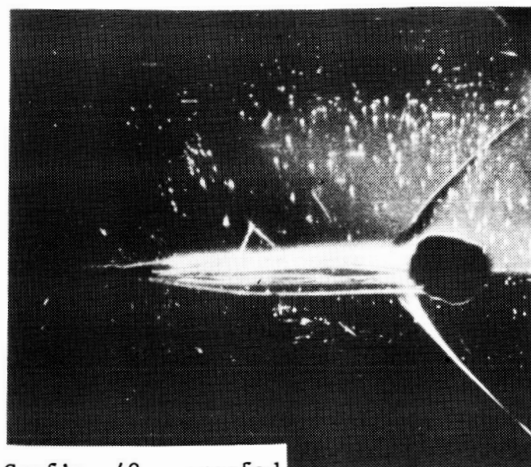
L-75-112

(c) Disk-gap-band canopies – Continued.

Figure 9.- Continued.



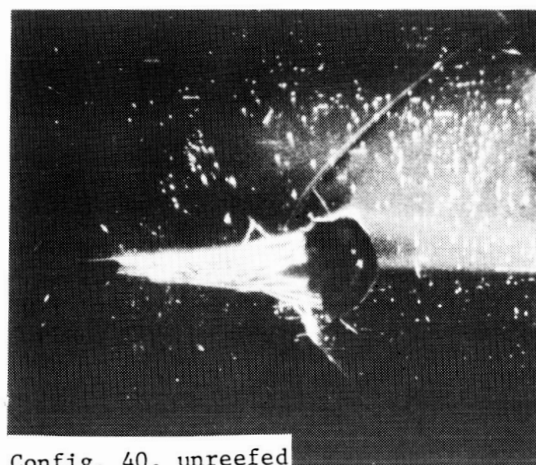
Config. 40, unreefed



Config. 40, unreefed



Config. 40, unreefed

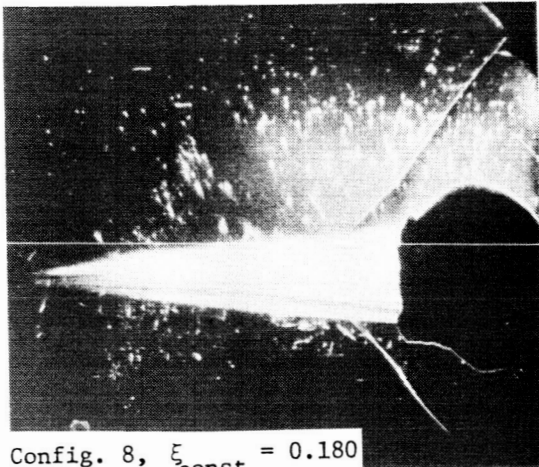


Config. 40, unreefed

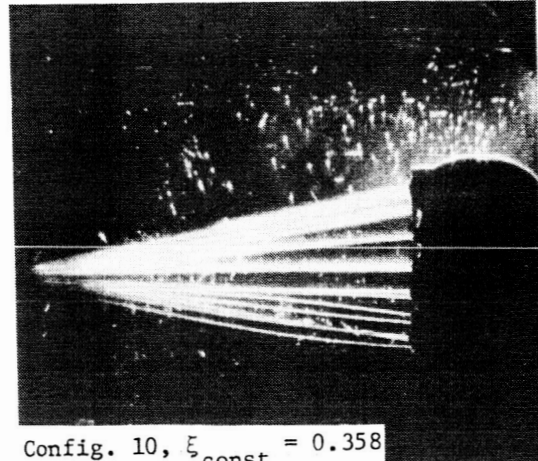
L-75-113

(c) Disk-gap-band canopies (standard flat canopy) – Concluded.

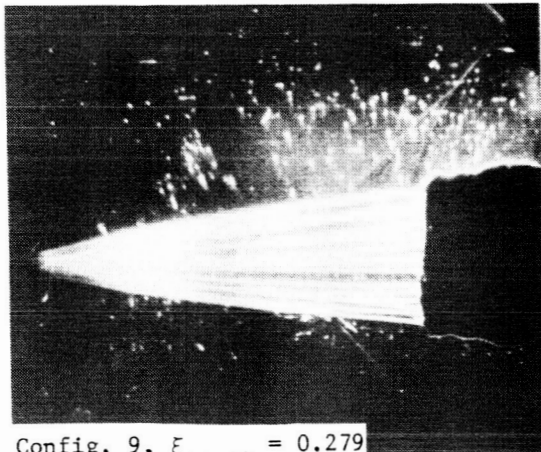
Figure 9. - Continued.



Config. 8,  $\xi_{\text{const}} = 0.180$



Config. 10,  $\xi_{\text{const}} = 0.358$



Config. 9,  $\xi_{\text{const}} = 0.279$

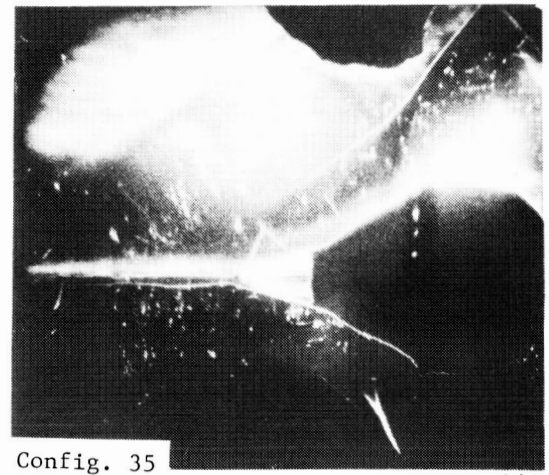
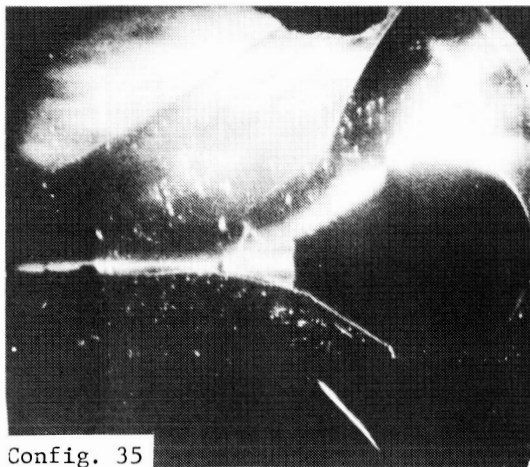
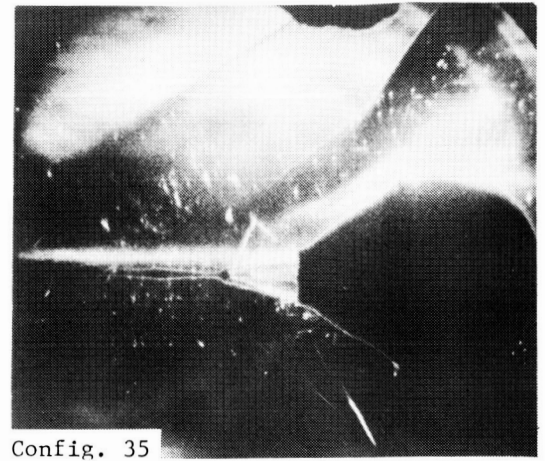
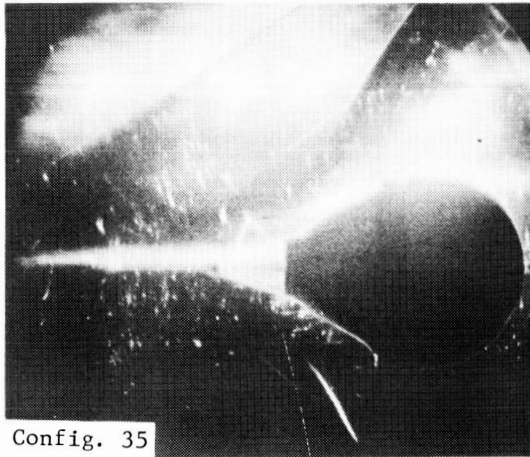


Config. 11, unreefed

L-75-114

(d) Extended-skirt canopies.

Figure 9.- Continued.



L-75-115

(e) Ballute.

Figure 9.- Concluded.

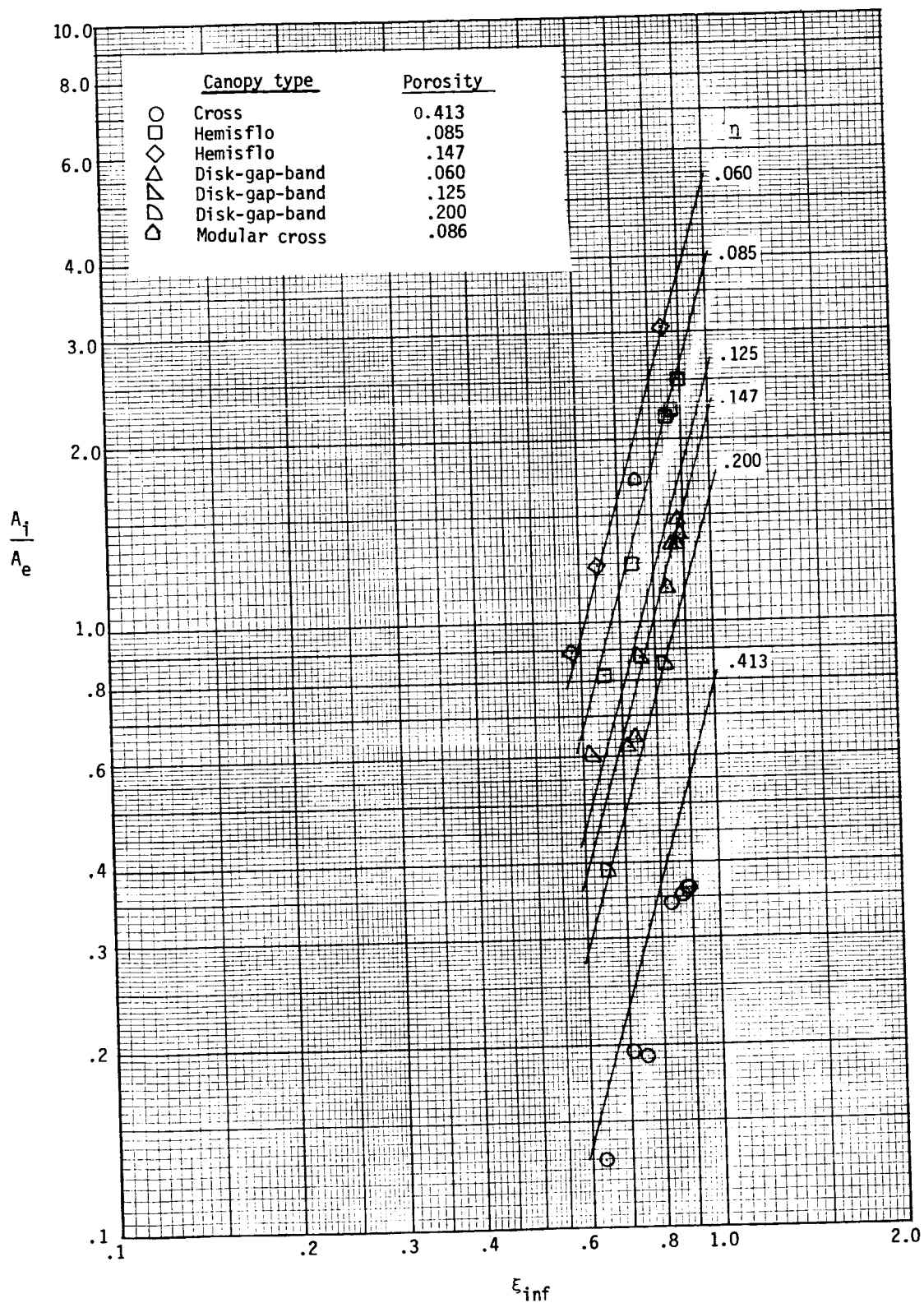


Figure 10.- Variation of area ratio with inflated reefing ratio at  $M = 1.80$ .

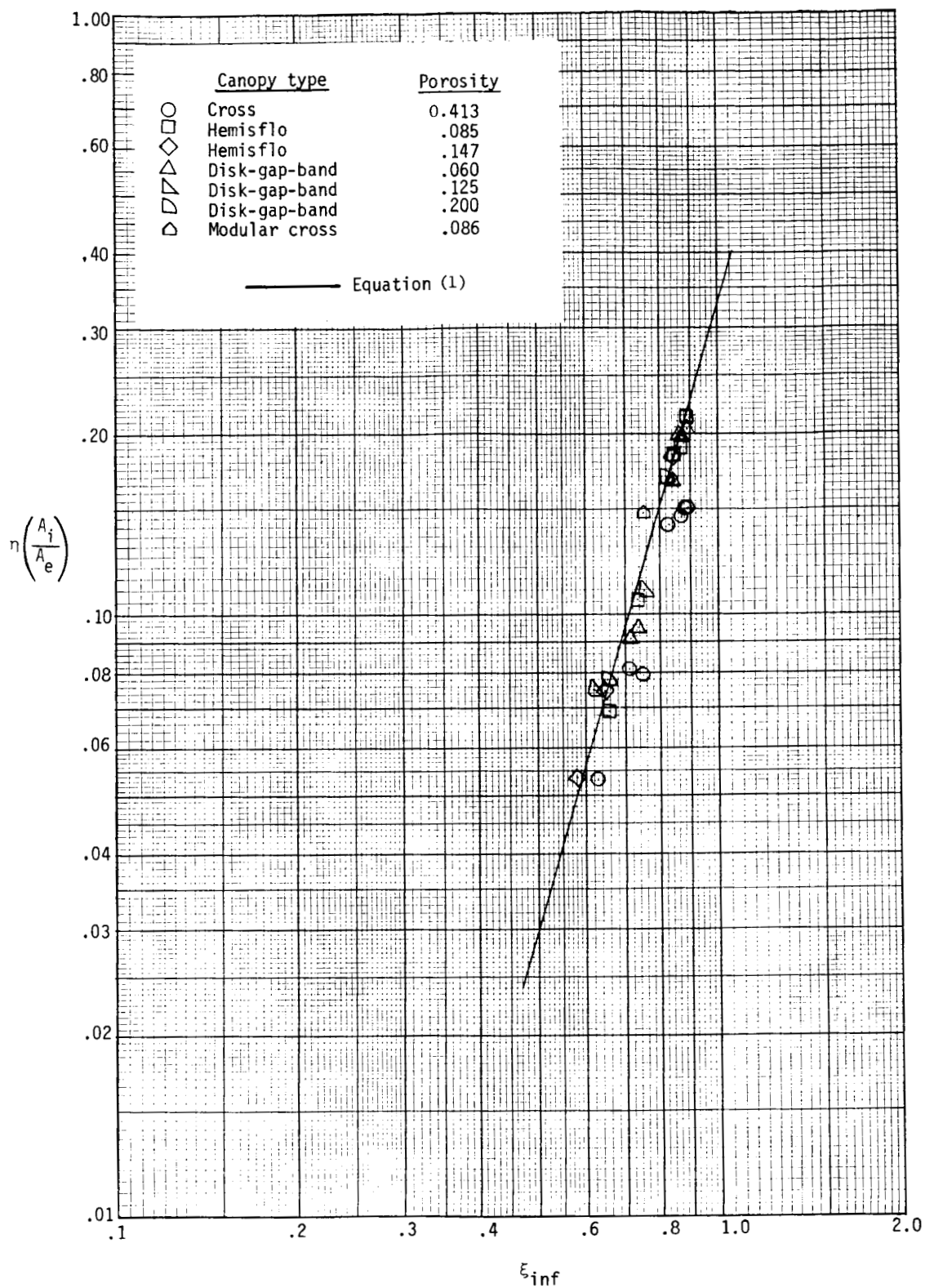


Figure 11.- Correlation between area ratio and inflated reefing ratio for a variety of parachute configurations at  $M = 1.80$ .

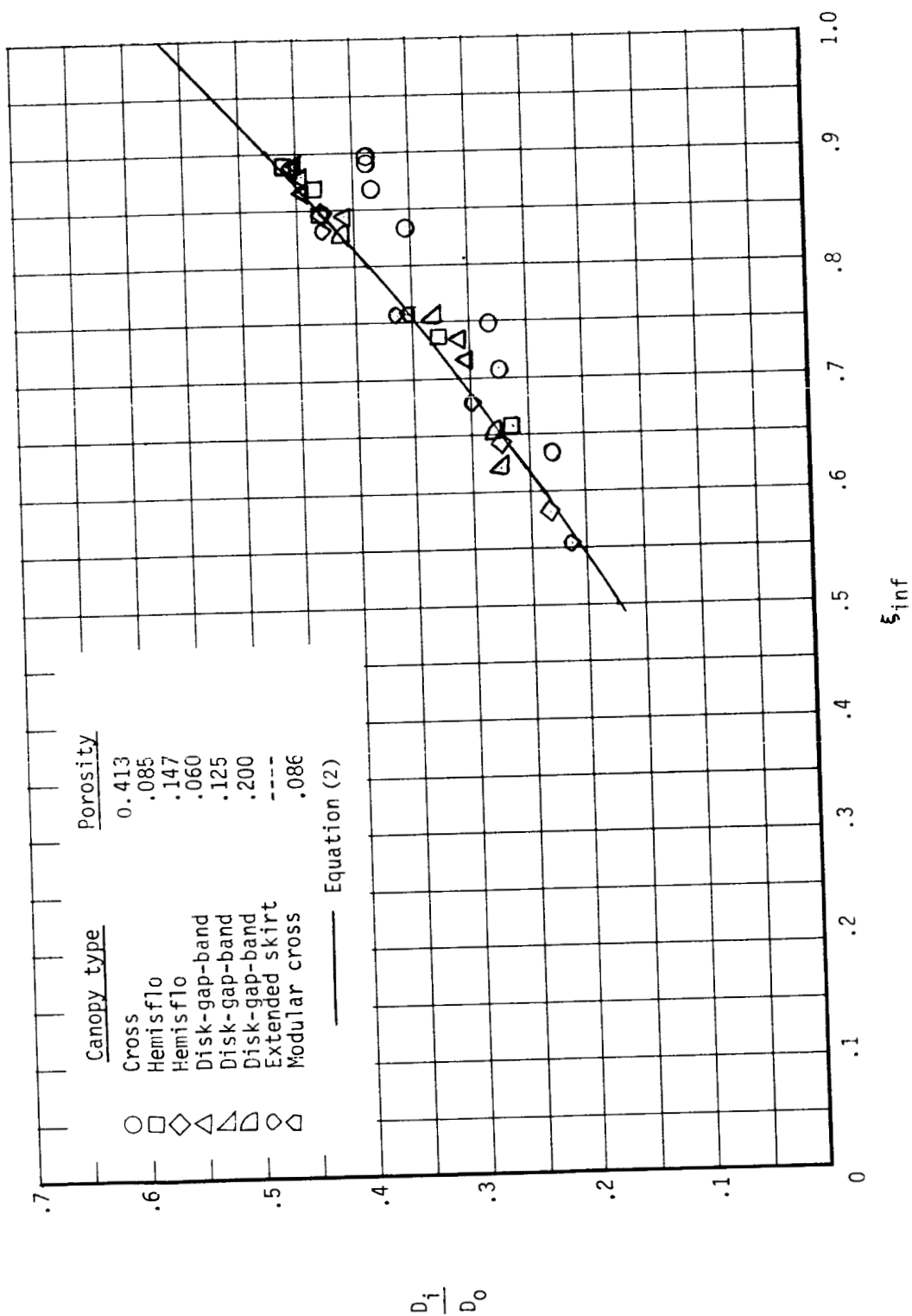


Figure 12.- Variation of diameter ratio with inflated reefing ratio.



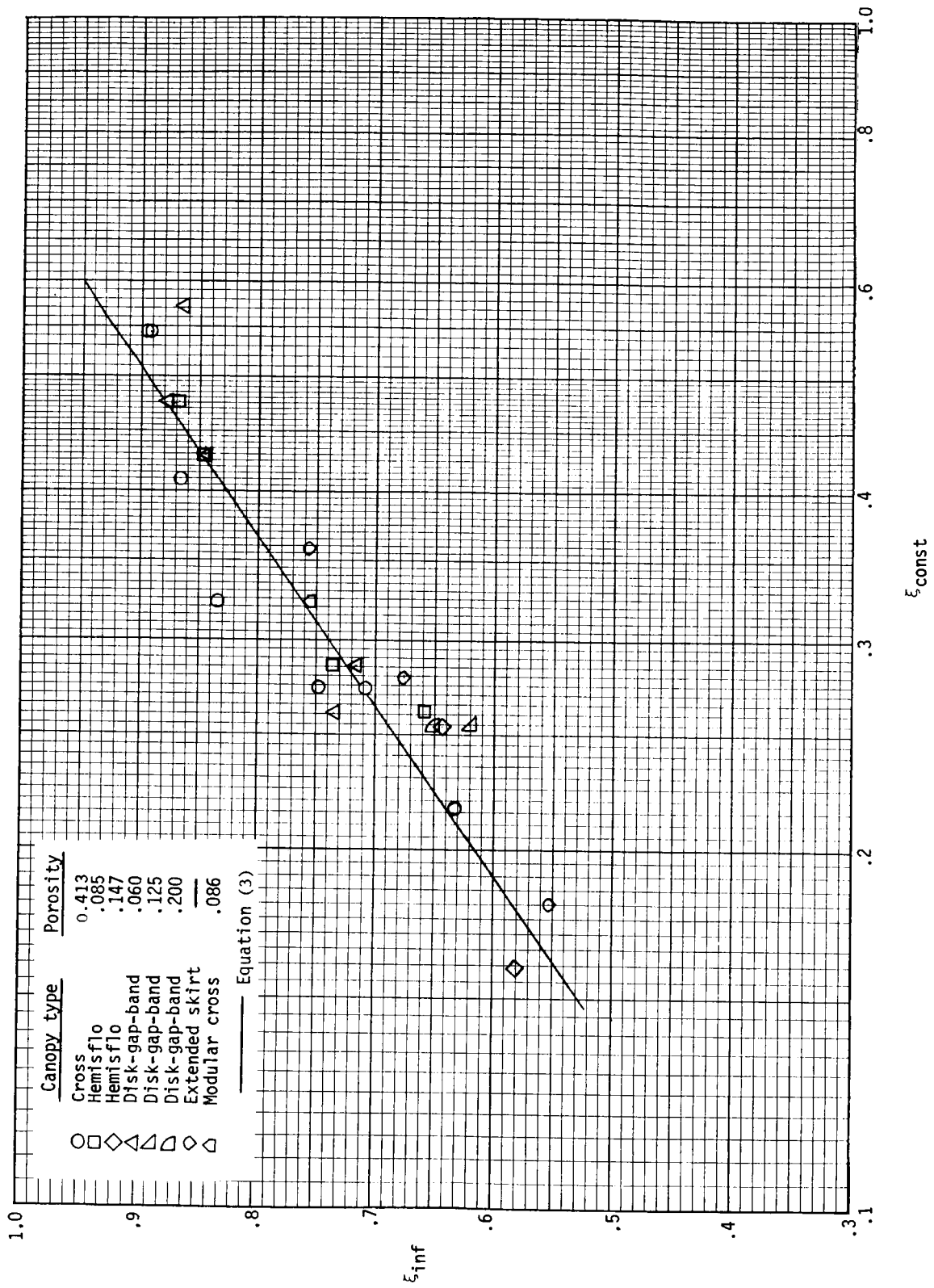


Figure 13. - Variation of inflated reefing ratio with constructed reefing ratio.



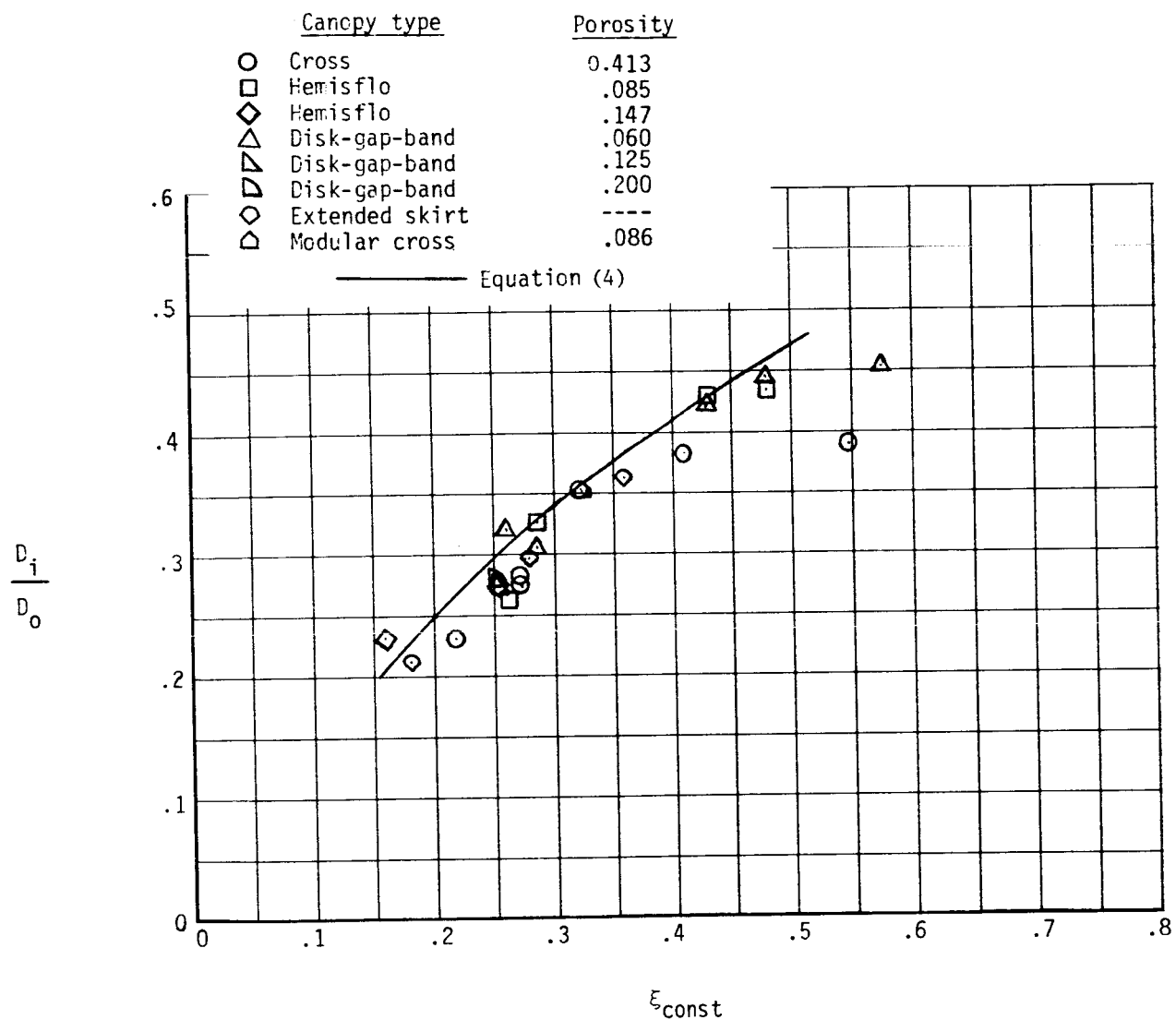


Figure 14.- Variation of  $D_i/D_o$  with constructed reefing ratio.

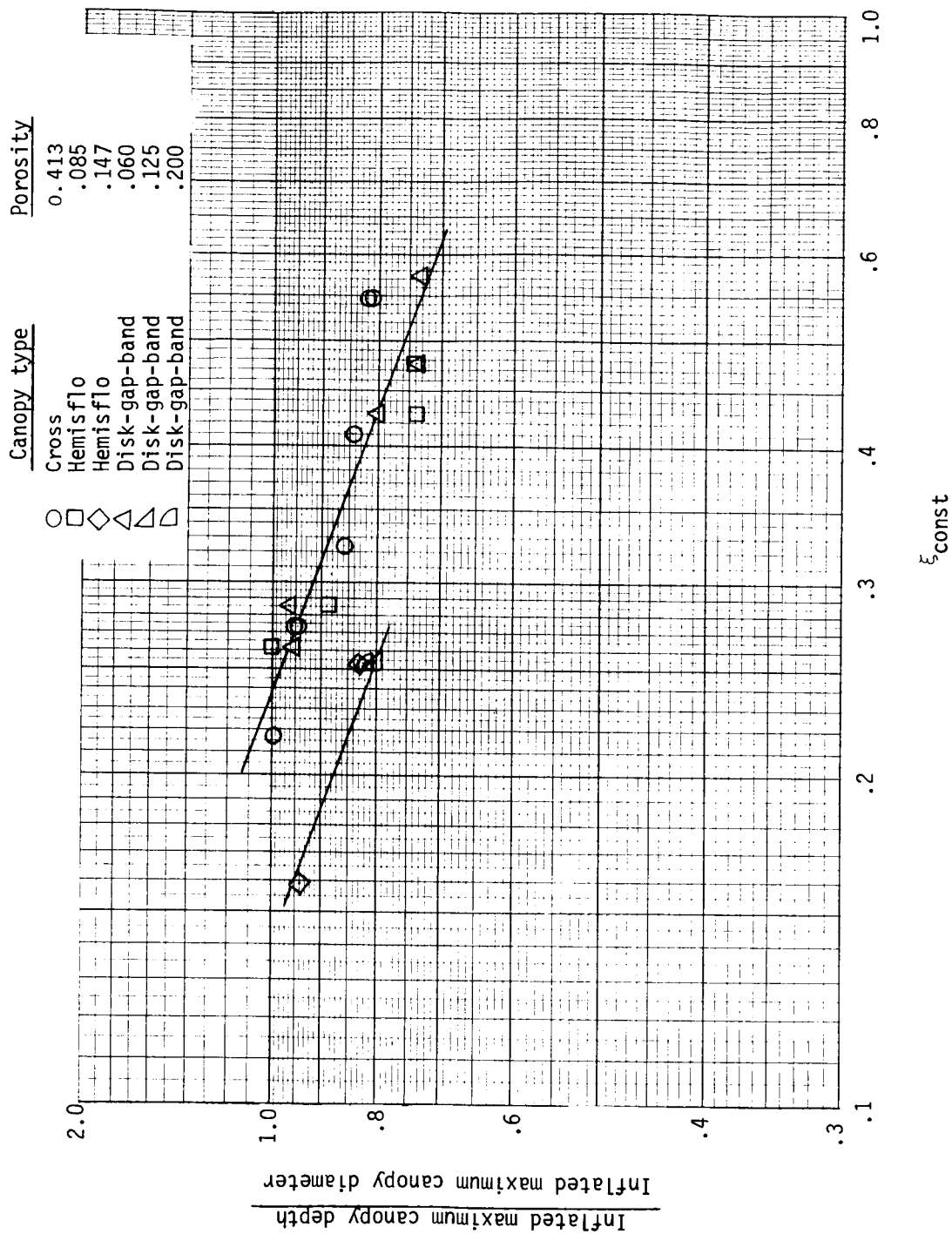


Figure 15.- Effect of constructed reefing ratio on canopy shape.

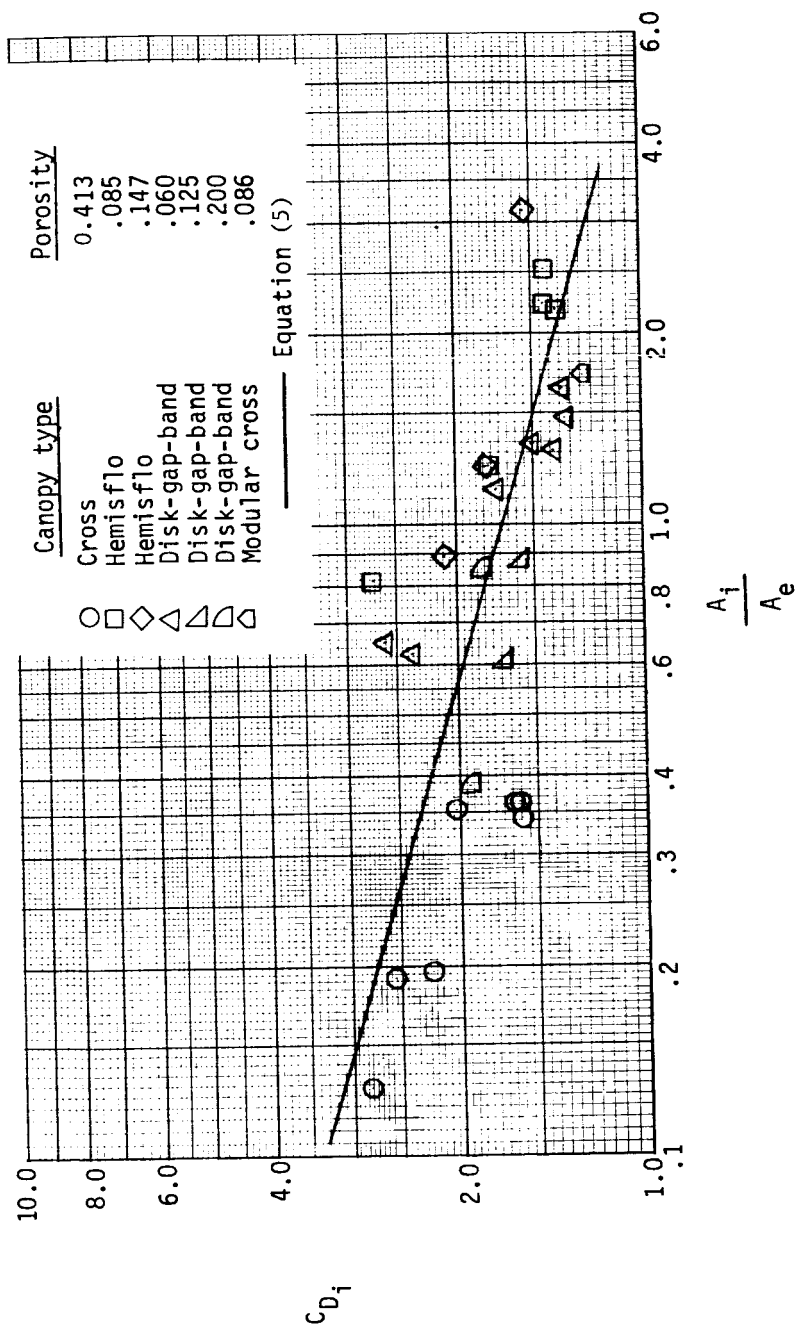


Figure 16.- Comparison of measured data with correlation equation for the variation of drag coefficient based on inlet area with ratio of inlet area to exit area at  $M = 1.80$ .

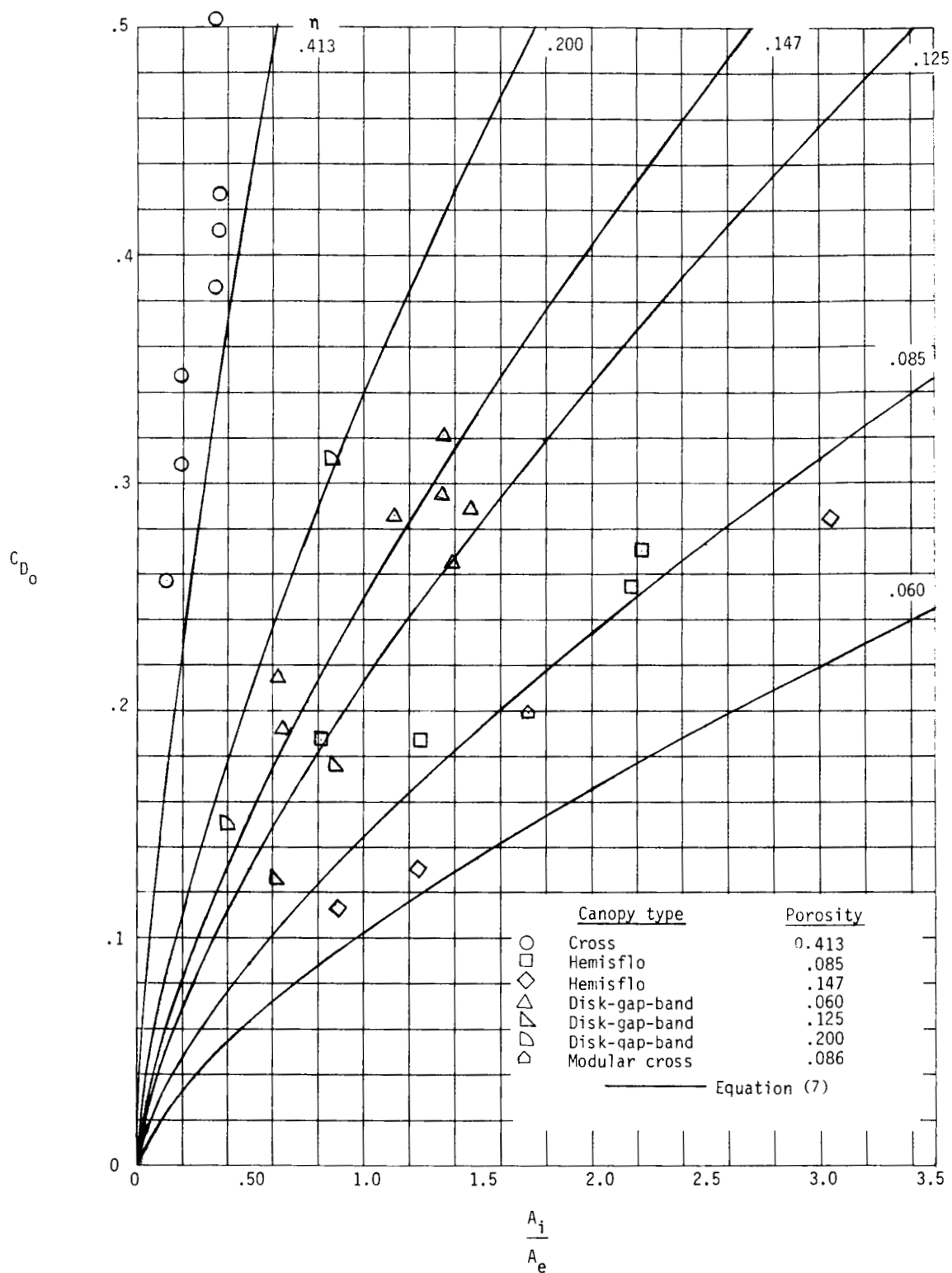


Figure 17.- Comparison of measured data with correlation equation for the variation of drag coefficient with ratio of inlet area to exit area at  $M = 1.80$ .

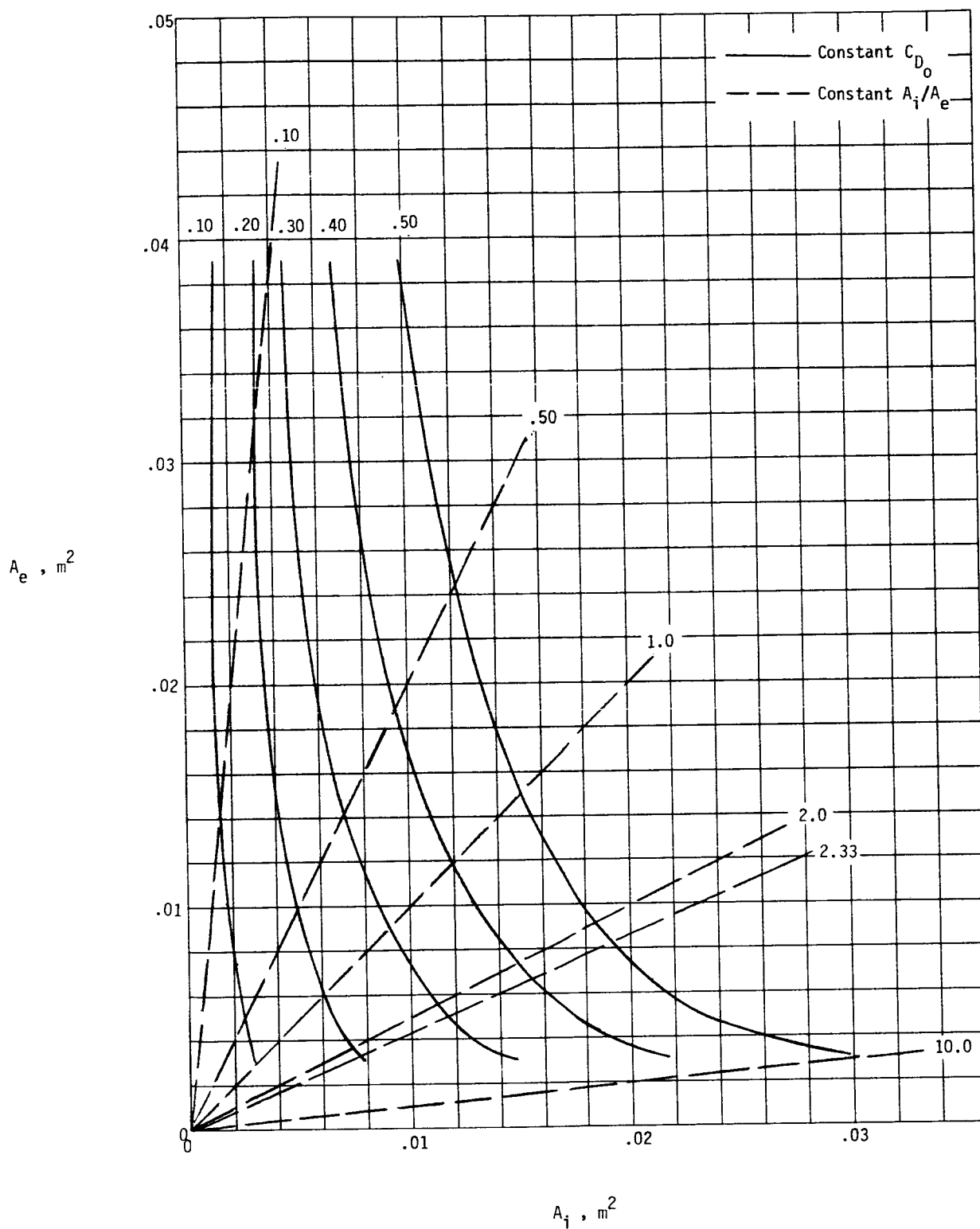


Figure 18.- Effect of area changes on drag coefficient of parachutes at  $M = 1.80$ .

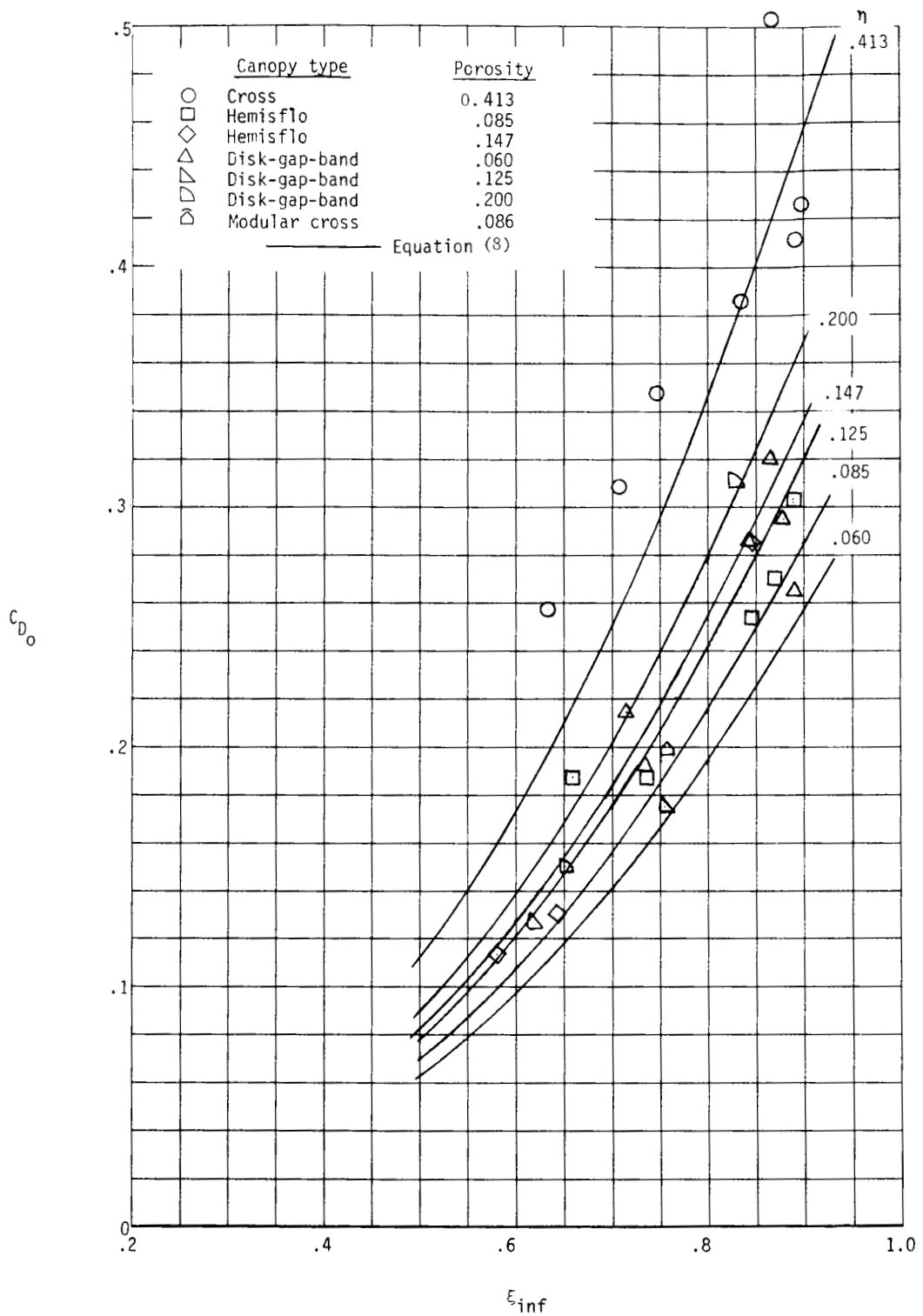


Figure 19.- Comparison of measured data with correlation equation for the variation of drag coefficient with inflated reefing ratio at  $M = 1.80$ .

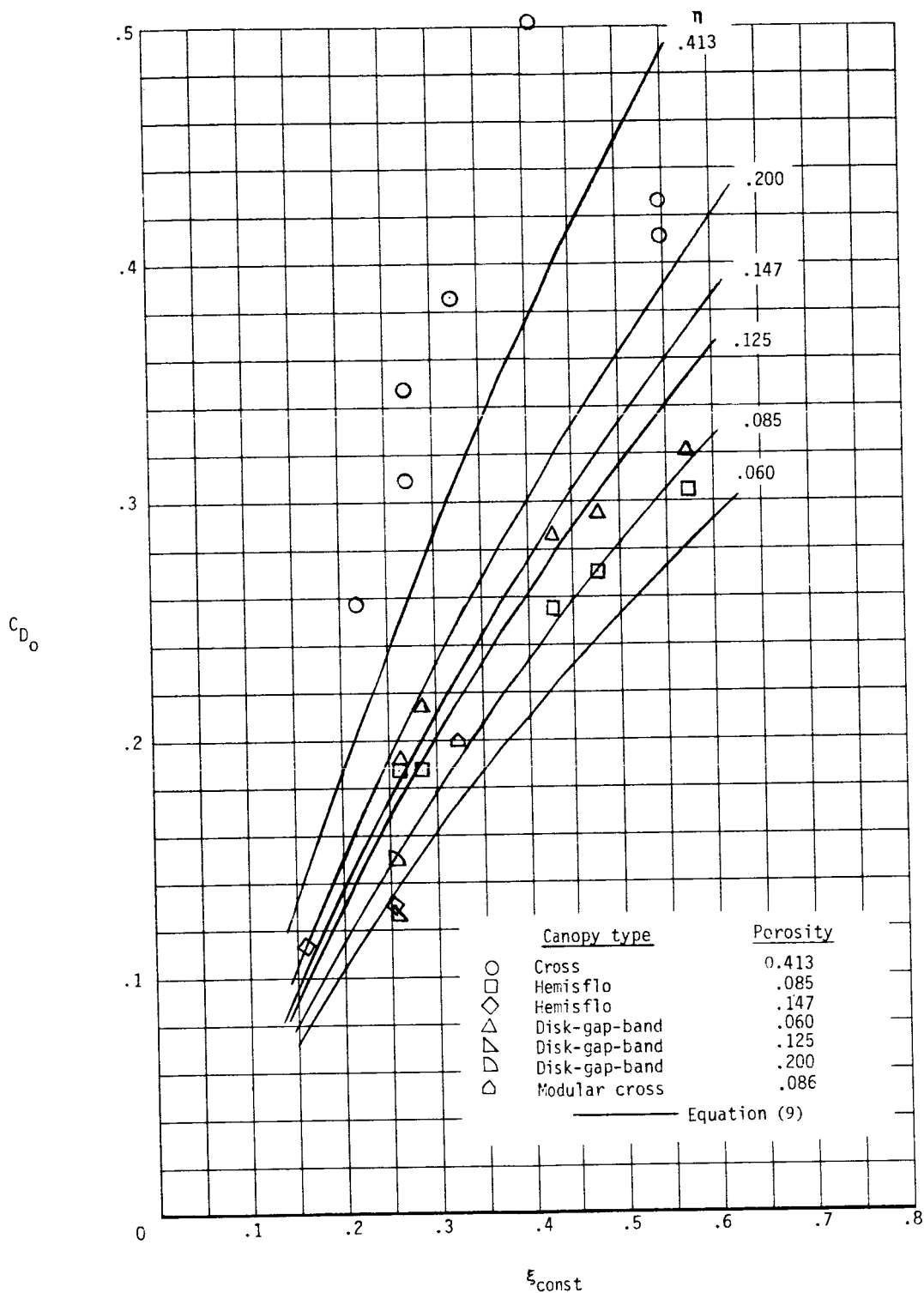
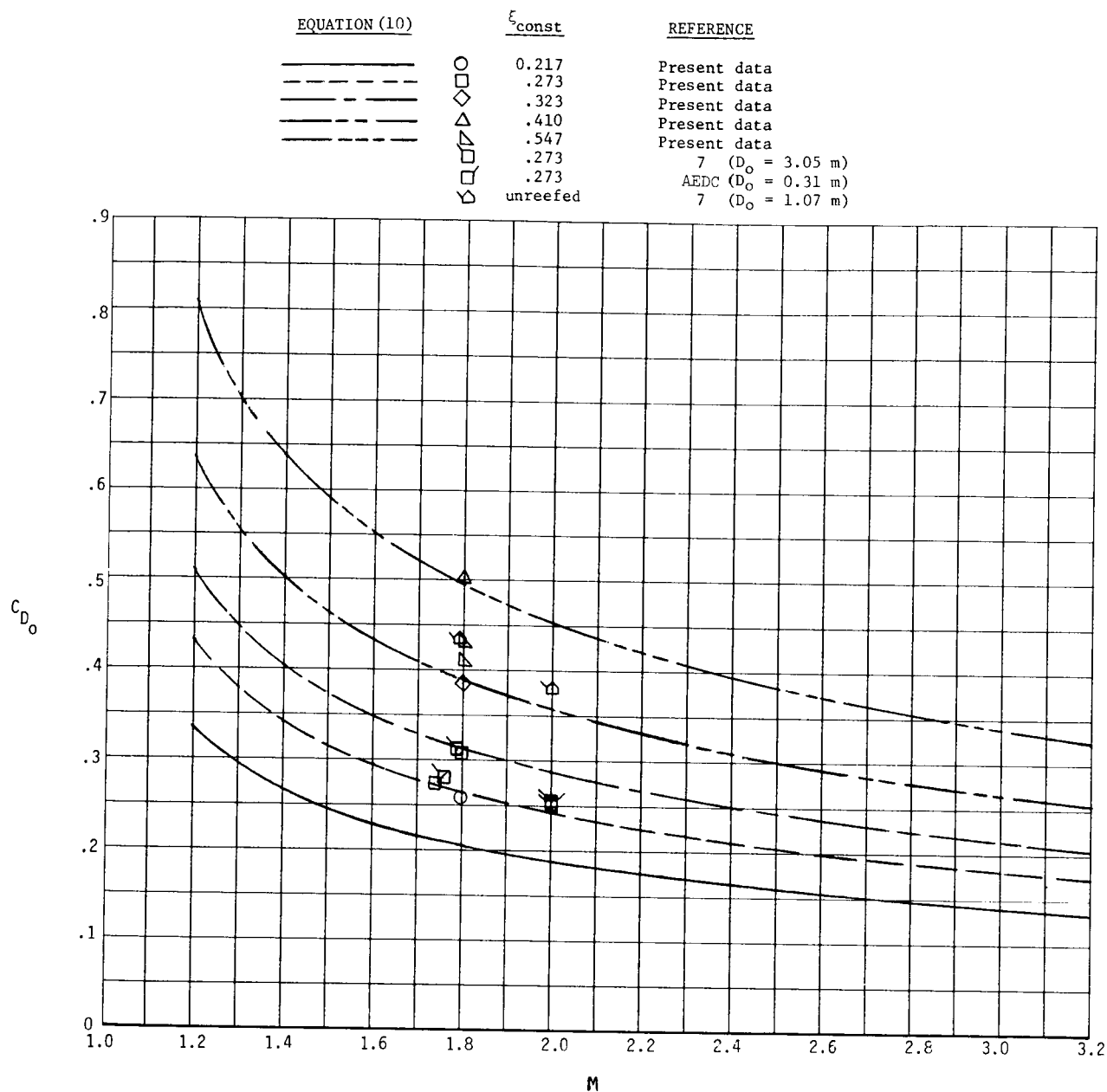


Figure 20.- Comparison of measured data with correlation equation for the variation of drag coefficient with constructed reefing ratio at  $M = 1.80$ .

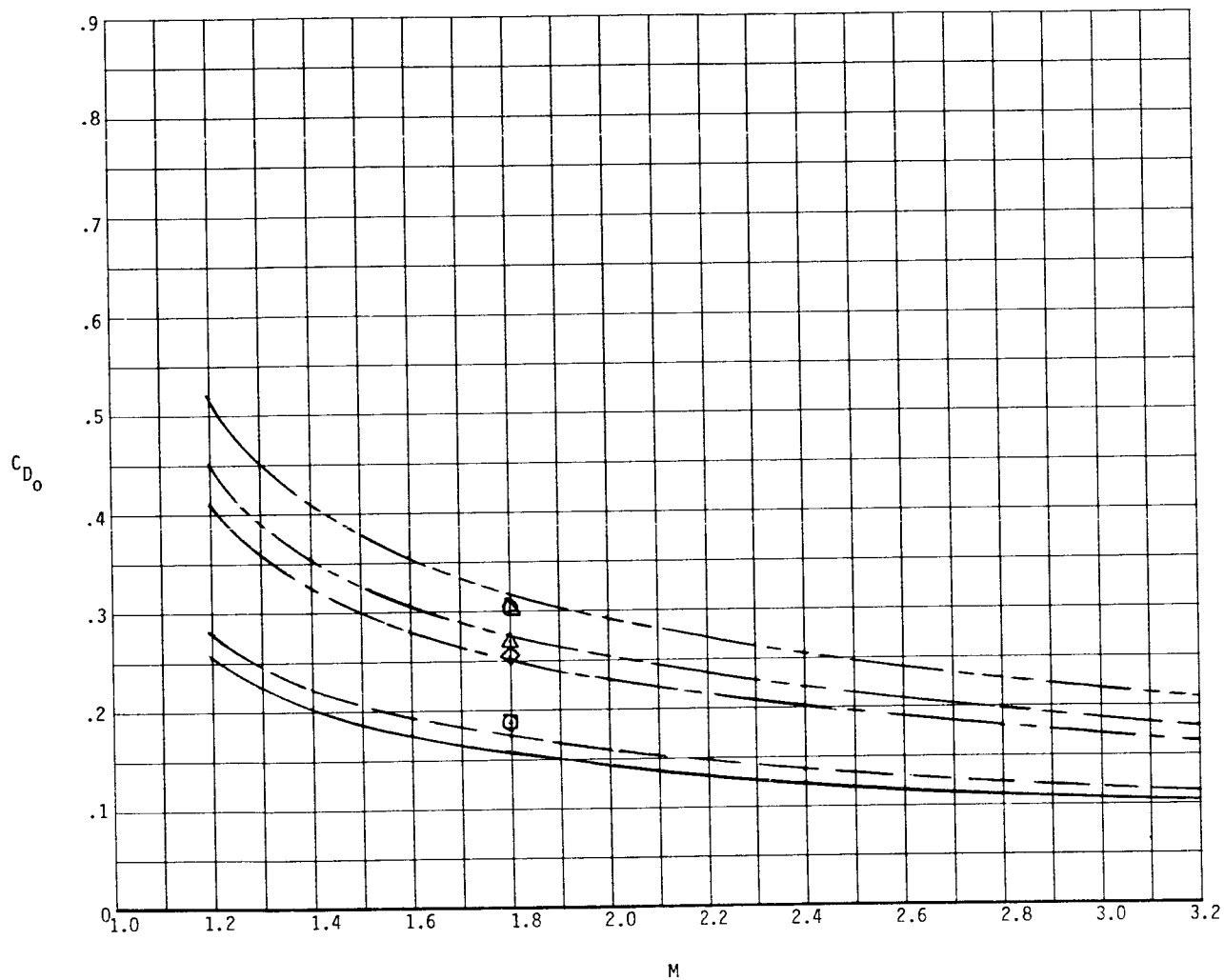


(a) Cross canopies ( $\eta = 0.413$ ).

Figure 21.- Comparison of experimental data and predicted variation of drag coefficient with Mach number in the supersonic range.

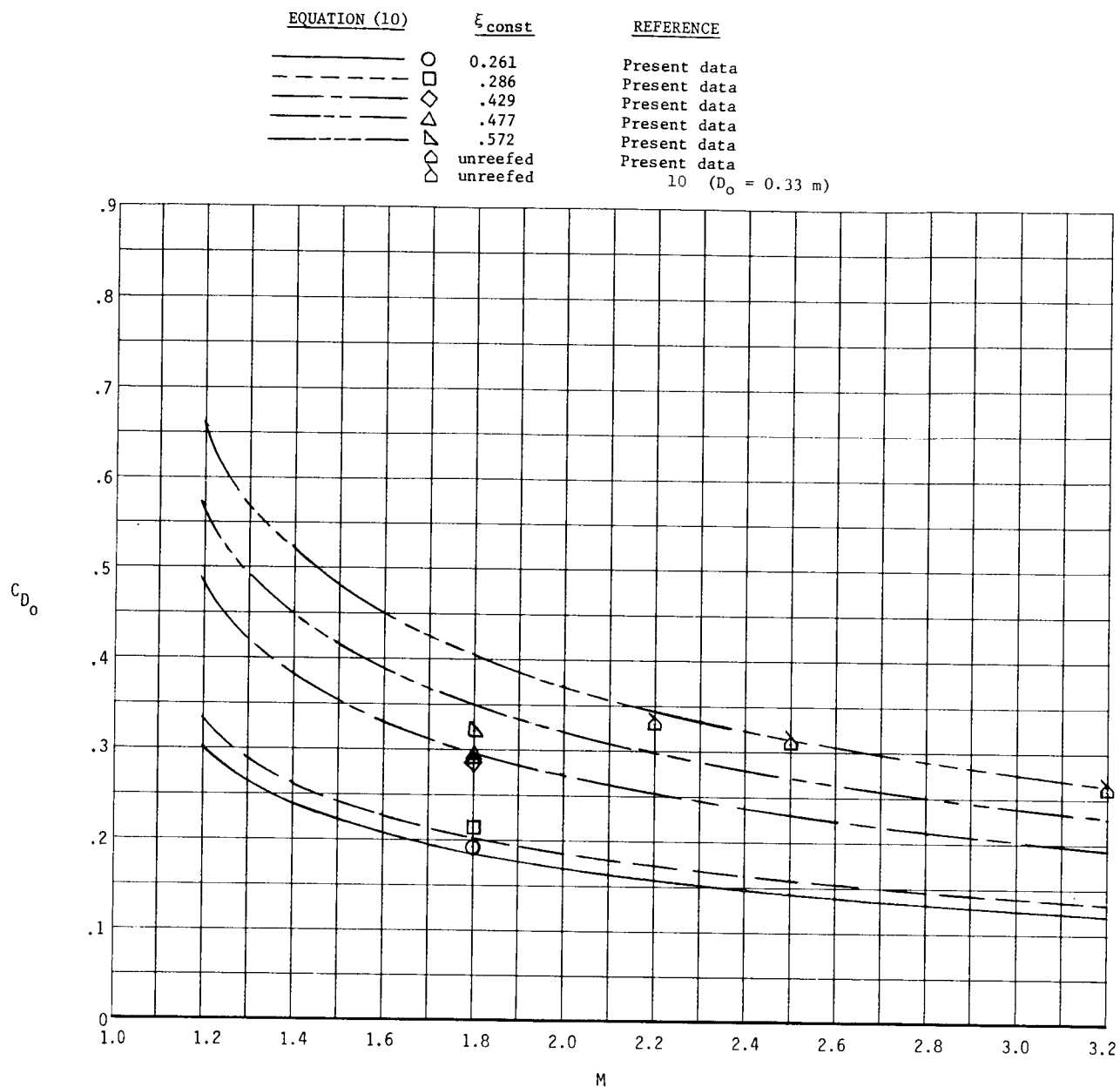


<u>EQUATION (10)</u>		<u><math>\xi_{const}</math></u>	<u>REFERENCE</u>
—————	○	0.261	Present data
-----	□	.286	Present data
-----	◇	.429	Present data
-----	△	.477	Present data
-----	▽	.572	Present data
-----	△	unreefed	Present data



(b) Hemisflo canopies ( $\eta = 0.085$ ).

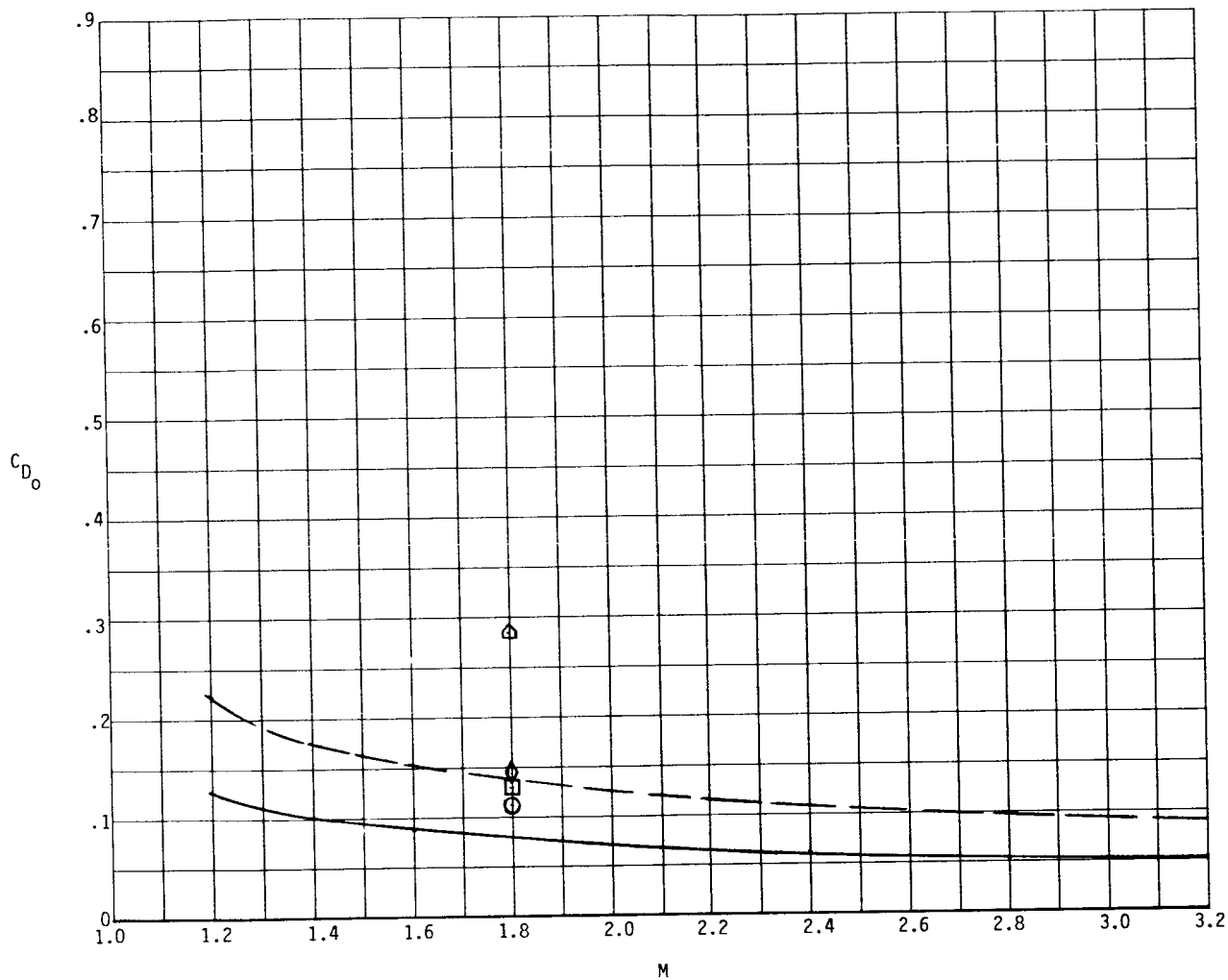
Figure 21.- Continued.



(c) Hemisflo canopies ( $\eta = 0.147$ ).

Figure 21.- Continued.

EQUATION (10)	$\epsilon_{const}$
—————	○ 0.159
-----	□ .254
	◇ .254 (reefed on disk)
	△ unreefed



(d) Disk-gap-band canopies ( $\eta = 0.060$ ).

Figure 21.- Continued.

EQUATION (10)

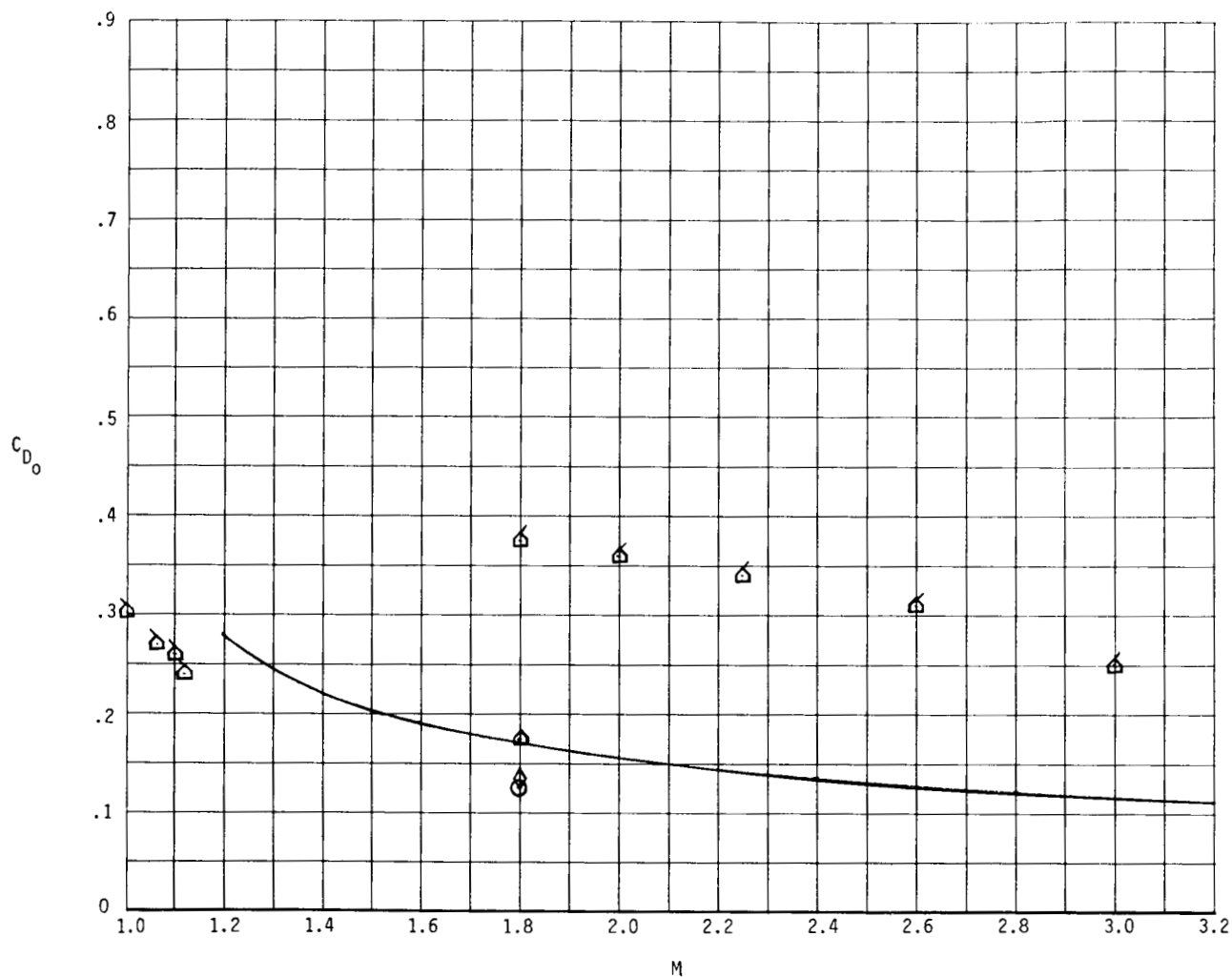
$\xi_{\text{const}}$

REFERENCE

○  
◇  
△  
▽  
□

0.254  
.254  
unreefed  
-  
-

Present data  
Present data (reefed on disk)  
Present data  
12 ( $D_o = 0.25$  m)  
13 ( $D_o = 1.68$  m)



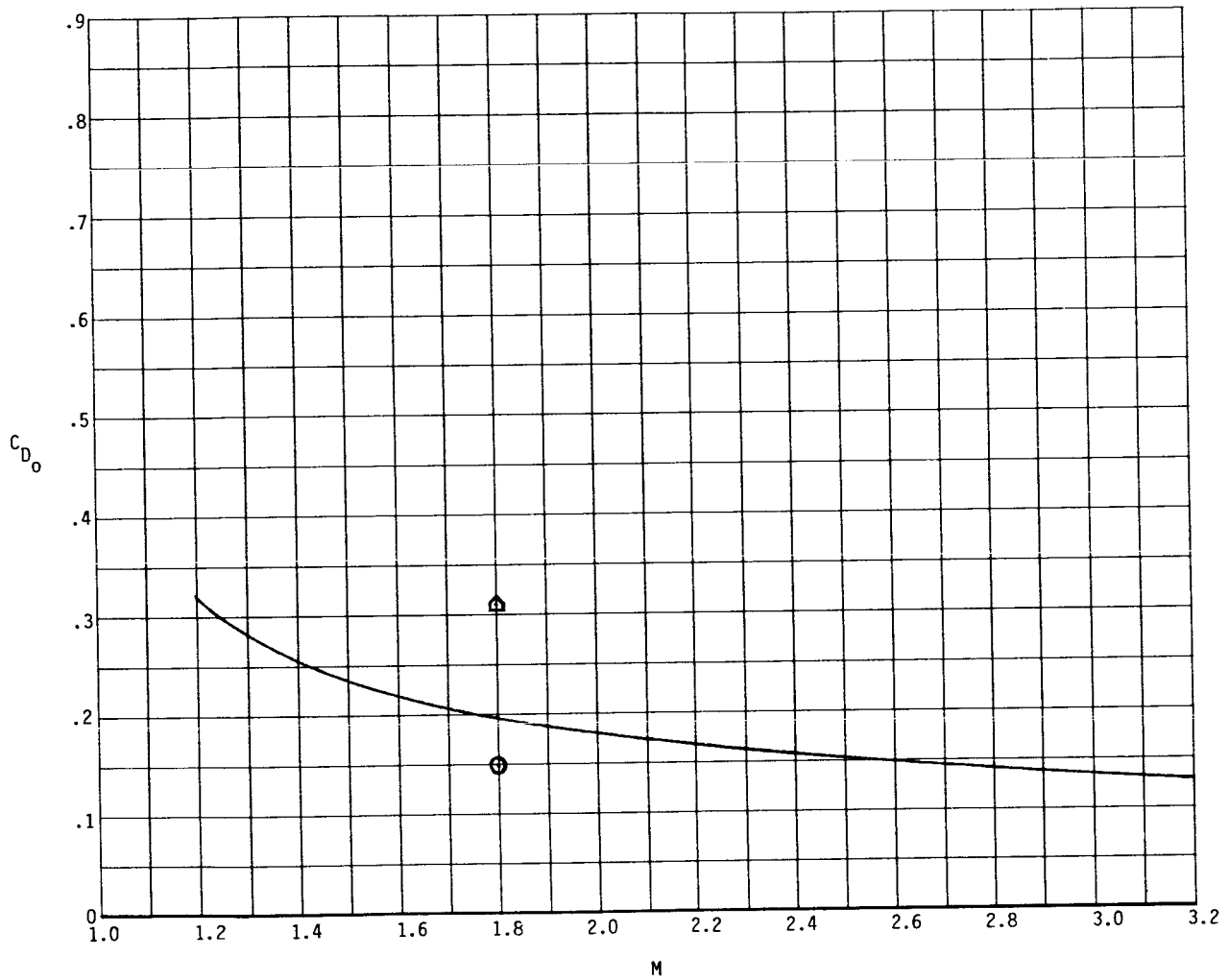
(e) Disk-gap-band canopies ( $\eta = 0.125$ ).

Figure 21.- Continued.

EQUATION (10)

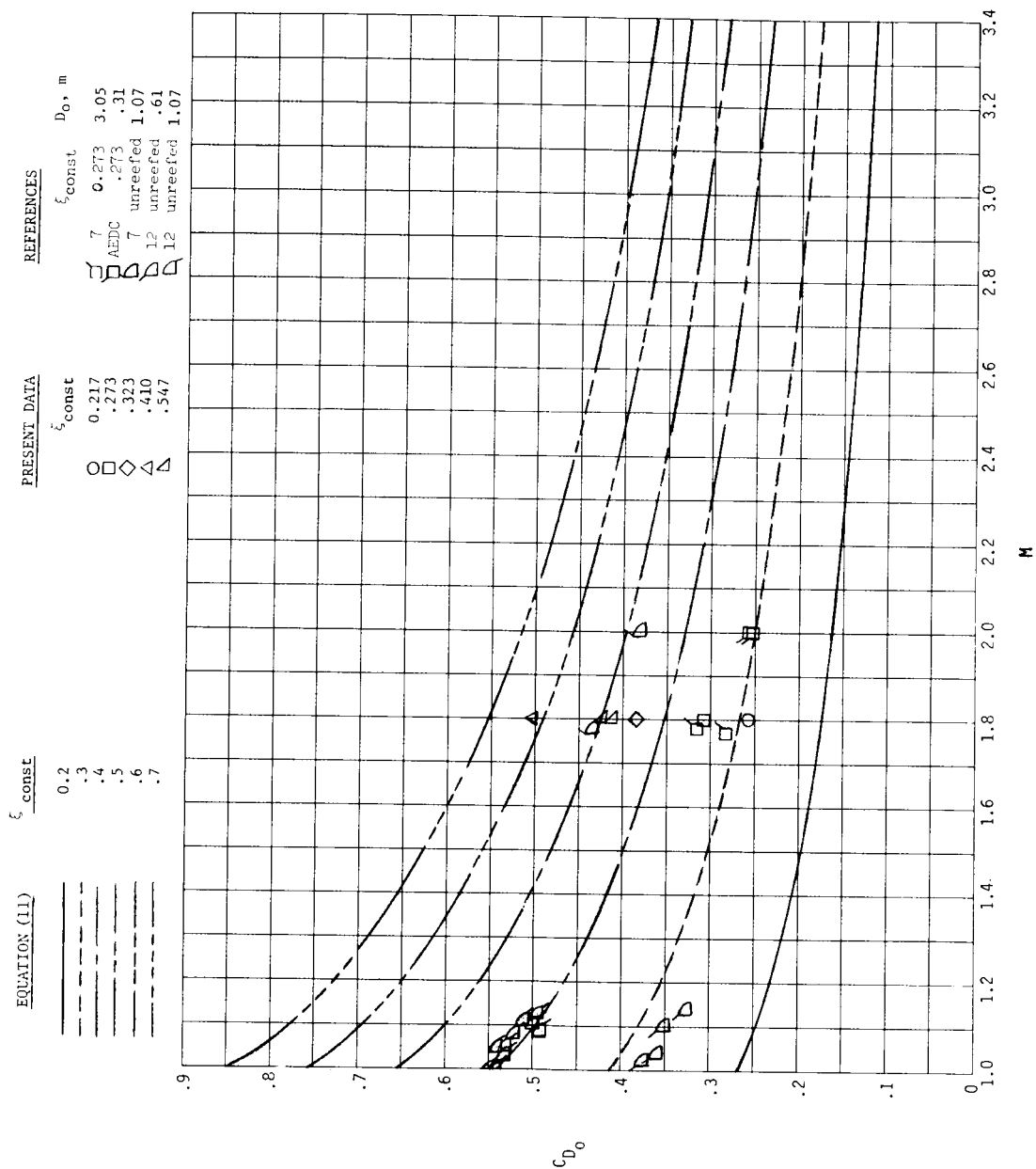
$\xi_{\text{const}}$

○ 0.254  
△ unreefed



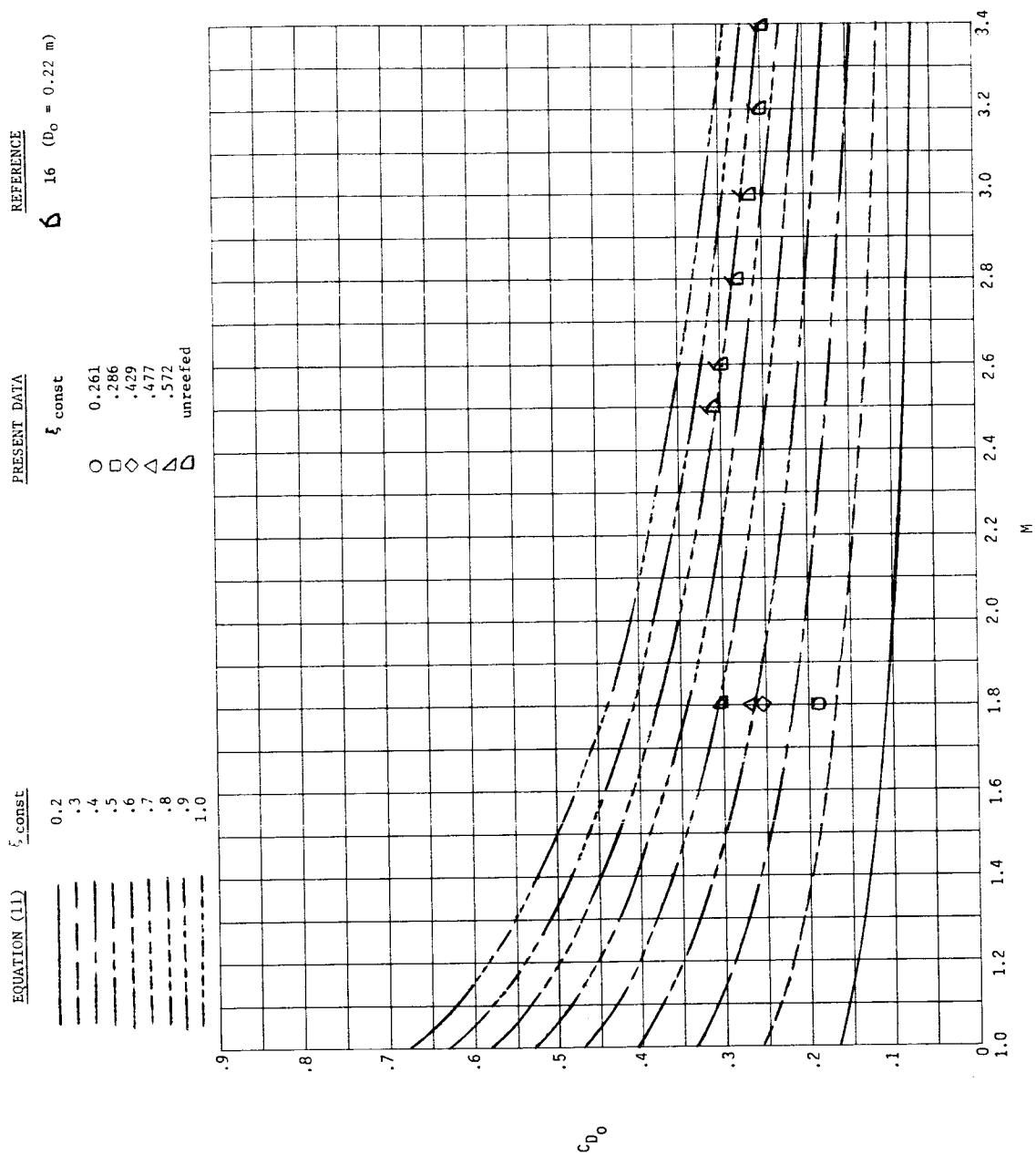
(f) Disk-gap-band canopies ( $\eta = 0.200$ ).

Figure 21.- Concluded.



(a) Cross canopies ( $\eta = 0.413$ ).

Figure 22.- Comparison of experimental data and predicted variation of drag coefficient with Mach number in the high transonic and supersonic range.



(b) Hemisflo canopies ( $\eta = 0.085$ ).

Figure 22. - Continued.

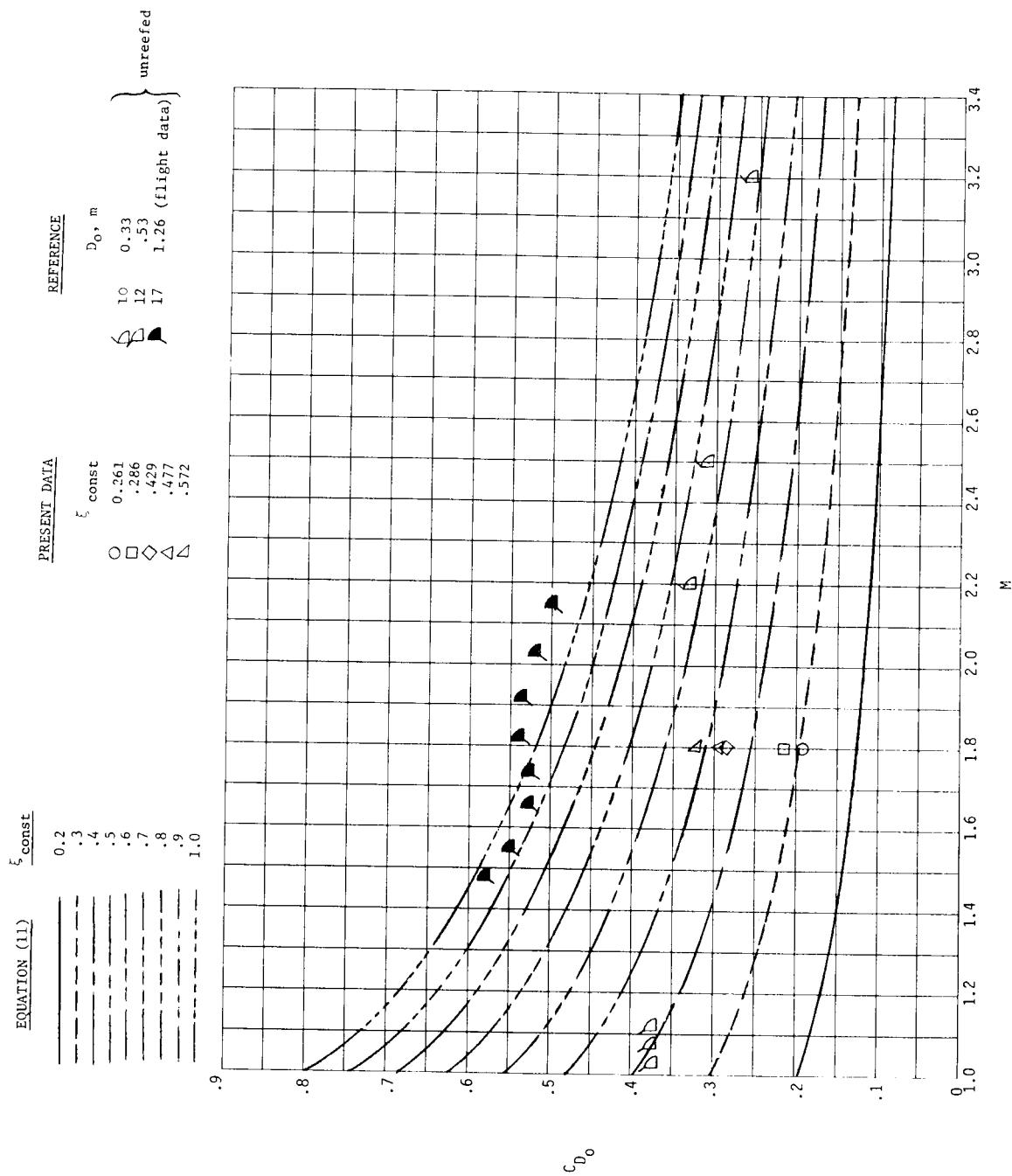
(c) Hemisflo canopies ( $\eta = 0.147$ ).

Figure 22. - Continued.

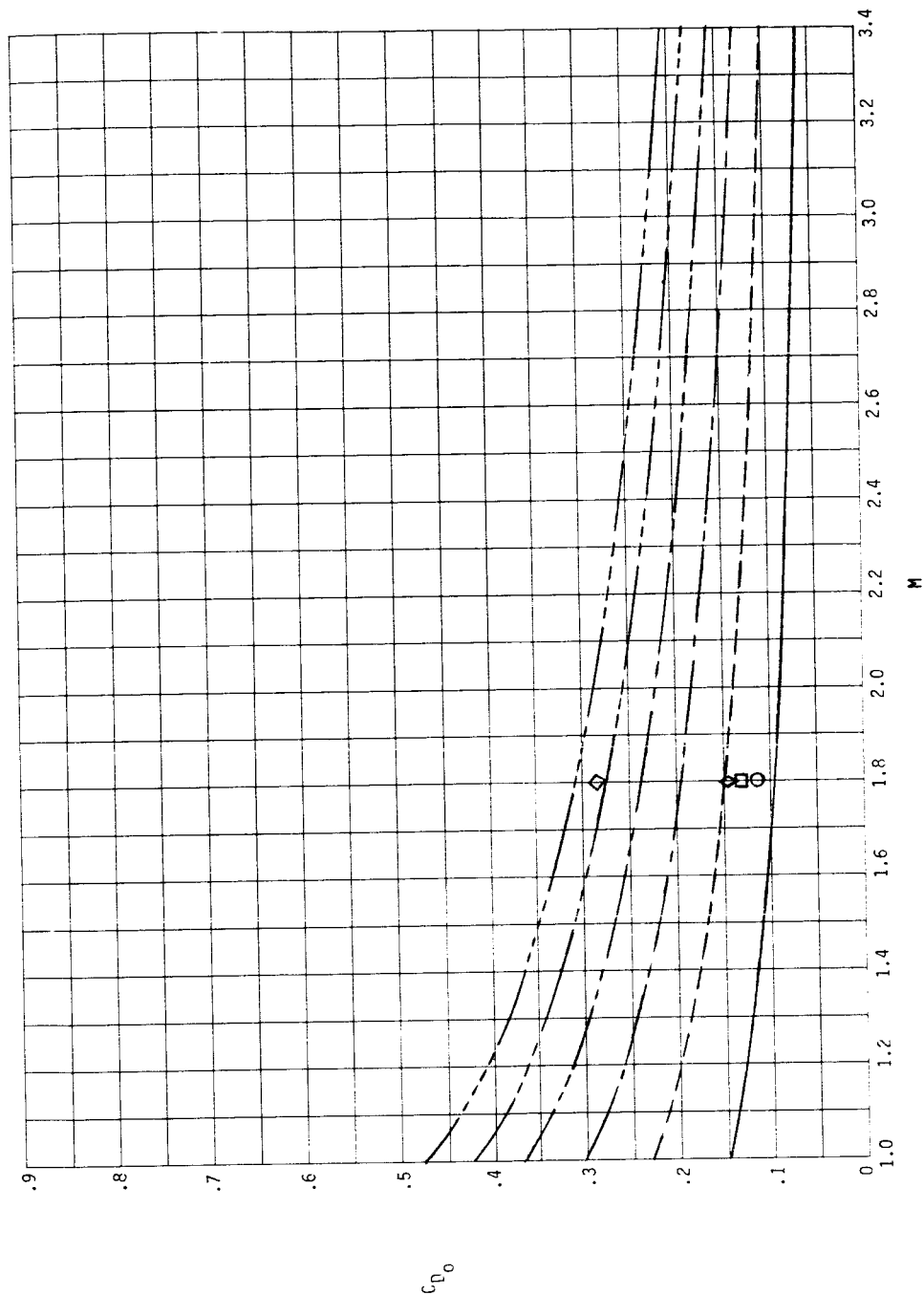


EQUATION (11)

0.2
0.3
0.4
0.5
0.6
0.7

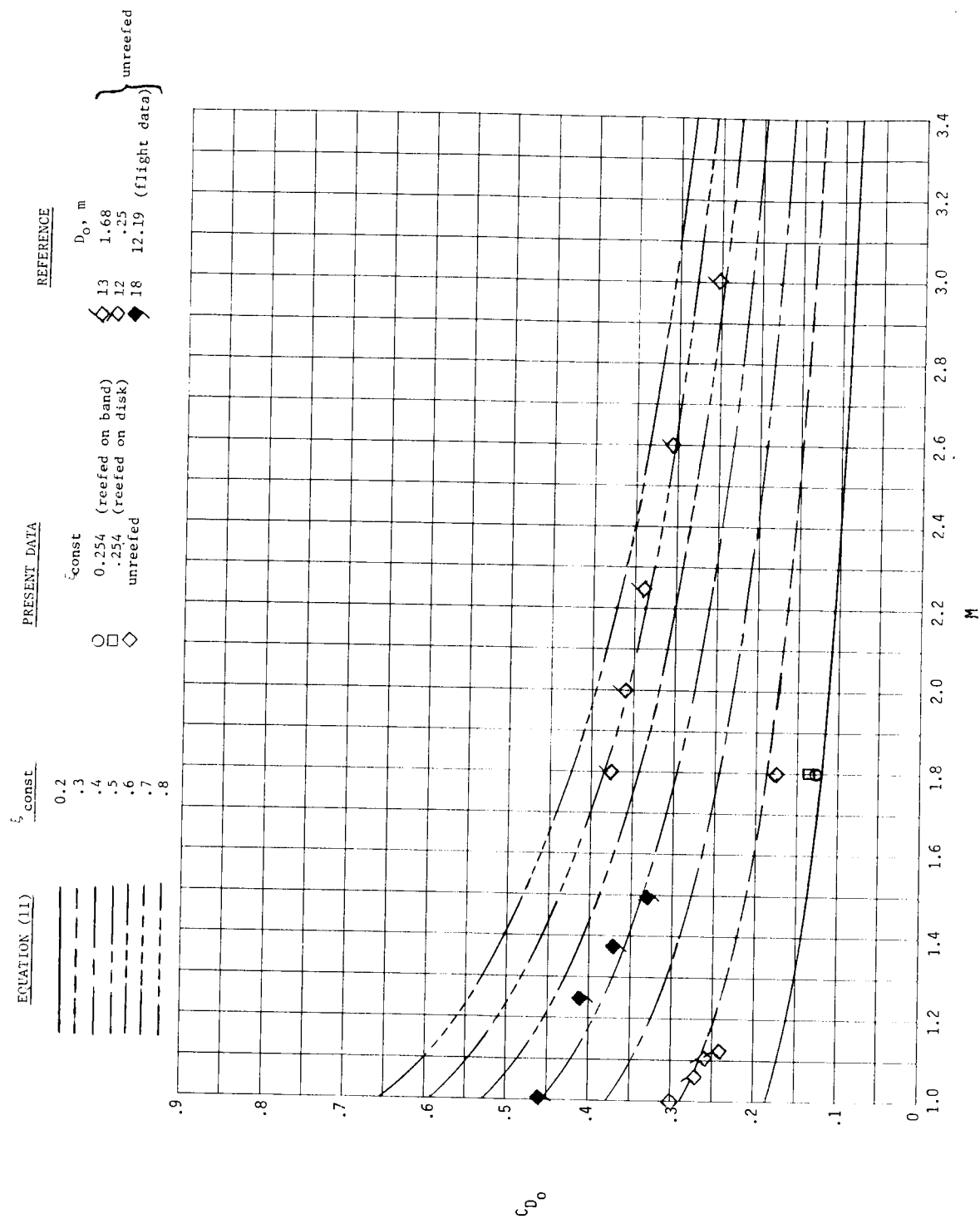
PRESENT DATA

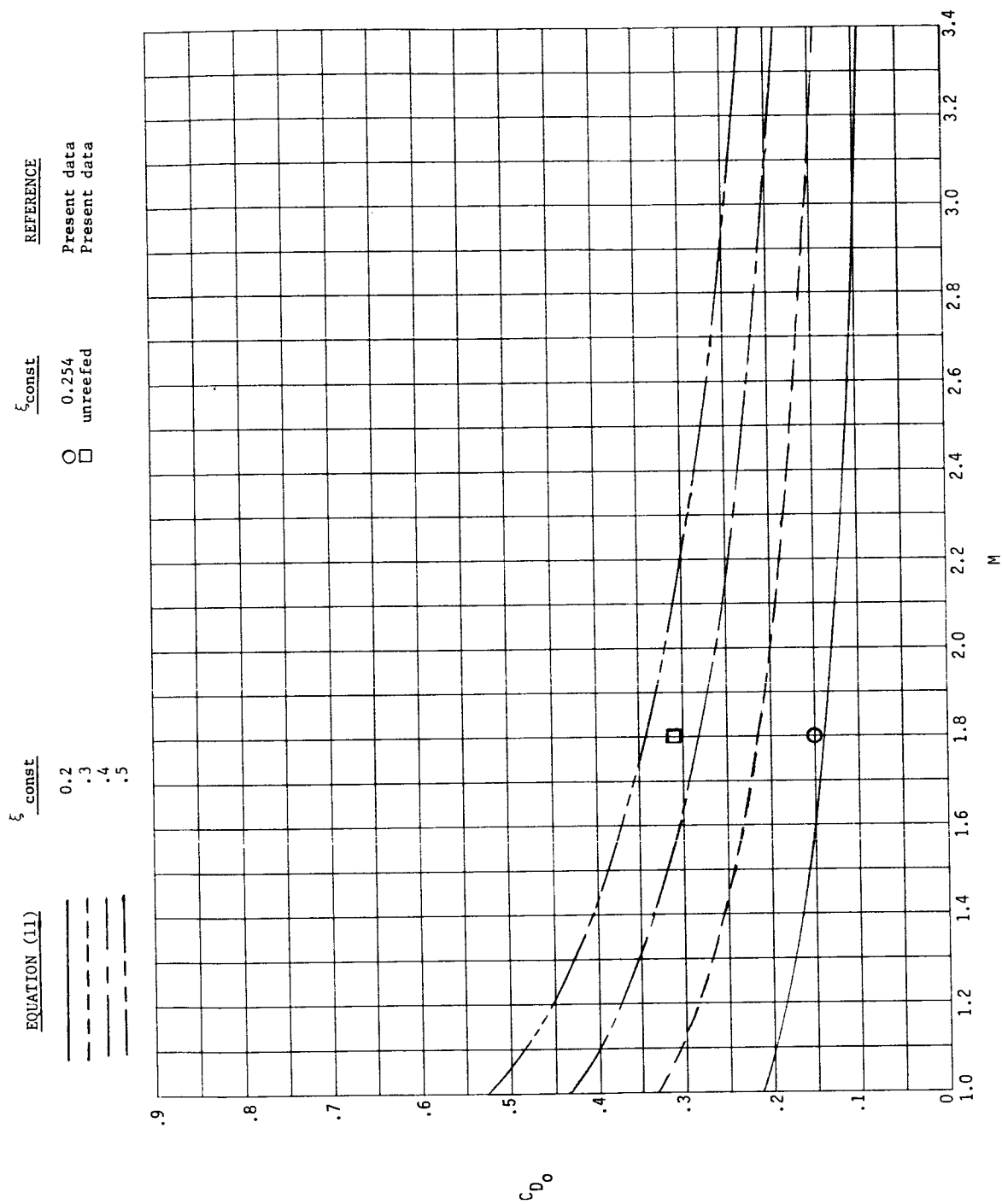
$\zeta$ const
0.159 (reefed on band)
.254 (reefed on disk)
.254 (reefed on disk)
unreefed



(d) Disk-gap-band canopies ( $\eta = 0.06$ ).

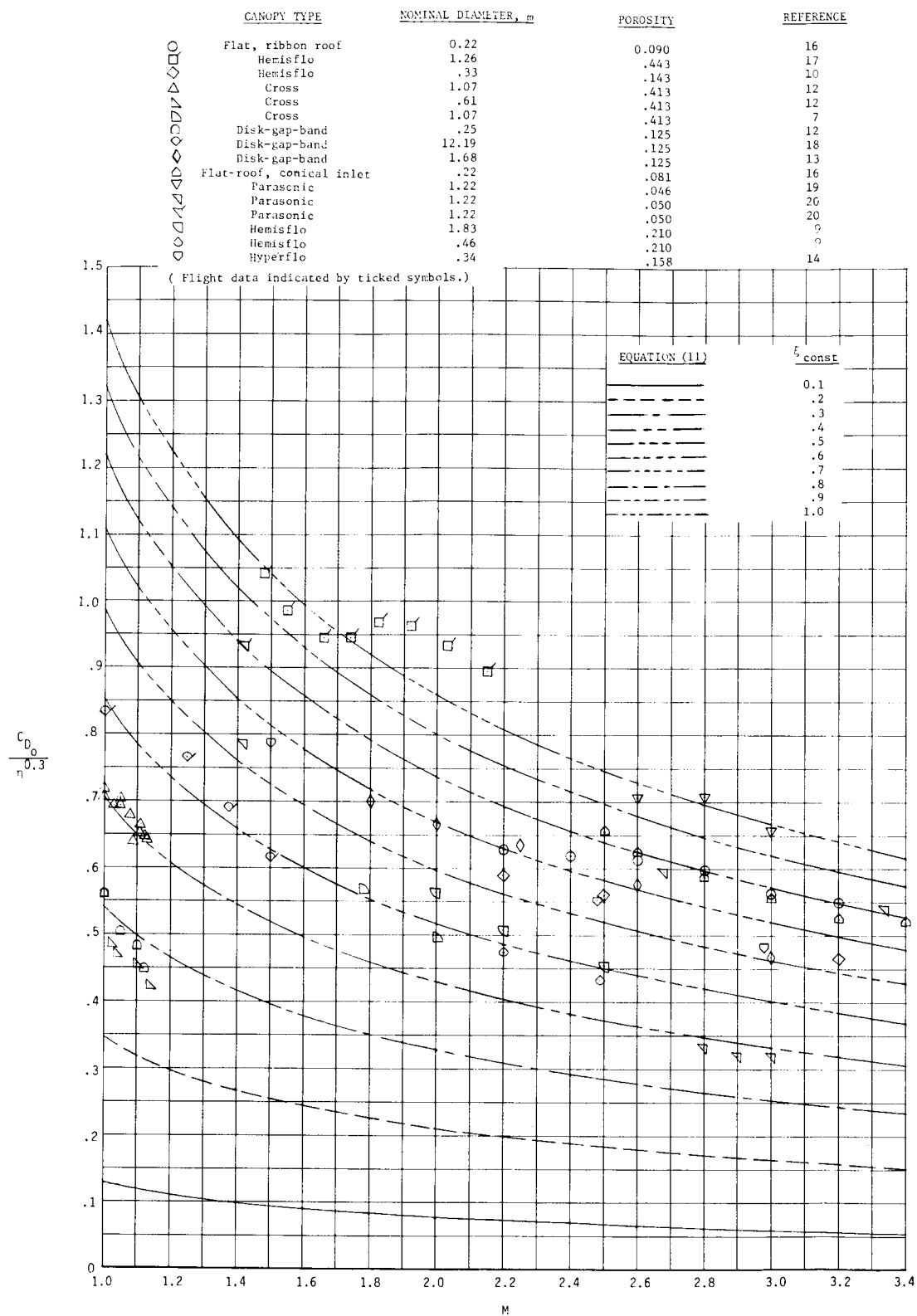
Figure 22. - Continued.





(f) Disk-gap-band canopies ( $\eta = 0.20$ ).

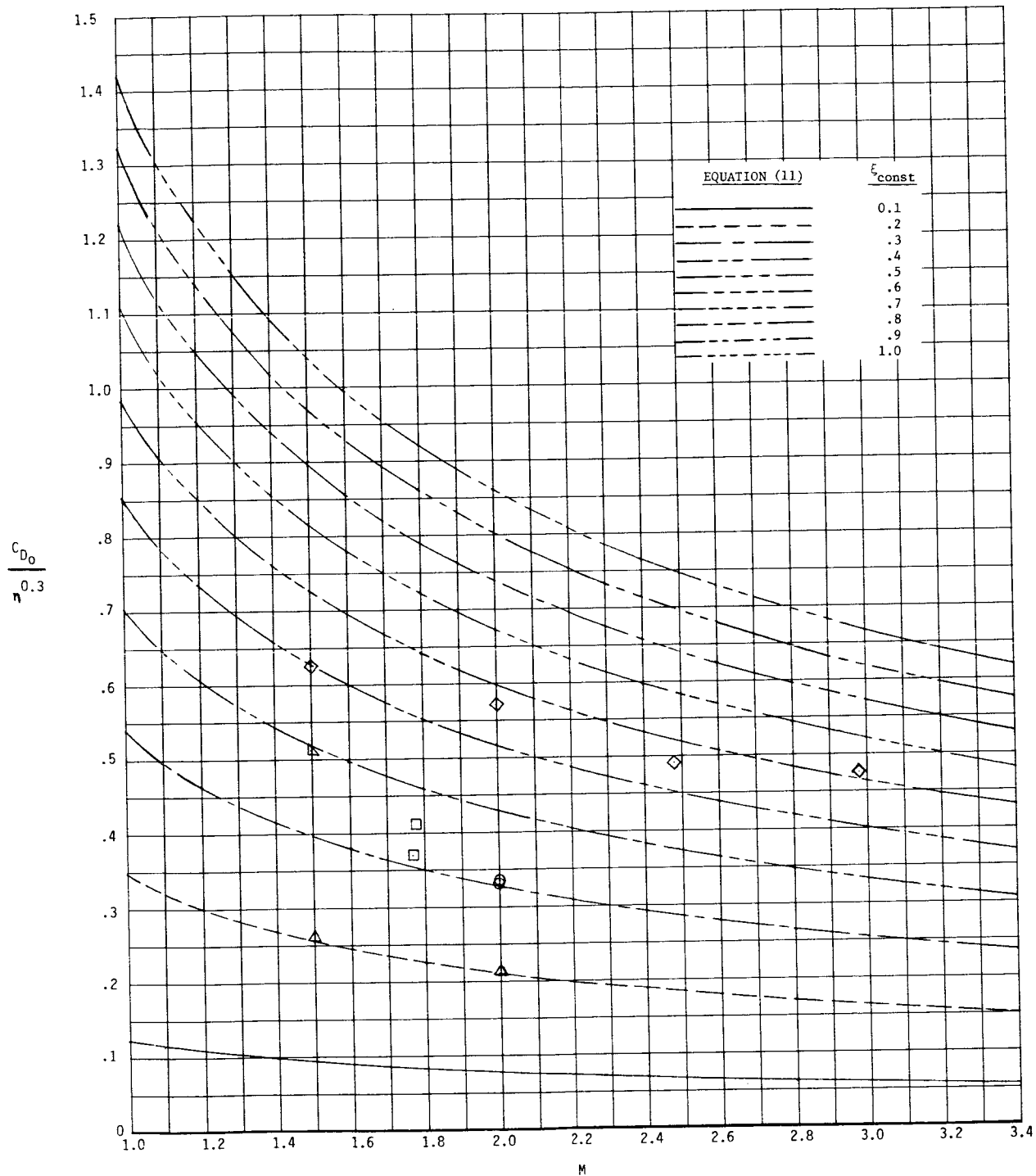
Figure 22. - Concluded.



(a) Unreefed parachutes.

Figure 23.- Comparison of empirically predicted drag coefficients with referenced wind-tunnel and flight data.

	CANOPY TYPE	NOMINAL DIAMETER, m	POROSITY	$\xi_{const}$	REFERENCE
○	Cross	0.31	0.413	0.273	AEDC
□	Cross	3.05	.413	.273	7
◇	Hyperflo	.30	.174	.575	14
△	Hemisflo	.33	.280	.289	14
▽	Hemisflo	.33	.280	.390	14



(b) Reefed parachutes.

Figure 23. - Concluded.



POSTMASTER .

If Undeliverable (Section 158  
Postal Manual) Do Not Return

*"The aeronautical and space activities of the United States shall be conducted so as to contribute . . . to the expansion of human knowledge of phenomena in the atmosphere and space. The Administration shall provide for the widest practicable and appropriate dissemination of information concerning its activities and the results thereof."*

—NATIONAL AERONAUTICS AND SPACE ACT OF 1958

## NASA SCIENTIFIC AND TECHNICAL PUBLICATIONS

**TECHNICAL REPORTS:** Scientific and technical information considered important, complete, and a lasting contribution to existing knowledge.

**TECHNICAL NOTES:** Information less broad in scope but nevertheless of importance as a contribution to existing knowledge.

**TECHNICAL MEMORANDUMS:** Information receiving limited distribution because of preliminary data, security classification, or other reasons. Also includes conference proceedings with either limited or unlimited distribution.

**CONTRACTOR REPORTS:** Scientific and technical information generated under a NASA contract or grant and considered an important contribution to existing knowledge.

**TECHNICAL TRANSLATIONS:** Information published in a foreign language considered to merit NASA distribution in English.

**SPECIAL PUBLICATIONS:** Information derived from or of value to NASA activities. Publications include final reports of major projects, monographs, data compilations, handbooks, sourcebooks, and special bibliographies.

**TECHNOLOGY UTILIZATION PUBLICATIONS:** Information on technology used by NASA that may be of particular interest in commercial and other non-aerospace applications. Publications include Tech Briefs, Technology Utilization Reports and Technology Surveys.

Details on the availability of these publications may be obtained from:

SCIENTIFIC AND TECHNICAL INFORMATION OFFICE

NATIONAL AERONAUTICS AND SPACE ADMINISTRATION

Washington, D.C. 20546